3-21-2019

Scaling Film Cooling Adiabatic Effectiveness with Mass Transfer and Thermal Experimental Techniques

Luke J. McNamara

SCALING FILM COOLING ADIABATIC EFFECTIVENESS WITH MASS TRANSFER AND THERMAL EXPERIMENTAL TECHNIQUES

THESIS

Luke J. McNamara, Captain, USAF

AFIT-ENY-MS-19-M-233

DEPARTMENT OF THE AIR FORCE
AIR UNIVERSITY

AIR FORCE INSTITUTE OF TECHNOLOGY

WRIGHT-PATTERSON AIR FORCE BASE, OHIO

AFIT-ENY-MS-19-M-233

SCALING FILM COOLING ADIABATIC EFFECTIVENESS WITH MASS TRANSFER AND THERMAL EXPERIMENTAL TECHNIQUES

THESIS

Presented to the Faculty

Department of Aeronautics and Astronautics

Graduate School of Engineering and Management

Air Force Institute of Technology

Air University

Air Education and Training Command

In Partial Fulfillment of the Requirements for the

Degree of Master of Science in Aeronautical Engineering

Luke J. McNamara, BS

Captain, USAF

March 2019

AFIT-ENY-MS-19-M-233

SCALING FILM COOLING ADIABATIC EFFECTIVENESS WITH MASS TRANSFER AND THERMAL EXPERIMENTAL TECHNIQUES

THESIS

Luke J. McNamara, BS
Captain, USAF

Committee Membership:

Lt Col James L. Rutledge, PhD, PE
Chair

Dr. Marc D. Polanka
Member

Dr. Andrew T. Lethander
Member

Abstract

With the continued desire for more power and thrust from gas turbine engines, combustion exhaust gas temperatures are escalating. Thus, it is becoming increasingly important to design effective film cooled engine components to avoid failure. Due to high cost and complexity experimenting at engine conditions, low temperature tests on geometrically scaled up models are often performed. The nondimensional adiabatic effectiveness, η, can be used as an indication of the performance of a film cooling scheme provided the coolant flow rate is properly scaled. Matching the appropriate coolant flow rate parameter at low temperature film cooling test conditions to accurately scale results to engine conditions is a topic of continued debate. Although tests are most commonly conducted using thermal measurement techniques, such as infrared (IR) thermography, the use of pressure sensitive paints (PSPs) with the heat-mass transfer analogy can be used to implement a boundary condition analogous to an adiabatic wall without having to correct for conduction, as is required with thermal techniques.

The increased use of PSPs for film cooling effectiveness experiments raises the question of how mass transfer experimental techniques compare to thermal experimental techniques. In the present work, a thermal technique using infrared thermography was compared to a mass transfer technique using a pressure sensitive paint. The two methods were evaluated on the same model, a flat plate with a single zero-degree compound angle 7-7-7 shaped hole. The coolant gases evaluated in this study were argon, carbon dioxide, helium, and nitrogen to offer comprehensive gas property variation to evaluate the efficacy of several coolant flow rate parameters' scaling ability. From results of a previous study, it

was confirmed that when the specific heat is accounted for, adiabatic effectiveness results are best scaled using the Advective Capacity Ratio (*ACR*) with an IR thermal measurement technique at low momentum flux ratios. A method for collecting and reducing results from large experimental datasets with PSPs was improved upon in this study. The new method utilized an interpolation of reference images taken at the beginning and the end of the dataset to account for paint degradation from extended exposure to the excitation light source used to capture partial pressures on the surface of the test model. Using the new testing method, results indicate that the mass flux ratio (*M*) is the appropriate parameter to accurately scale adiabatic effectiveness results between gases with a large range of gas property variation using the mass transfer technique. This has significant implication for engine designers that rely on experimental data to predict engine behavior.

Acknowledgments

I would like to thank my research advisor, Lt Col James Rutledge, for his unwavering passion and guidance. All the lessons and support were greatly appreciated. I would also like to thank Dr. Marc Polanka for his direction and advice, especially on the second and third chapters, and for helping me become a better technical writer and presenter. Further, I would like to acknowledge Dr. Andy Lethander and the other members of AFRL/RQTT, without their support, this research could not take place. I also wish to thank Lt Jake Fischer and Capt Connor Wiese for always being there for me when I had a question or needed advice.

Luke J. McNamara

Table of Contents

Page

List of Figures

Page

List of Tables

Page

Nomenclature

ACR	=	advective capacity ratio, $\frac{\rho_c c_{P,c} u_c}{\rho_\infty c_{P,\infty} u_\infty}$
BDR	=	binary diffusion coefficient ratio, $\frac{\mathcal{D}_c}{\mathcal{D}_\infty}$
C	=	mass concentration
c_P	=	specific heat at constant pressure, (J/kg-K)
CpR	=	specific heat ratio, $\frac{c_{P,c}}{c_{P,\infty}}$
D	=	cooling hole diameter, (m)
$\mathcal{D}$	=	binary diffusion coefficient, (m^2/s)
DR	=	coolant-to-freestream density ratio, $\frac{\rho_c}{\rho_\infty}$
G	=	net mass flux vector, (ρu)
h	=	transfer coefficient, heat (W/m^2-K), or mass (m/s)
I	=	momentum flux ratio, $\frac{\rho_c u_c^2}{\rho_\infty u_\infty^2}$
k	=	thermal conductivity, (W/m-K)
kR	=	thermal conductivity ratio, $\frac{k_c}{k_\infty}$
Le	=	Lewis number, $\frac{\propto}{\mathcal{D}}$ or $\frac{Pr}{Sc}$
LeR	=	Lewis number ratio, $\frac{Le_c}{Le_\infty}$
M	=	mass flux (blowing) ratio, $\frac{\rho_c u_c}{\rho_\infty u_\infty}$
$\mathcal{M}$	=	molecular weight, (kg/kmol)
Nu	=	Nusselt number, $\frac{h_f l}{k}$
p	=	partial pressure, (Pa)
P	=	pressure, (Pa)

Pr	=	Prandtl number, $\frac{\mu c_P}{k}$ or $\frac{\nu}{\alpha}$
q''	=	heat flux, (W/m^2)
Re	=	Reynolds number, $\frac{\rho u l}{\mu}$ or $\frac{u l}{\nu}$
ReR	=	coolant-to-freestream Reynolds number ratio, $\frac{\rho_c u_c \mu_\infty}{\rho_\infty u_\infty \mu_c}$
Sc	=	Schmidt number, $\frac{\mu}{\rho \mathcal{D}}$ or $\frac{\nu}{\mathcal{D}}$
Sh	=	Sherwood number, $\frac{h_M l}{\mathcal{D}}$
t	=	thickness, (m)
T	=	temperature, (K)
T_{t_4}	=	turbine inlet temperature
Tu	=	freestream turbulence intensity
u	=	velocity, (m/s)
VR	=	velocity ratio, $\frac{u_c}{u_\infty}$
x	=	first ordinate, (m)
$\mathcal{X}$	=	mole fraction
y	=	second ordinate, (m)
z	=	third ordinate, (m)
α	=	thermal diffusivity, $\frac{k}{\rho c_P}$, (m^2/s)
ΔT	=	temperature difference, (K)
δ	=	boundary layer thickness
ε	=	measurement uncertainty
ϵ	=	turbulent diffusivity

η	=	adiabatic effectiveness, $\frac{T_\infty - T_{aw}}{T_\infty - T_c}$
$\bar{\eta}$	=	spanwise-averaged adiabatic effectiveness
$\bar{\bar{\eta}}$	=	area-averaged adiabatic effectiveness
μ	=	dynamic (absolute) viscosity, (Pa-s)
μR	=	dynamic (absolute) viscosity ratio, $\frac{\mu_c}{\mu_\infty}$
ν	=	kinematic viscosity, $\frac{\mu}{\rho}$, (m^2-s)
ρ	=	density, (kg/m^3)
ζ	=	arbitrary measured quantity

Subscripts

AB	=	property of chemical species A and B combined
amb	=	ambient condition
app	=	apparent
aw	=	adiabatic wall
c	=	coolant
D	=	with respect to hole diameter
$\mathcal{D}$	=	for determination of binary diffusion coefficients
e	=	coolant hole exit plane
f	=	with film cooling
fg	=	with foreign gas injection, or property of the foreign gas
M	=	relating to mass transfer

max	=	maximum
min	=	minimum
O_2	=	of oxygen
ref	=	reference condition
s	=	at the surface
T	=	relating to thermal
$turb$	=	relating to turbulence
w	=	property of model test surface
x	=	of the first ordinate
y	=	of the second ordinate
z	=	of the third ordinate
η	=	of adiabatic effectiveness
ρ	=	of the density
0	=	no surface cooling
∞	=	of or relating to the freestream

Acronyms

BNC	=	Bayonet Neill-Concelman
CAD	=	computer-aided design
CCD	=	charged coupled device
CFD	=	computational fluid dynamics

DP	=	data point
GUI	=	graphical user interface
IR	=	infrared thermography
ISSI	=	Innovative Scientific Solutions, Inc.
LAN	=	local area network
LED	=	light emitting diode
NI	=	National Instruments
PSG	=	pulse generator
PSP	=	pressure sensitive paint
RSS	=	root-sum-squared
SLPM	=	standard liters per minute
TSP	=	temperature sensitive paint
TTL	=	transistor-transistor logic
UV	=	ultraviolet

SCALING FILM COOLING ADIABATIC EFFECTIVENESS WITH MASS TRANSFER AND THERMAL EXPERIMENTAL TECHNIQUES

1. Introduction

Gas turbine engines have played an essential role since their introduction in the 1940s for the United States Air Force as well as commercial airlines. Not only do gas turbine engines act as the propulsion systems for aircrafts such as fighters, bombers, cargo aircraft, and passenger aircraft, they also act as power generation systems on the ground. In terms of design, the parameters most considered are cost, weight, efficiency, and performance. As the desire for more power out of gas turbine engines persists, engine designers continue to push the limits of design capabilities. One way to increase the power output from gas turbine engines is to increase the temperature of the gases exiting the combustor and entering the turbine.

In many applications, the rise of combustor gas temperatures has exceeded the material limits of the turbine components the gases are impinging upon. As the turbine components are exposed to constant mechanical stresses while operating at the exceedingly high temperatures, they become subject to slow plastic deformation, called creep. Creep is one of the most imperative failure mechanisms to turbine airfoils. In a study of turbine blade temperature as it relates to life expectancy, Rezazadeh et al. [1] found that a 10 K increase to turbine airfoils at engine operating temperatures caused the airfoils' creep life to decrease by 40%. Thus, to prevent turbine airfoil failure, it is important to design effectively cooled turbine components.

There are two primary ways to cool a turbine airfoil, internal cooling and external cooling. Both mechanisms reroute relatively cool air, called bleed air, from the compressor, around the combustor and out to the turbine components. Internal cooling takes the bleed air and routes it along the internal surfaces of the turbine airfoils. External cooling, known as film cooling, injects

the bleed air through small holes manufactured through the surface to distribute the air over the airfoils. One problem with turbine airfoil cooling mechanisms is that they remove air that the compressor was doing work on. By doing this, there is less air that enters the combustor, which, in turn, lowers the amount of the oxidizer in the combustor causing a lower energy reaction and a loss of efficiency to the cycle. One objective of engine cooling designers is to reduce the amount of cooling air taken from the compressor while also reducing the amount of heat transfer occurring from the high temperature gases to the turbine components. Decreasing the amount of air removed from the compressor allows engines to use more of the incoming air, increasing the performance of the gas turbine engines.

To evaluate film cooling designs, many studies revolved around the performance of the cooling schemes. Popular performance considerations consist of hole geometry and configuration. Another performance consideration is the flow rate of the coolant injected onto the surface through the film cooling holes. To analyze these performance considerations, low temperature tests are often performed due to the high cost and difficulty experimenting at engine conditions. Geometrically scaled up models are commonly used in low temperature tests as a surrogate to small engine components to achieve greater fidelity in experimentation. Geometrically scaled up models also allow tests to be conducted at much lower velocities while still matching the freestream Reynolds number. To make results from experiments at ambient conditions relevant to engine conditions, the results must be appropriately scaled between the two conditions.

Film cooling scaling research has proven difficult since many gas properties change with temperature and each gas property changes by a different factor. Thus, there is no way to simultaneously match every gas property of the coolant and the freestream from ambient conditions to engine conditions. This led researchers to investigate a variety of coolant flow rate

parameters to analyze how to best scale results between conditions. Previous research has revolved around the density ratio between the coolant and the freestream, a value of approximately two at engine conditions. However, the success of matching coolant flow rate parameters that deal only with density and coolant flow rate have found limitations. This is because of other gas properties often overlooked, such as specific heat. One method of analyzing coolant flow rate parameters while evaluating the effects of different gas properties is to use a diverse group of foreign gases for the coolant. An appropriate coolant flow rate parameter to use in experimentation would be able to scale cooling effectiveness results between the different foreign gases, no matter the variation in their gas properties.

Numerous experimental techniques have been used to evaluate film cooling effectiveness. Many of these techniques can be split into two main categories, thermal measurement techniques and techniques that utilize the heat-mass transfer analogy. One of the most common thermal measurement techniques is infrared (IR) thermography. However, when evaluating film cooling adiabatic effectiveness, one shortcoming of IR thermography is that the results are influenced by conductive heat transfer. Due to this, heat-mass transfer methods have seen an increased use with pressure sensitive paints (PSPs) to apply a boundary condition analogous to that of an adiabatic wall when determining adiabatic effectiveness distributions. Mass transfer methods do have shortcoming of their own, for example, some thermal relations between the coolant and the freestream gases are dropped. Therefore, success of the evaluations from both IR thermography and PSP measurement techniques have produced mixed results [2] [3].

A previous study sought to determine the best coolant flow rate parameter to scale film cooling adiabatic effectiveness with a thermal measurement technique on a flat plate with an expanded exit, zero-degree compound angle cooling hole [2]. The study used a variety of foreign

gases to explore a large variation of gas properties. The results showed that when scaling adiabatic effectiveness, it is imperative to account for the specific heats of the gases. The question then arises whether a mass transfer method, with an insensitivity to thermal effects, can be used as a surrogate to thermal measurement techniques.

The objectives of this study are summarized by the following:

- Determine the best coolant flow rate parameter to scale adiabatic effectiveness with a pressure sensitive paint mass transfer experimental technique on a flat plate with a standard laid-back fan shaped zero-degree compound angle cooling hole using a variety of gases to achieve large variations in gas properties.
- Compare the pressure sensitive paint measurement technique to the infrared thermography technique on the exact same flat plate model to determine the differences between experimental results of a mass transfer method and a thermal method.

2. Literature Review

In gas turbine engines, combustor exhaust gases are rising to temperatures above that of the material limit of the turbine airfoils, blades and vanes alike. To withstand these temperatures and avoid failure, the temperature of turbine airfoils can be reduced by two primary means, internal cooling where relatively cool bypass air from the compressor is driven through passages inside the airfoils, and external cooling where compressor bypass air is injected onto the surface of the airfoils. This study will focus on the latter, turbine airfoil film cooling.

The most common parameter for rating film cooling performance is adiabatic effectiveness, η, defined in Section 2.1. Adiabatic effectiveness is a parameter of nondimensional temperature that relates the reduction in T_{aw} from T_∞ along a surface downstream of the coolant injection location, where T_∞ is the freestream temperature and T_{aw} is the temperature of the wall if the wall was adiabatic. Adiabatic effectiveness is used to rate the cooling potential of a given cooling scheme and it is also used as a parameter for comparisons to be made. Characterizing η allows film cooling to be decoupled from internal cooling. A significant amount of film cooling research has gone into determining the best nondimensional coolant flow rate parameter to scale adiabatic effectiveness from test conditions at ambient temperatures and pressures to engine conditions consisting of much higher temperatures and pressures [2] [3].

The current study seeks to provide a comparison between two measurement techniques, mass transfer and thermal methods, and to characterize various coolant flow rate parameters using a variety of gases to further understand scaling adiabatic effectiveness from low to high temperatures in an effort to improve gas turbine engine performance. To provide the necessary background literature and motivation behind the current study, this chapter will focus on various important film cooling topics relating to this research. The topic areas include: general film cooling

overview (Section 2.1), methods of film cooling experimentation (Section 2.2), cooling effectiveness performance considerations (Section 2.3), and scaling (Section 2.4).

2.1 General Film Cooling

Since gas turbine engines were first developed, engine designers have been trying to raise engine temperatures to produce more power and thrust. The turbine inlet temperature has been a limiting factor due to the material limits of the turbine components. The exhaust gases from the combustor have increased to temperatures higher than the material limit of the turbine airfoils the gases are impinging upon. One method of withstanding these exceedingly high temperatures has been developed through several turbine airfoil cooling schemes. Early turbine airfoil cooling was accomplished through internal convective cooling by taking pressurized air from the compressor, bypassing the air around the combustor, and cycling the relatively cool air on the internal side of the turbine airfoils. When internal cooling schemes were not enough to keep the turbine airfoils from failing of prolonged stress at temperatures higher than their material limit, a new cooling scheme was developed. Film cooling takes the compressor bleed air and injects it through small holes in the turbine airfoil to the external surfaces [4].

Film cooling creates a protective layer of relatively cool air that reduces the potential for heat transfer to occur between the hot freestream exhaust gases of the combustor and the turbine airfoil surface. Bogard and Thole [4] provide a review of general film cooling processes and evaluation. Film cooling reduces the heat transfer by lowering the gas temperature near the surface of the airfoil as the heat from the freestream is being convected to the surface. This process is characterized by Newton's Law of Cooling and is shown by the convective heat transfer equation:

$$q" = h(T_{ref} - T_s) \quad (1)$$

where $q"$ is the heat flux, h is the convective heat transfer coefficient, T_{ref} is the reference temperature, and T_s is the surface temperature of the component of interest.

When applying Equation (1) to film cooling, T_{ref} is not apparently known as it involves a mixture of the freestream temperature and the coolant temperature. As the coolant is injected onto the surface and mixes with the freestream, the local temperature near the surface of the airfoils varies greatly downstream of the film cooling hole from the momentum and heat transport in the boundary layer. Therefore, the reference temperature is chosen to be the adiabatic wall temperature, the temperature of the fluid immediately above the surface if the surface were adiabatic. The convective heat transfer equation becomes:

$$q_f" = h_f(T_{aw} - T_s) \quad (2)$$

where $q_f"$ and h_f are the heat flux and heat transfer coefficient with film cooling present, respectively, and T_{aw} is the adiabatic wall temperature. The local heat transfer coefficient and adiabatic wall temperature vary greatly along the surface of the airfoil due to the geometry, placement, and orientation of the film cooling scheme.

The heat transfer dependence on T_{aw} and a film cooling scheme's ability to decrease T_{aw} is often characterized by one of the most important driving variables for predicting airfoil temperatures, the nondimensional parameter known as adiabatic effectiveness:

$$\eta = \frac{T_\infty - T_{aw}}{T_\infty - T_{c,e}} \quad (3)$$

T_∞ and $T_{c,e}$ are the temperatures of the freestream and the coolant at the exit of the hole, respectively. Nondimensionalization of the adiabatic wall temperature allows for experimentalists

to scale test results from ambient to engine conditions. However, to do so, other flow physics need to be scaled properly as well. Previous research has investigated how to properly scale the adiabatic wall temperature using η since there are other flow properties that are temperature dependent, such as the coolant and freestream densities, specific heats, and thermal conductivities [2] [3].

Designing effective film cooling schemes often requires results taken from experiments at ambient conditions and appropriately scaling the results to engine conditions. Choosing the appropriate nondimensional coolant flow rate parameter to match at engine conditions, while accounting for the gas property changes, has been a recent focus of film cooling research [2] [3]. Film cooling scaling research generally surrounds which coolant flow rate parameter can best match adiabatic effectiveness between different conditions, a topic of Section 2.4.

2.2 Methods of Experimentation

To evaluate film cooling effectiveness, quality data must first be gathered to accurately predict the scaling of film cooling experiments from ambient to engine conditions as well as to compare results among sources. The methods of collecting data can be split into two categories: thermal methods and mass transfer methods. These methods can be used to measure adiabatic effectiveness and overall effectiveness. Thermal methods can also be used to measure the heat transfer coefficient. However, adiabatic effectiveness is the focus of the current study. A few of the thermal methods implemented in film cooling effectiveness experimentation are: infrared thermography [2], thermocouples [5], liquid crystal [6], and temperature sensitive paint (TSP) [7] with IR being the most prevalent method used for data collection. Some mass transfer methods used in film cooling experimentation that utilize the heat-mass transfer analogy are measurement techniques that use: pressure sensitive paints [8], gas sampling [9], or naphthalene sublimation

[10], where the latter is used for measurements of the mass transfer analog to the heat transfer coefficient. The comparison of results between thermal experimental techniques and mass transfer experimental techniques is an objective of the current study. The comparison will be accomplished using an IR thermal method and a PSP mass transfer method.

2.2.1 Thermal Method for Determining η

The infrared thermography measurement technique is one of the most popular methods to conduct thermal experiments due to its simplistic experimental set up and testing procedures. Using an IR camera is one of the only requirements with this thermal measurement technique as the test article does not require any surface treatment to measure the surface temperature. The coolant and freestream temperatures can be directly measured by thermocouples, and together with the measured surface temperature, these three temperatures can be used to calculate the apparent adiabatic effectiveness, η_{app}:

$$\eta_{app} = \frac{T_\infty - T_s}{T_\infty - T_{c,e}} \tag{4}$$

Equation (4) is identical in form to η in Equation (3) but instead of T_{aw}, there is the surface temperature, T_s, in its place. This is because no material is truly adiabatic and even using a low thermal conductivity material, such as the flat plate foam model with k = 0.03 W/m-K used by Fischer [2], any conduction through the test article will change the surface temperature reading from the IR camera, resulting in an η_{app} distribution different than the desired η. To account for the conduction present in η_{app}, amongst many, Williams et al. [11] applied a 1-D conduction correction that can be used on most thermally conductive models given by:

$$\eta_T = \frac{\eta_{app} - \eta_0}{1 - \eta_0} \tag{5}$$

η_0 is the same nondimensional surface temperature as η_{app}, with identical internal cooling flow but with no coolant flow on the external surface. Applying the 1-D conduction correction to η_{app} results in the adiabatic effectiveness with thermal measurements η_T. Fischer [2] applied this 1-D conduction correction by calculating the η_0 values using the same IR image as η_{app}. To find T_s for the η_0 calculation, Fischer averaged three points on the surface above the coolant plume and three points below, resulting in a global correction for each individual data point. Fischer used these six points outside the coolant plume but on the same image as the η_{app} since at the chosen locations, the only cause for a lower than freestream temperature was due to conduction into the test article. Typical values for η_0 were between 0.02 and 0.04 in the dataset used by Fischer. The author then applied η_{app} and η_0 to Equation (5) to present the results of η_T.

The thermal measurement technique to calculate adiabatic effectiveness requires the surface temperature of the test article. However, when using an IR camera, the camera captures the thermal radiation off the test surface in a unit of thermal counts. In order to calibrate the thermal radiation to surface temperature, Baldauf et al. [12] implemented a technique using thermocouples attached to the surface along with the IR camera images. The authors used this calibration since the measured thermal radiation is additionally influenced by reflection off the test section walls as well as transmission and emission of the IR camera's sapphire viewing window. Baldauf et al. mounted several thermocouples flush with the test surface downstream of the coolant injection location. For every data point, IR images and thermocouple temperatures were recorded simultaneously, and a curve fit was applied for thermal counts to surface temperature.

Fischer [2] took the calibration technique by Baldauf et al. [12] one step further after noting that the IR camera calibration was heavily influenced by the temperature of the wind tunnel walls. If the temperature of the tunnel walls had not reach thermal equilibrium, the calibration curve would drop by 1%, or 4 K, at higher thermal count values. However, if the tunnel walls were heated up to a consistent temperature, the calibration curves taken over multiple different test days collapsed within ±0.5 K variations. Fischer also found that the location of the thermocouples downstream of the coolant injection influenced the calibration as well. The author noted that it was important to place the thermocouples in areas of relatively low thermal gradients because if a high temperature gradient was present near the reading, an error of about 1 K could arise due to uncertainty in that thermocouple's location.

2.2.2 Mass Transfer Method for Determining η

The pressure sensitive paint measurement technique has become increasingly popular for studies of scaling film cooling adiabatic effectiveness due to its ability to implement a boundary condition analogous to that of an adiabatic wall. This ability removes any conduction errors that are prevalent in thermal measurement methods. The PSP measurement technique is a mass transfer method that invokes the heat-mass transfer analogy to determine adiabatic effectiveness. The heat-mass transfer analogy applies a direct conversion of the heat transferred in a system to the mass transferred in that same system.

The derivation of adiabatic effectiveness for using PSPs with mass transfer measurement techniques begins by utilizing the heat and mass transfer methods developed by Kays et al. [13]. Han and Rallabandi [8] use Kays et al. to show that for a homogeneous fluid, the governing energy equation for the heat transfer method takes the form:

$$G_x \frac{\partial T}{\partial x} + G_z \frac{\partial T}{\partial z} = \alpha \frac{\partial^2 T}{\partial z^2} \tag{6}$$

where G is the net mass-flux vector (ρu) that includes all components of the mixture, some of which may be moving at different velocities due to diffusion, and α is the thermal diffusivity. The boundary conditions for external flow over a flat plate for this study are:

1. At $z = 0$ (wall), $\frac{\partial T}{\partial z} = 0$, and $T = T_{aw}$ (which is a reasonable assumption since the mass transfer method has a boundary condition analogous to an adiabatic wall since there is no mass flux through the surface)
2. At $z > \delta$ (boundary layer thickness), $T = T_\infty$

and for the injected coolant:

3. At $x = 0$, $T = T_c$

The relatively hot mainstream has tracer element or mass concentration of the gas C_∞, and the relatively cold coolant has tracer element or mass concentration of the gas C_c. Applying the heat-mass transfer analogy, the governing energy equation becomes:

$$G_x \frac{\partial C}{\partial x} + G_z \frac{\partial C}{\partial z} = \mathcal{D} \frac{\partial^2 C}{\partial z^2} \tag{7}$$

where $\mathcal{D}$ is the mass diffusion coefficient. The boundary conditions become:

1. At $z = 0$ (wall), $\frac{\partial C}{\partial z} = 0$, and $C = C_w$ (C_w is the concentration at the wall)
2. At $z > \delta$, $C = C_\infty$

and for the injected coolant:

3. At $x = 0$, $C = C_c$

Now that the governing equations have been developed, Equation (2) as written in terms of temperature, needs to be converted to terms of mass concentration and this is accomplished by

applying the heat-mass transfer analogy. The heat-mass transfer analogy was first developed by Schmidt and Nusselt based on the governing equations for momentum, heat, and mass transfer to relate information about a heat transfer process to that of a mass transfer process [14]. The Nusselt number, Nu, is a nondimensional form of the heat transfer coefficient and the Sherwood number, Sh, is a nondimensional form of the mass transfer coefficient. The two processes, heat transfer and mass transfer, are analogous for two fluids when the Prandtl number, Pr, is equal to the Schmidt number, Sc, and as such:

$$Nu = Sh \quad \text{when} \quad Pr = Sc$$

This statement expresses the heat-mass transfer analogy.

Application of the heat-mass transfer analogy requires the Lewis number, Le, to be near unity. The ratio of the Prandtl number to the Schmidt number results in the Lewis number and the correlation becomes:

$$Le = 1 = \frac{Pr}{Sc} = \frac{\frac{\nu}{\alpha}}{\frac{\mu}{\rho \mathcal{D}}} = \frac{\alpha}{\mathcal{D}} \equiv \frac{thermal\ diffusivity}{mass\ diffusivity} \tag{8}$$

Which shows that the thermal and mass diffusion terms must be equal.

Applying the heat-mass transfer analogy to convert the energy equation in terms of temperature to that of mass concentrations require that $Le = 1$. Thus, the appropriate nondimensional solutions can become identical [8]:

$$\eta_T = \frac{T_\infty - T_{aw}}{T_\infty - T_{c,e}} \rightarrow \frac{C_\infty - C_w}{C_\infty - C_c} = \eta_M \tag{9}$$

When a foreign gas is used as a coolant, C_w becomes a reduction in the O_2 concentration, since O_2 is the tracer species for the PSP used in this study, due to the film created by the foreign gas coolant having a lower O_2 concentration than that of the freestream air. Also, C_c at the foreign

gas coolant injection location, $x = 0$, will have a concentration of zero O_2 since the coolant has not had a chance to mix with the freestream. Since the oxygen properties are known when air is used as the freestream, C_∞ becomes $C_{O_2,\infty}$ and the concentration of oxygen at the surface, or wall, is unknown when a foreign gas coolant is used, C_w is termed $C_{O_2,w}$. The equation for adiabatic effectiveness with respect to mass concentration of the gas becomes:

$$\eta_M = \frac{C_\infty - C_w}{C_\infty - C_c} = \frac{C_{O_2,\infty} - C_{O_2,w}}{C_{O_2,\infty} - 0} = 1 - \frac{C_{O_2,w}}{C_{O_2,\infty}} \tag{10}$$

A detailed explanation of how pressure sensitive paints determine the partial pressure of oxygen on a surface of interest is given in the following section, Section 2.2.3, and the theory of applying the partial pressures of O_2 on the surface to determine η_M is given in Section 2.2.4. However, Equation (10) is in terms of mass concentrations, not the partial pressures determined by the PSP. Also, to account for coolant gases with varying densities, concentration is converted to mole fractions, $\mathcal{X}$, and molecular weights, $\mathcal{M}$. $\mathcal{X}_{O_2,\infty}$ and $C_{O_2,\infty}$ are constant regardless of pressure and temperature. Though, when a foreign gas in injected onto the surface, the local concentrations will vary. $\mathcal{X}_{O_2,w}$ and the chemical composition of the film at the wall will change with the interaction of the freestream and the foreign gas coolant, resulting in the molecular weight of the mixture at the wall, $\mathcal{M}_{mix,w}$. Equation (10) becomes:

$$\eta_M = 1 - \frac{C_{O_2,w}}{C_{O_2,\infty}} = 1 - \frac{\mathcal{X}_{O_2,w}\left(\frac{\mathcal{M}_{O_2}}{\mathcal{M}_{mix,w}}\right)}{\mathcal{X}_{O_2,\infty}\left(\frac{\mathcal{M}_{O_2}}{\mathcal{M}_\infty}\right)} = 1 - \frac{\mathcal{X}_{O_2,w}\mathcal{M}_\infty}{\mathcal{X}_{O_2,\infty}\mathcal{M}_{mix,w}} \tag{11}$$

Next, the molecular weight of the mixture inside the film needs to be determined. It is considered a mixture of its component gases: air and coolant:

$$\mathcal{M}_{mix,w} = \mathcal{X}_{\infty,w}\mathcal{M}_\infty + \mathcal{X}_{c,w}\mathcal{M}_c \tag{12}$$

and recognizing that

$$\mathcal{X}_{O_2}\mathcal{M}_{O_2} + \mathcal{X}_{N_2}\mathcal{M}_{N_2} = \mathcal{X}_{\infty}\mathcal{M}_{\infty}$$

where the freestream air is considered to be a mixture consisting of mainly N_2 and O_2. The O_2 percentage in air by volume is considered to be known and the mole fraction is also known, which can be substituted in:

$$\mathcal{X}_{\infty,w} = \mathcal{X}_{O_2,w}(1 + \frac{\mathcal{X}_{N_2,\infty}}{\mathcal{X}_{O_2,\infty}})$$

It is also considered that

$$\mathcal{X}_{c,w} + \mathcal{X}_{\infty,w} = 1$$

since all mole fractions must add up to unity. Using these equations and substituting into Equation (12), the molecular weight of the mixture becomes:

$$\mathcal{M}_{mix,w} = \mathcal{X}_{O_2,w}(1 + \frac{\mathcal{X}_{N_2,\infty}}{\mathcal{X}_{O_2,\infty}})\mathcal{M}_{\infty} + \left(1 - \mathcal{X}_{O_2,w}(1 + \frac{\mathcal{X}_{N_2,\infty}}{\mathcal{X}_{O_2,\infty}})\right)\mathcal{M}_c \qquad (13)$$

Now, Equation (13) can be substituted back into Equation (11) so the adiabatic effectiveness with respect to mass transfer is a function of the mole fraction of oxygen and parameters to be measured during the experiment.

Using Dalton's Law of partial pressures, the ratio of partial pressure of a constituent gas to the static pressure, P_s, is identical to the mole fraction of that constituent gas resulting in:

$$\mathcal{X}_{O_2,w} = \frac{p_{O_2,w}}{P_s}$$

where p_{O_2} is the partial pressure of oxygen. Equation (11) becomes:

$$\eta_M = 1 - \frac{\mathcal{X}_{O_2,w}\mathcal{M}_{\infty}}{\mathcal{X}_{O_2,\infty}\left(\mathcal{X}_{O_2,w}(1 + \frac{\mathcal{X}_{N_2,\infty}}{\mathcal{X}_{O_2,\infty}})\mathcal{M}_{\infty} + \left(1 - \mathcal{X}_{O_2,w}(1 + \frac{\mathcal{X}_{N_2,\infty}}{\mathcal{X}_{O_2,\infty}})\right)\mathcal{M}_c\right)}$$

Noting that:

$$\mathcal{X}_{O_2,\infty}\left(1+\frac{\mathcal{X}_{N_2,\infty}}{\mathcal{X}_{O_2,\infty}}\right)=\mathcal{X}_{\infty,\infty}=1$$

η_M reduces by:

$$\eta_M=1-\frac{\mathcal{X}_{O_2,w}\mathcal{M}_\infty}{\mathcal{X}_{O_2,\infty}\mathcal{M}_\infty+\left(\mathcal{X}_{O_2,\infty}-\mathcal{X}_{O_2,w}\mathcal{M}_c\right)}$$

$$\eta_M=1-\frac{1}{1+\left(\left(\frac{\mathcal{X}_{O_2,\infty}}{\mathcal{X}_{O_2,w}}-\frac{\mathcal{X}_{O_2,w}}{\mathcal{X}_{O_2,w}}\right)\frac{\mathcal{M}_c}{\mathcal{M}_\infty}\right)}$$

$$\eta_M=1-\frac{1}{1+\left(\left(\frac{\mathcal{X}_{O_2,\infty}}{\mathcal{X}_{O_2,w}}-1\right)\frac{\mathcal{M}_c}{\mathcal{M}_\infty}\right)}$$

$$\eta_M=1-\frac{1}{1+\left(\left(\frac{p_{O_2,\infty}}{p_{O_2,w}}-1\right)\frac{\mathcal{M}_c}{\mathcal{M}_\infty}\right)} \tag{14}$$

where $\frac{p_{O_2,\infty}}{p_{O_2,w}}$ is determined from the intensity and pressure fields taken from reference and test conditions with the PSP. A detailed description of how $\frac{p_{O_2,\infty}}{p_{O_2,w}}$ is determined in this study is given in Section 3.4 and the accepted standard process is described in Section 2.2.4. The form of Equation (14) for adiabatic effectiveness with the heat-mass transfer analogy using the PSP measurement technique is in agreement with [3] and [8].

Han and Rallabandi [8] presented an overview of the PSP measurement technique using the heat-mass transfer analogy to determine film cooling effectiveness. The review encompassed the theoretical basis behind the experimental technique as well as the accepted standard process of experimentation and provides summaries of several results in the open literature, consisting of many different cooling configurations. The authors communicated the importance that the PSP

measurement technique allows high resolution contours, especially in high thermal gradient regions such as near the cooling hole exit, without being exposed to conduction errors present in the results when experimenting with thermal methods. Han and Rallabandi gave a similar derivation to the one shown in this study starting with Equation (6) and ending with the same form of adiabatic effectiveness using the mass transfer analogy shown in Equation (14). However, instead of beginning the mass transfer analogy stating that *Le* needs to be unity as shown in Equation (8), the authors suggested that for the boundary conditions of Equation (6) and Equation (7) to be identical, along with the nondimensional solutions, the turbulent Lewis number, Le_{turb}, needs to be of unity:

$$Le_{turb} = 1 = \frac{\epsilon_T + \alpha}{\epsilon_M + \mathcal{D}}$$

where ϵ_T is the turbulent thermal diffusivity and ϵ_M is the turbulent mass diffusivity. The authors state that this assumption is valid over the surface of a turbine blade due to the high Re and secondary mechanisms, such as vortices and wakes, that create a highly turbulent flowfield. However, the assumption may not be valid over the leading edge region where the flow is either laminar or in transition.

2.2.3 PSP Experimental Theory

Before an explanation of the theory behind the standard process to implement a pressure sensitive paint to measure $p_{O_2,\infty}$ and $p_{O_2,w}$ on the surface to determine η_M, the background behind how a PSP determines the partial pressure of O_2 on the surface, while removing the dependence on temperature, is in order. The PSP measurement technique is based on the sensitivity of luminescent molecules within the paint to the presence of oxygen molecules. The PSP used in this

study was developed by Innovative Scientific Solutions, Inc. (ISSI) [15]. PSPs are comprised of two main parts, an oxygen sensitive fluorescent molecule, known as the signal probe, and an oxygen-permeable polymer binder. A single component PSP process can be visualized in Figure 1. When a luminescent molecule absorbs a photon from an excitation energy source such as an LED light, at a wavelength of about 405 nm, that molecule gets excited to a higher energy state. At the excited energy state, the molecule emits a photon of a longer wavelength and then returns to the ground state. The pressure sensitivity of the luminescent molecules embedded within the PSP results from the interaction of an excited luminophore with an oxygen molecule. During an interaction, the excited luminophore transfers energy to the vibrational mode of the oxygen molecule. The oxygen molecule's resulting recovery back to the ground state lacks radiation, a process known as oxygen quenching, and does not release a photon of longer wavelength. The rate at which the oxygen quenching process competes with the excited luminophores emitting photons is dependent upon the partial pressure of oxygen on the surface of the PSP. When there is a greater amount of oxygen present on the surface, the oxygen quenching process dominates and results in less emission from the luminophores in the paint and therefore, less intensity of fluorescence. Since PSPs are sensitive to the partial pressure of oxygen on their surface, oxygen is known as the tracer gas or species. The fluorescent, or luminescent, intensity emitted by the paint is what the detector, commonly a CCD camera, captures. This intensity captured by the camera is converted to the partial pressure of oxygen using a calibration of that PSP.

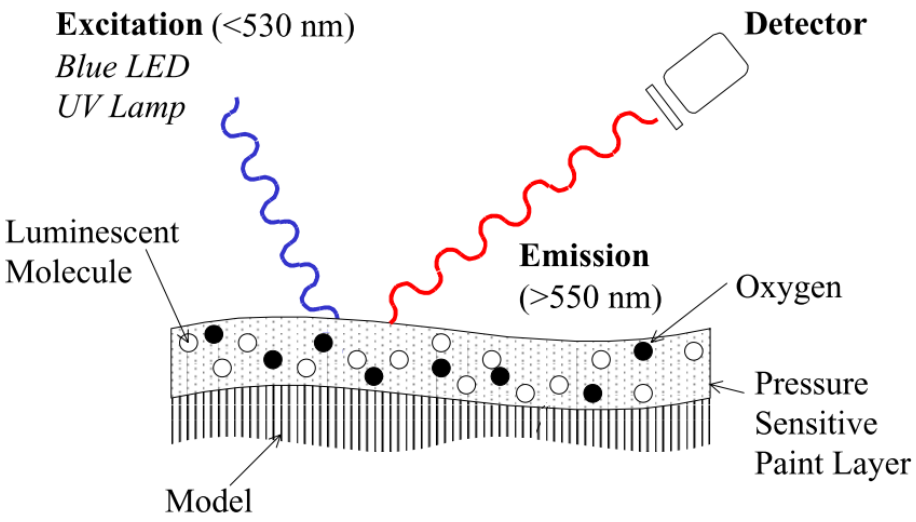

Figure 1: Single Component Pressure Sensitive Paint [15].

There are many sources of error that can result from PSP testing which include: camera shot noise, stray light other than the illumination LED, paint degradation from excitation source exposure, model deformation during imaging, illumination, area of image focus, and temperature. ISSI has worked to develop a system to combat and minimize all these sources of error and state that temperature and illumination have seen the greatest sources of error [16]. Many of the effects from illumination changes and temperature have been resolved through the production of a binary PSP. A comparison between a single component PSP and a binary PSP is shown in Figure 2. Binary PSPs employ a reference probe to a typical single component PSP. The reference probe excites at the same wavelength as the pressure sensitive probe but fluoresces at a spectrally distinct wavelength as seen in green in Figure 2 (b) compared to no reference probe in Figure 2 (a). The reference probe is used to correct for variations in the illumination by making the system response a function of pressure and temperature only.

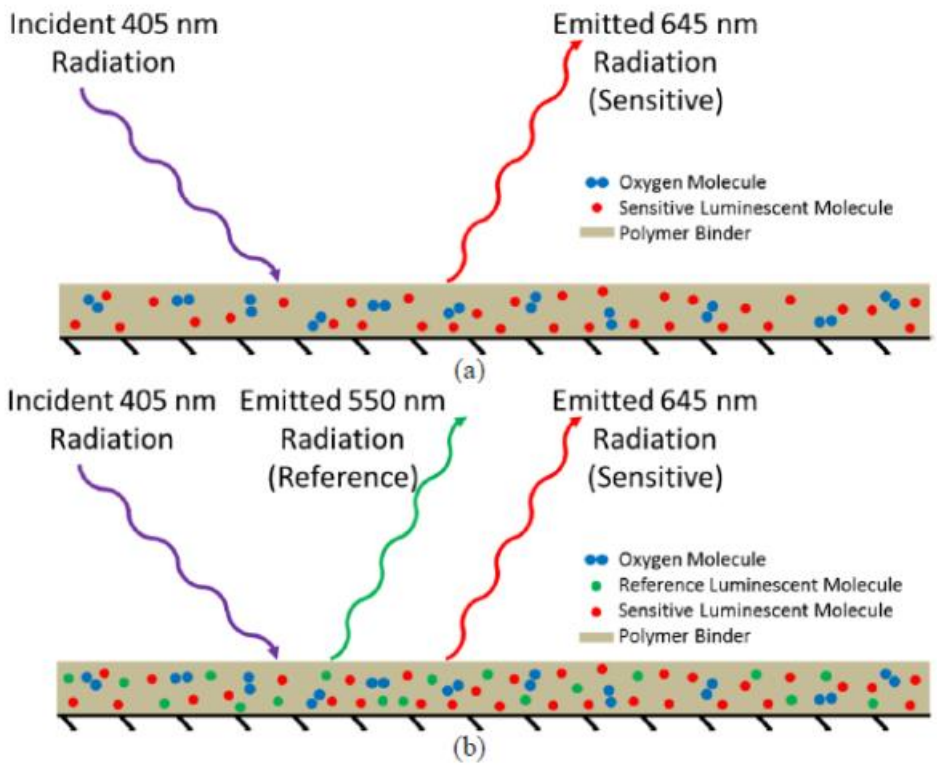

Figure 2: a) Single component PSP and b) Binary PSP [17].

ISSI has developed a process to reduce the system response from a function of four variables to a function of temperature and pressure only. As described by ISSI [18], the luminescent intensity (F), of a PSP is a function of pressure (P), temperature (T), luminophore concentration (N), and illumination (L) which can be represented by:

$$F = f(P, T, N, L) \tag{15}$$

Accounting for variations in illumination, luminophore concentration, and paint layer thickness involves a ratio of a "wind off" image to that of a "wind on" image. By using this ratio, it is assumed that the illumination at all points on the model surface remain constant throughout testing. This means that the model and illumination source need to remain unmoved and undeformed. Any error resulting from slight movement of either the test object or illumination

source can be more pronounced in tests at low speeds where small changes in pressure result in small changes of illumination. A wind off image consists of capturing a picture while illuminating the sample with the wind tunnel turned off but at testing temperature. A wind on image is taken illuminating the sample with the wind tunnel on, at testing temperature, and with coolant flowing, whether that be air or a foreign gas. A foreign gas is used as a coolant since the tracer species, oxygen, is not present in the gas, and therefore, the PSP can detect the partial pressure of oxygen from the freestream on the test surface and discern the placement of the foreign gas coolant.

The ratio of the wind off to wind on images uses the luminescence of the reference probe, subscript R, to account for variations in the signal, or pressure sensitive, probe, subscript S, that are caused by variations in paint illumination. Since the reference and signal probe's responses are linearly proportional to the local illumination of the probes and the probes spatial density within the paint, the ratio, r, becomes the following function:

$$F_S = f_S(P, T, N_S, L)$$

$$F_R = f_R(P, T, N_R, L)$$

$$r(P,T) = \frac{F_S(P,T)N_S * L}{F_R(P,T)N_R * L} = \frac{F_S(P,T)N_S}{F_R(P,T)N_R}$$

The dependence of the ratio on the illumination of the probes has been removed, but the ratio remains a function of pressure, temperature, and luminophore concentration. The PSP's composition of the luminophores is imperfectly homogeneous and therefore, the ratio of signal to reference probe concentration $\frac{N_S}{N_R}$ is not uniform throughout the paint and thus, not constant. To then remove the variation of concentration between the two probes, a wind on and wind off ratio of ratios is used between a reference and test condition. The ratio of ratios determines the

luminescent intensity, given by the variable I, where the subscript 0 is for the reference condition. The system response is now a function of only pressure and temperature:

$$I(P,T) = \frac{r_0(P_0,T_0)\frac{N_S}{N_R}}{r(P,T)\frac{N_S}{N_R}} = \frac{r_0(P_0,T_0)}{r(P,T)} \tag{16}$$

The image processing involved in applying the ratio of ratios is accomplished in three steps. First, the ratio of the signal probe to the reference probe is computed for each condition of wind off and wind on which eliminates the illumination from the system. Second, the wind on ratio of signal to reference probe is mapped onto the wind off ratio image where the probe concentration effects are eliminated. Third, the background noise is accounted for with the background images. Two background images are used where the light is turned off for both the wind off and wind on scenarios. Although ISSI's process suggested a background image for each the wind on and the wind off conditions, the background noise should remain the same with each flow scenario. Therefore, requiring only one background image to be taken for use as the background image for both the wind on and wind off conditions. The rest of the discussion in this study will refer to the background images as one image. One convenience of working with this approach is that every wind on image can be compared to a single wind off image, assuming the paint has not degraded between images. This approach is also a benefit of using a binary PSP and can only be used for a binary PSP where the reference and signal probes are excited by the same illumination source but the luminescence of the two probes are spectrally different, so they can be filtered through optical lenses. A new method of applying the ratio of ratios with the wind off and wind on images for experimentation and data reduction was developed in this study and is discussed in Section 3.4.

Now, the system is a function of pressures and temperatures but needs to be a function of only pressure as it relates to the illumination of the test surface. Temperature compensation was

accomplished by a calibration curve relating the intensity of luminescence to the partial pressure of oxygen by curves that collapse over a range of temperatures. The calibration curve determined by ISSI for the specific paint used on the model in this study is shown in Figure 3. The accuracy of the calibration curve was 50 Pa/K. ISSI related the luminescent intensity from a particular PSP to the pressure and temperature experienced by the paint using their signature PSP calibration chamber [15]. To summarize the calibration chamber and the process of determining the functional relationship between intensity and the partial pressure of oxygen, first, a small aluminum coupon was painted with the PSP and then mounted onto a Peltier thermo-electric cooler where it was then mounted inside the PSP calibration chamber. The pressure inside the chamber was controlled using a Ruska pressure controller at the same time an Omega temperature controller regulated the temperature. The coupon was illuminated with an array of 76 LEDs from an ISSI LM-2 Lamp to produce an excitation wavelength of 405 nm. The luminescence from the painted coupon was captured from a Canon CCD camera through a long-pass filter to filter out the reference probe's emitted photon of about 550 nm and capture the signal probe at about 645 nm. The calibration data acquisition started at a reference condition of 298 K and 14.696 psia. The pressure and temperature were then varied over a wide range within the calibration chamber. The luminescent intensity from the painted sample was recorded at each condition. Once all the data was acquired, the ratio of reference to signal intensities, $I(P,T)$, over the data points was computed and plotted. The calibration curve plotted on intensity versus pressure with lines of different temperatures can be collapsed to one curve fit resulting in a calibration curve over a range of temperatures that was nearly independent of temperature.

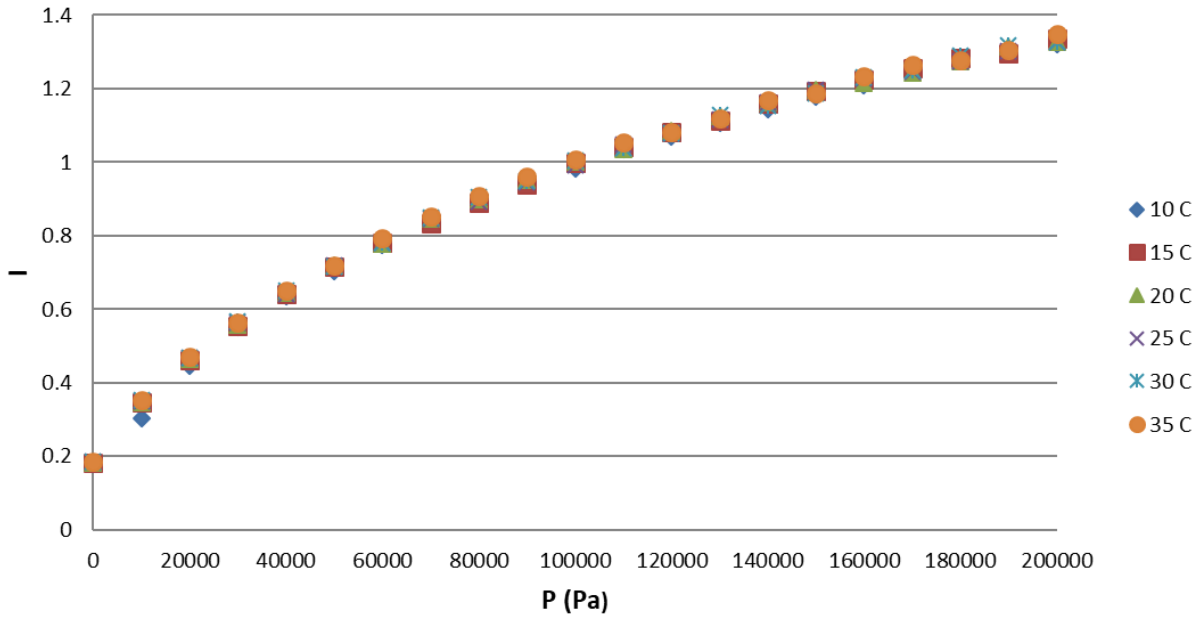

Figure 3: ISSI's BinaryFIB calibration curve for the PSP used in this study.

The ability of a binary PSP to remove temperature from the function of light intensity captured off the surface is an important feature of this study. By having the PSP's ability to accurately detect the partial pressure of oxygen on the surface over a range of temperatures allows the temperature of the coolant to be different than the temperature of the freestream. As a reminder, one of the objectives of this study is to compare mass transfer methods, using a PSP experimental technique, to thermal methods, using an IR experimental technique, with minimal differences between the two. Having the capability of acquiring accurate results using the PSP technique with a temperature difference between the coolant and the freestream allows a closer match to experimental conditions used with the IR technique. Now, temperature differences can be matched, and in turn, the flow physics, using both techniques limiting the changes between the PSP and IR experiments.

PSPs can be used in experimentation as a technique that provides non-intrusive measurements of barometric pressure at high resolution on wind tunnel model surfaces to which

the PSP has been applied. Low-speed wind tunnel tests were a target for PSP experimentation for many years. However, early PSP tests in wind tunnels with flows below Mach 0.3 proved challenging [16]. Low-speed wind tunnel testing was difficult because error was more pronounced since small changes in pressure result in small changes in illumination. ISSI has demonstrated the recent production PSPs to be accurate to 50 Pa/K, as was shown for the calibration of the paint used in this study. The testing done by ISSI has refined the PSP measurement technique in low-speed, large wind tunnels to compensate for errors that were reported in early PSP testing. The system now consists of a binary PSP, a single camera with a long-pass filter that has remote focus/zoom/aperture lenses, illumination provided by 400 nm LEDs operated by a pulse generator for the correct duration of illumination and exposure, and a refined data processing program called ProImage.

2.2.4 Theory of Determining Partial Pressures with PSPs

Han and Rallabandi [8] explain the standard process of experimentation for determining adiabatic effectiveness using the PSP technique and how to acquire the unknown values in the equation for η_M, which are the values in the ratio $\frac{p_{O_2,\infty}}{p_{O_2,w}}$ in Equation (14). The unknown values are the partial pressure of O_2 at the wall when air is flowing as the coolant, $p_{O_2,\infty}$, and the partial pressure of O_2 at the wall when a foreign gas is flowing as the coolant, $p_{O_2,w}$. Note that the process explained in [8] is for a single component PSP that has only one luminophore (signal probe) that is temperature and pressure sensitive. Therefore, the freestream and the coolant are required to be at the same temperature for experiments using single component PSP. The following explanation of the standard process can be applied to both a single component PSP and a binary PSP with the exception of experimenting at different temperatures for the coolant and the freestream. The new

process developed in this study applying ISSI's ratio of ratios with a binary PSP is described in detail in Section 3.4.

The standard process explained by Han and Rallabandi [8] required a series of four images, or tests, to be taken and averaged for each data point. First, each image was a series of several frames, or snapshots, which were then averaged. The authors state an average of 200 frames was common. The first image involved the room completely dark with the excitation source turned off to capture the dark room background noise intensity, called the background image. The second image taken was the wind off image which involved running the wind tunnel until testing temperatures were reached, shutting the tunnel off so there was no freestream velocity, and then capturing an image with the excitation source turned on. The third and fourth images taken were the wind on images which involved running the tunnel at the desired testing Re and temperature and taking an image with air running as the coolant at the desired coolant flow rate, the third image, and then taking an image with a foreign gas running as the coolant at the desired coolant flow rate, the fourth image. The images recorded are of the light intensity captured by the camera from the excited luminophores fluorescing from the surface of the PSP. The intensities are as follows: I_B is the background image intensity, I_R is the wind off image intensity, and I_T is the wind on test image intensity for either the air as coolant or foreign gas as coolant scenarios. Han and Rallabandi describe the process to convert the light intensities, *I's*, to the partial pressure of oxygen on the surface for either air or foreign gas as the coolant, p_{O_2}, through the relationship that involves the Stern-Volmer Equation, adapted from [8]:

$$\frac{I_R - I_B}{I - I_B} = A(T) + B(T)\frac{p_{O_2}}{p_{O_2,R}}$$

where

$$A(T) = A(T_R)\left(1 + \frac{E_{nr}}{RT_R}\left(\frac{T - T_R}{T_R}\right)\right)$$

$$B(T) = B(T_R)\left(1 + \frac{E_p}{RT_R}\left(\frac{T - T_R}{T_R}\right)\right)$$

In the provided equations, *A(T)* and *B(T)* are the Stern-Volmer constants, subscript *R* is at the wind off reference, or atmospheric conditions, E_{nr} is the Arrhenius activation energy for a nonradiative process, E_p is the activation energy for oxygen diffusion, and *R* is the universal gas constant. However, rather than solve for the Stern-Volmer equations, a calibration chamber can be used to convert light intensities to the partial pressure of O_2, a process that was described Section 2.2.3.

2.3 Cooling Effectiveness Performance Considerations

There are factors that affect film cooling performance, such as hole geometry and configuration, airfoil geometry, turbulence, and coolant flow rate. Hole geometry and configuration breaks out into several factors to include, but not limited to: shape of the hole, coolant injection angle and compound angle of the coolant hole, spacing between the hole, length of the hole, spacing between rows of holes, and number of rows. Airfoil geometry also breaks into several factors, not limited to: surface curvature, surface roughness, and hole location at the leading edge, main body, blade tip, and end wall. Freestream turbulence created from the combustor has been shown to affect the cooling performance of the turbine components. Coolant flow rate is discussed in Section 2.4.

The majority of early film cooling research revolved around standard cylindrical holes with varying injection angles [19]. Cylindrical holes are easier to manufacture than shaped holes which allows a scaling experimentalist to focus on the scaling technique or parameter of interest, rather

than hole geometry. However, cylindrical holes are prone to jet separation at higher coolant flow rates. Higher flow rates lead to higher momentum flux ratios, the parameter that best scales jet separation. This led to a desire for hole geometries that would better distribute the coolant on the surface and prevent coolant jet separation. The fan-shaped hole and laid-back fan-shaped holes increase the area of the hole near the injection point, slowing down the flow, preventing the coolant from detaching [19] [20].

Gritsch et al. [19] were amongst the first to study the differences in the three hole geometries shown in Figure 4, which also shows standard angles chosen for injection angles and expanded exit angles. The fan-shaped and laid-back fan-shaped holes were found to provide a decreasing fluid momentum as the coolant flows from the cylindrical tube to the expanded geometry hole exit. The fan-shaped expanded exit also resulted in more lateral spreading of the coolant onto the surface. Due to the flow decreasing in momentum, the fluid stayed attached to the surface further downstream of the hole exit for the expanded exit holes as compared to the cylindrical hole. The increase in lateral spreading of the coolant, along with the decreased momentum allowing the coolant to stay attached, resulted in an increased cooling effectiveness over the surface downstream of the hole [19].

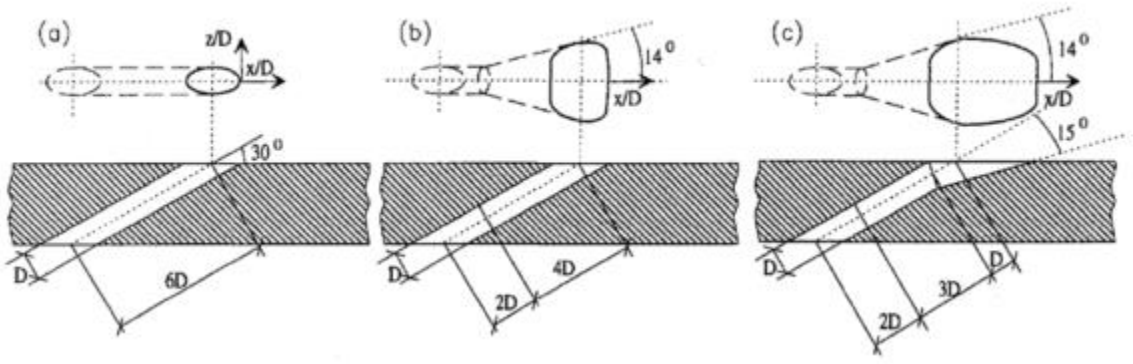

Figure 4: Hole geometries: a) cylindrical, b) fan-shaped, and c) laid-back fan-shaped [19].

Expanded exit holes have many different geometries and injection schemes that can be optimized leading to many propriety hole designs by turbine manufacturing companies. Thus, Schroeder and Thole [20] set out to create a shaped hole that would be representative of the increased effectiveness achieved by propriety hole designs while also offering the community a baseline for comparison purposes. The hole design by Schroeder and Thole, to also be used in the current study, is named the "triple 7" hole, or 7-7-7 hole, seen in Figure 5. The hole is named 7-7-7 because the hole expands seven degrees in both the positive and negative lateral directions from the centerline, two 7's, and has a seven-degree laid back angle, the third 7. Another noteworthy feature of the 7-7-7 hole is the 30° injection angle to the surface. The current study will utilize a flat plate with a single zero-degree compound angle 7-7-7 shaped hole.

	Range Common in Literature	7-7-7 Shaped Hole
Injection Angle, α	30 to 55°	30°
L_m/D	1 to 4	2.5
L_{lat}/D, L_{fwd}/D	1.6 to 9.5	3.5
L/D	2.8 to 11.5	6
Laidback Angle, β_{fwd}	2 to 25°	7°
Lateral Angle, β_{lat}	2 to 18°	7°
P/D	2.8 to 8	6
Coverage Ratio, t/P	0.3 to 0.8	0.35
Area Ratio, AR	2.5 to 4.7	2.5
Sharpness of Inlet and Breakout Edges	Usually Sharp	Sharp
Rounding of Four Edges Inside Diffuser, R/D	0 to 0.5	0.5

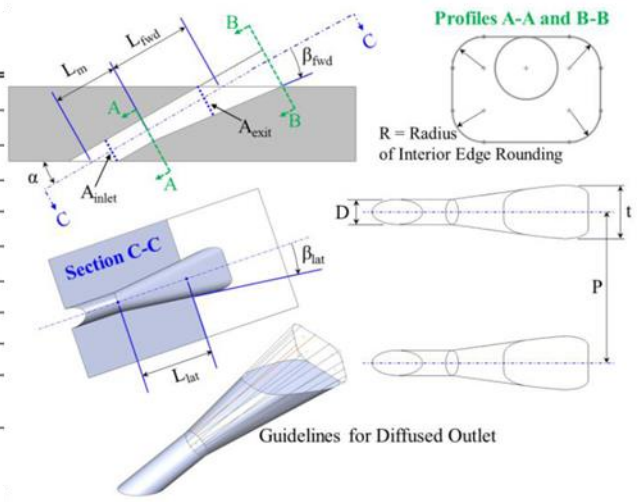

Figure 5: 7-7-7 hole geometry and layout [20].

Another influential effect on film cooling performance is the freestream turbulence created from the combustor upstream of the turbine [4]. An increased turbulence level has been shown to decrease the film cooling effectiveness. Turbulence creates mixing of the freestream flow and the coolant flow on the surface of the turbine blades. When the turbulence is increased, the hot air is

more readily mixed with the coolant flow and removes the coolant film from the surface, replacing it with hot freestream gases, thus increasing the temperature near the surface of the airfoil.

Studies of higher levels of freestream turbulence are usually limited by the grid used to generate turbulence levels where the size of the eddies are on the order of the bars used to make the grid [4]. Common turbulence studies, represented by the work of Kadotani and Goldstein [21], were limited to turbulence levels of 8% with integral length scales on the order of one-third the diameter of the coolant hole exit diameter. With these conditions, the authors found that there was a significant decrease in film cooling effectiveness, up to 15% at lower coolant flow rates, and the decrease in film cooling effectiveness lessened at higher coolant flow rates.

2.4 Scaling

Due to the high cost and difficulty experimenting at gas turbine temperatures, low temperature tests are often conducted. In these experiments, experimentalists can determine how well a given cooling scheme can perform. The question then arises as to what film cooling flow rates should be matched in low temperature tests to scale results to predict conditions at engine temperatures. Thus, in general gas turbine film cooling experimentation, scaling is the process of predicting results at high temperature engine conditions through nondimensional parameters at low temperature test settings. Geometrically scaled up models are often used in low temperature tests as a surrogate to small engine components to achieve greater fidelity in experimentation and to allow the operation of wind tunnels at lower freestream velocities. Lower freestream velocities are achievable while maintaining the same Reynolds number because as the geometrically scaled up model results in a greater length scale, the velocity is decreased.

2.4.1 Scaling Parameters

Adiabatic effectiveness is a nondimensional parameter that is used to scale the adiabatic wall temperature from low temperature test settings up to engine temperatures. Thus, η can be used to predict the adiabatic wall temperature at engine conditions. To properly scale adiabatic effectiveness, the bulk of film cooling research has revolved around the density ratio (*DR*) and several coolant flow rate parameters described by Bogard and Thole [4]: velocity ratio (*VR*), mass flux ratio, also known as blowing ratio (*M*), and momentum flux ratio (*I*). These ratios are defined in Equations (17), (18), (19), and (20) where ρ_∞ is the freestream density, ρ_c is the density of the coolant, u_∞ is the velocity of the freestream, and u_c is the velocity of the coolant.

$$DR = \frac{\rho_c}{\rho_\infty} \tag{17}$$

$$VR = \frac{u_c}{u_\infty} \tag{18}$$

$$M = \frac{\rho_c u_c}{\rho_\infty u_\infty} \tag{19}$$

$$I = \frac{\rho_c u_c^2}{\rho_\infty u_\infty^2} \tag{20}$$

The density ratio describes the density variation between the coolant and the freestream, and the velocity ratio scales the velocities between the coolant jet and the freestream air. However, to consider the flow rate and density variations, the blowing ratio is used to scale the mass flux between the coolant and the freestream. The turning of the coolant jet into the freestream is also important to characterize to avoid jet separation, which decreases film cooling effectiveness. This leads to the momentum flux ratio. *I* scales the dynamics of the force of the coolant jet interacting with the freestream air.

It has been reported in the literature that the blowing ratio has the ability to scale the thermal transport capacity of the coolant jet [4] [5]. However, the blowing ratio only has the partial ability to scale the thermal energy transport of the coolant jet because of its relation to $c_p \rho U$ through ρU. Though, it is clearly noted that c_p does not appear in Equation (19), for *M*, and cannot handle the thermal capacity of the coolant jet. This discrepancy led to another, unconventional scaling parameter shown in Equation (21). The advective capacity ratio, *ACR*, accounts for thermal energy transport by multiplying *M* by the specific heat ratio of the coolant to the freestream, $CpR = \frac{c_{p,c}}{c_{p,\infty}}$, [22] [23]. The reader should note that *ACR* was first named the heat capacity ratio, *HCR*, in [22] but later renamed *ACR* in [23] to avoid confusion with a ratio of coolant-to-freestream heat capacities, $\frac{(\rho c_p)_c}{(\rho c_p)_\infty}$.

$$ACR = \frac{\rho_c c_{p,c} u_c}{\rho_\infty c_{p,\infty} u_\infty} \tag{21}$$

Many studies have been performed analyzing these coolant flow rate parameters to determine which parameters can be useful in various flow conditions and cooling schemes. The following sections in Chapter 2 will discuss various studies that analyzed coolant flow rate parameters and gas property effects.

2.4.2 Density Effects

The density ratio is one of the most predominant parameters considered in early film cooling scaling studies as it has been shown to have the most influential effect scaling adiabatic effectiveness. Many film cooling tests are conducted at density ratios that do not match engine conditions. At engine conditions, the *DR* is about two since coolant temperature in gas turbine

operations is about half the engine freestream temperature. The *DR* is commonly not matched due to the difficulty and cost to replicate in lab environments [4]. If *DR* cannot be matched in low temperature test conditions, the other stated scaling parameters cannot be simultaneously matched to perform a test. Many studies have been conducted on which matched parameter: *M*, *I*, or *VR* can best scale adiabatic effectiveness while potentially accounting for density effects [5]. However, recent research has been looking into effects of other gas properties, such as specific heat, and their influence on scaling adiabatic effectiveness [22] [23].

Sinha et al. [5] conducted one of the first film cooling effectiveness studies considered to be a baseline for characterizing the effect of density differences for scaling adiabatic effectiveness using the common scaling parameters: *VR*, *M*, and *I*. In the study, cooling effectiveness was studied using a row of inclined, cylindrical holes that injected cryogenically cooled air to obtain a range of density ratios from 1.2 to 2 to characterize the scaling abilities of *M*, *I*, and *VR*. The test article used was a flat plate made of low k, 0.027 W/m-K, Styrofoam to reduce conduction errors. A 3-D conduction correction was also applied to the heat transfer analysis to further reduce conduction errors. The test plate was fitted with thin ribbon thermocouples to measure the surface temperature. To further reduce conduction errors, the thermocouples were chosen to have a large surface area of the ribbon relative to the cross-sectional area. Thermocouples were placed to measure temperatures along the jet centerlines as well as laterally to determine a spanwise averaged adiabatic effectiveness. By independently varying *DR* and the mass flow rate of the coolant, a range of *M*s, *I*s, and *VR*s were able to be evaluated for their efficacy in scaling η. *M* ranged from 0.25 to 1 and in conjunction with a varying *DR*, allowed a wide range of *I* and *VR* to be observed. Values for the scaling parameters can be seen in Table 1. The centerline effectiveness holding each scaling parameter, *M*, *I*, and *VR*, constant while varying density ratio can be seen in Figure 6.

Table 1: Range of scaling parameters in experiment by Sinha et al. [5].

Case No.	Density Ratio	Mass Flux Ratio	Velocity Ratio	Momentum Flux Ratio
1	1.2	0.25	0.208	0.05
2	1.2	0.50	0.42	0.208
3	1.2	0.60	0.50	0.30
4	1.2	0.78	0.65	0.50
5	1.2	1.00	0.83	0.83
6	1.6	0.57	0.35	0.20
7	1.6	0.80	0.50	0.40
8	1.6	0.90	0.56	0.50
9	1.6	1.00	0.625	0.625
10	2.0	0.50	0.25	0.125
11	2.0	0.80	0.40	0.32
12	2.0	1.00	0.50	0.50

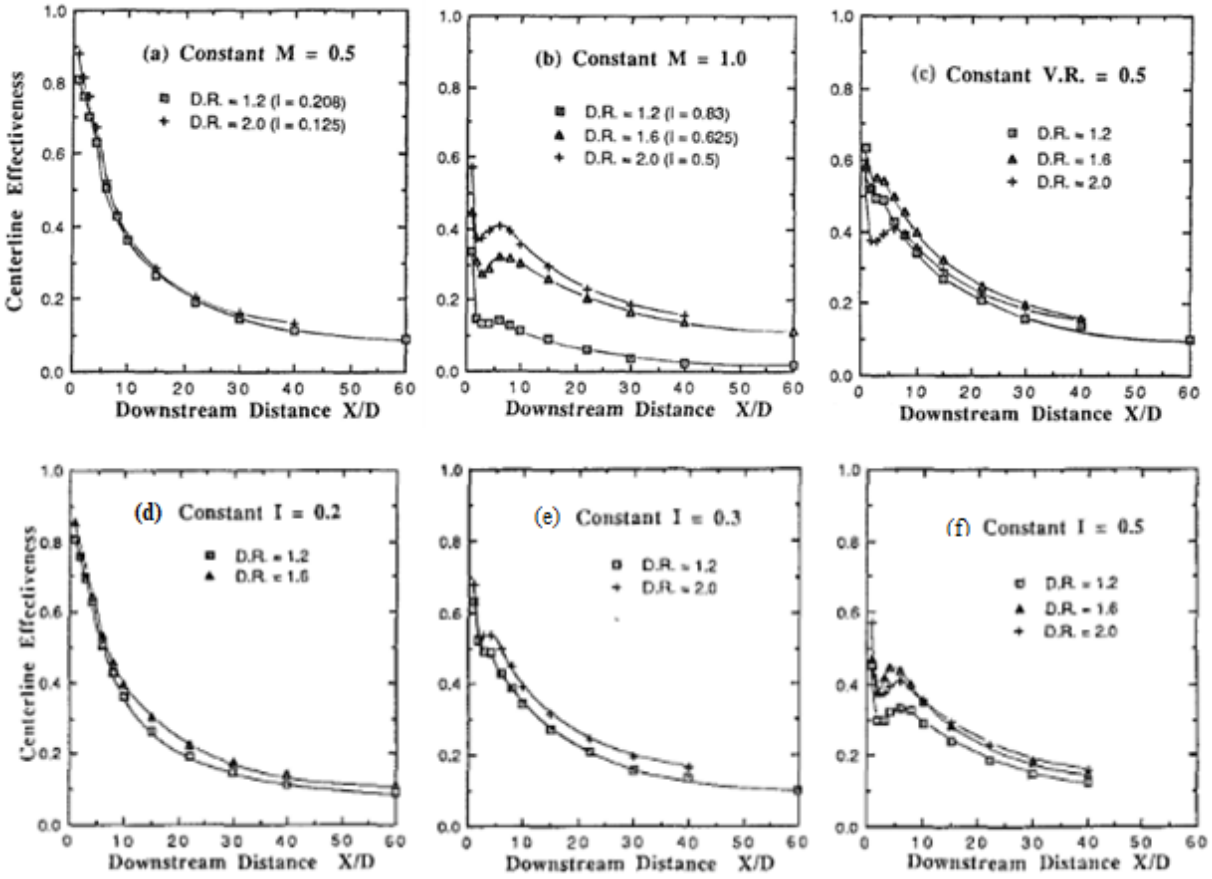

Figure 6: Effect of density ratio at constant scaling parameter values (a) *M* = 0.5, (b) *M* = 1, (c) *VR* = 0.5, (d) *I* = 0.2, (e) *I* = 0.3, and (f) *I* = 0.5 [5].

As shown in Figure 6, neither *M*, *I*, nor *VR* can scale adiabatic effectiveness. A perfectly scaled η would show the centerline effectiveness lines collapsed together with no variation along the downstream distance with the different *DR*s, while each scaling parameter is constant. Sinha et al. also note that scaling of spanwise averaged η show that none of these three parameters can collapse η, for consistent scaling, across the varying density ratios.

Sinha et al. [5] found that the jet dynamics, whether the jet remains attached, separates and reattaches, or has complete detachment, depends on the momentum flux ratio. For jets that remain attached, at low coolant flow rates, η is best scaled with *M*, which is shown to perform well at $M = 0.5$. However, as soon as the jet detaches, whether it reattaches or not, *M* provides an inconsistent scaling of η. For a jet that detaches and reattaches to the surface, *I* was found to have consistent scaling of the general distribution of η. A complete detachment of the jet was found based off momentum flux ratio, at a value of 0.7 for this cooling scheme. Sharp decreases in η were seen as the coolant jet does not travel along the test surface downstream of detachment. Most consistent trends are displayed by *I* which indicates that the effects of changing density ratio are best scaled with *I*. The authors also note that spreading of the jet along the surface increases with an increase in density ratio [5].

While many studies have been performed similar to Sinha et al. [5], characterizing the adiabatic effectiveness scaling ability of *M*, *I*, and *VR* over varying *DR*s, Eberly and Thole [24] do just that but take the study further using time resolved digital particle image velocimetry (TRDPIV) to report flowfield measurements while providing time-averaged and time-resolved data for the film cooling flow. The facility used Eberly and Thole achieved *DR*s near two by cryogenically cooling the coolant flow with a liquid nitrogen heat exchanger. For low and high *DR*s, the authors achieved *DR*s of 1.2 and 1.6, respectively. The authors used an IR camera for

thermal measurements of time-resolved PIV measurements and used a flat plate test model with a cylindrical hole at 35-degree angle injection. Eberly and Thole [24] confirm the result of Sinha et al. [5] that jet detachment best scales with *I*. However, the critical value for separation occurred at $I = 0.6$ for their experimental conditions. Jet momentum was found to create the most jet blockage upstream of the coolant injection. At matched *M*, a lower *DR* had more jet blockage than a high *DR* because of the stronger jet momentum in the low *DR* case. Also, for matched *I* cases, a high *DR* showed more spreading of the jet. More spreading of the jet leads to better cooling effectiveness, and for matched *M*, results showed an increase in effectiveness at high *DR*s compared to the effectiveness at low *DR*s.

Through the use of TRDPIV, Eberly and Thole [24] were able to examine distributions of the coolant as well as the effect of turbulence. The authors found that turbulence affected the coolant distribution in two ways: one, the turbulence caused by the jet interaction with the freestream as it exited the hole and two, the turbulence in the shear layer between the jet and the mainstream. Similar levels of turbulence were seen for both the low and the high *DR* cases. Turbulence levels at the coolant injection scaled best with *I* where high turbulence levels were seen with high *I* cases. However, strength of the shear layer did not scale with *I*. In the shear turbulence case, the peak turbulence occurs when the mass flux of the coolant differs most from the freestream and for this reason, the least turbulence was seen at $M = 1$. The structure of vorticity in the shear layer took the form of Kelvin-Helmholtz instabilities before becoming turbulent in cases where *M* differed from unity. The size and spacing of the shear layer roll-ups remained nearly constant between *I*s. At high *DR*s, the vorticial structures remained closer to the wall than in the case with low *DR*s. The authors also note that counter-rotating vortex pair (CRVP) has been widely studied in film cooling as it greatly affects the cooling performance. Effects of CVRP were seen

with the TRDPIV in the streamwise velocity contours where high velocity fluid is pushed away from the wall at the hole centerline and toward the wall at the hole edge which changes how the coolant is distributed on the surface, affecting where the coolant is distributed.

2.4.3 Reynolds Number Effects

For incompressible flow experiments, experimentalists most commonly match the Reynolds number of the freestream, Re_∞. One issue with using the common scaling parameters *VR*, *M*, or *I* to scale the effects of *DR* is that none of these parameters can simultaneously match the Reynolds number of the coolant, Re_c, while also matching Re_∞. This is one of the main reasons why Re_c is usually disregarded and Re_∞ is matched in many scaling experiments [22]. Greiner et al. [25] researched scaling film cooling performance measurements from experimental ambient lab conditions to that of high temperature engine conditions. The study evaluated the common scaling parameters *VR*, *M*, and *I*, as well as *DR*, but also considered such parameters as Re and Prandtl number (Pr). The theory was that *Re* and *Pr* could be introduced to improve data matching from ambient to engine conditions. The authors used CFD to create a wide variety of hypothetical testing conditions used on a flat plate with a shaped hole geometry.

The findings of Greiner et al. [25] show that there is more to be considered than just the common scaling parameters. The authors note that Pr is usually not mentioned in scaling because it is relatively constant with gases over a large range of temperatures. However, Greiner et al. prove that when Pr is unmatched, η profiles do not match because η was not as sensitive to matching individual gas property ratios as it was to matching Pr. However, Pr is impacted through gas properties such as the fluid's specific heat and density. The impact of matching Pr on the η

profiles indicated the importance of the link between momentum and thermal diffusion between the freestream and the coolant.

Greiner et al. [25] also pursue matching Re_∞ and Re_c, finding that both scale well but have different advantages under certain conditions. In a low temperature experiment, it is impossible to simultaneously match *M*, *DR*, Re_∞ and Re_c for a fixed hole diameter and downstream distance from the hole injection location. This is because matching *DR* and the dynamic viscosity ratios, $\frac{\mu_c}{\mu_\infty}$, are mutually exclusive due to their variations with the coolant and freestream temperatures. Although, using CFD simulations to match *M* and *DR*, the authors found that matching Re_∞ best scaled spanwise averaged η but Re_c best scaled centerline effectiveness. The authors note that there are trade-offs to matching Re_∞ or Re_c individually, where Re_∞ is more important to match in most lab experiments and Re_c provides a slightly better scaling for η overall. The authors then averaged the two results and the outcome produced the best film cooling effectiveness scaling results.

The results of Greiner et al. [25], in regards to *Re*, help describe the thought process behind another nondimensional parameter introduced by Rutledge and Polanka [22] called the Reynolds number ratio, *ReR*, which considers viscous effects of the freestream and the coolant by taking *M* and multiplying it by the ratio of dynamic viscosities. *ReR* is also a proxy for matching Re_c when Re_∞ is matched. The Reynolds number ratio is defined as:

$$ReR = \frac{\rho_c \mu_\infty u_c}{\rho_\infty \mu_c u_\infty} \tag{22}$$

Rutledge and Polanka describe that the *ReR* between ambient and engine conditions varies by about 2.5, while holding *M* constant, having a significant impact on the ratio of *h*, the convective heat transfer coefficient. This impact was due to the way viscosity influences the Prandtl number,

Pr. The authors [22] found that increasing ReR affected η primarily by widening the coolant jet. This would be expected since Re_c's influence is on the hydrodynamic effect of the coolant and not the thermal behavior.

2.4.4 Other Fluid Property Effects

One may be inclined to believe that scaling adiabatic effectiveness from a low temperature test to high temperature engine conditions would be a simple task since η is a nondimensional form of the adiabatic wall temperature. However, η measured at ambient conditions around 300 K is not equivalent to η measured at engine conditions around 2000 K. Although η is only a function of temperatures, the difference in η is because many fluid properties change with temperature, resulting in difficulty scaling from ambient to engine conditions. One way the scaling of η can be predicted is by using a variety of gases to characterize how various gas properties influence the scaling results. A variety of different gases, with a wide range of fluid properties, that were injected as the coolant in the low temperature tests of this study are shown in Table 2 to compare to engine conditions. Engine conditions are represented in the table by air at 2000 K. Table 2 was constructed using standard gas tables [13]. Due to the variation of gas properties with temperature, scaling parameters need to be properly characterized to determine the most accurate scaling technique of adiabatic effectiveness.

Table 2: Properties of Various Gases at Testing and Engine Conditions [26].

Gas	Density ρ (kg/m^3)	Specific heat c_p (kJ/kg-K)	Dynamic Viscosity μ (10^6 Pa-s)	Thermal Conductivity k (10^{-3} W/m-K)
Engine Freestream (Air, 2000 K, 30 bar)	5.22	1.34	68.9	137
Engine Coolant (Air, 1000 K, 30 bar)	10.45	1.14	42.44	66.7
Air (300 K)	1.16	1.01	18.46	26.3
Air (150 K)	3.24	1.01	10.34	13.8
CO_2 (300 K)	1.77	0.85	14.9	16.55
N_2 (300 K)	1.12	1.04	17.82	25.9
Ar (300 K)	1.66	0.52	22.3	17.2
He (300 K)	0.16	5.19	19.9	152

While a significant amount of research surrounds the influence of density in the coolant-to-freestream density ratio and whether blowing ratio or momentum flux ratio is the best nondimensional fluid transport parameter to account for the density effects, there is uncertainty in determining the most ideal method to scale film cooling experiments from typical low speed, low temperature wind tunnel tests to high speed, high temperature engine conditions. As shown by Sinha et al. [5], neither *VR*, *M*, nor *I* perfectly scale adiabatic effectiveness so there are another fluid properties that needed to be considered. Rutledge and Polanka [22] emphasize the importance of accounting for the thermal energy transport as the coolant is injected into the freestream. In its relation to scaling, specific heat, c_p, describes a coolant's ability to absorb heat for a given change in temperature. This leads to the requirement to account for the specific heats of the coolant and the freestream. Therefore, Rutledge and Polanka [22] multiplied *M* by the ratio of specific heats, $\frac{c_{p,c}}{c_{p,\infty}}$, to develop the nontraditional parameter called heat capacity ratio, *HCR*, but later renamed to what it is now known as, *ACR*, by Rutledge et al. [23]. The current study will refer to the ratio as

ACR for the rest of the discussion. In a scaling experiment where *M* is matched with $DR = 1$ using air as the freestream and coolant, the *ACR* value would be 20% greater than the *ACR* at engine conditions.

Rutledge and Polanka [22] evaluated several unconventional scaling parameters, of particular interest is *ACR*, using computational fluid dynamics (CFD) on a simulated turbine blade leading edge. The study used a cylindrical leading edge model with a flat afterbody, single cylindrical coolant hole located 21.5 degrees from the leading edge and angled at 20 degrees to the surface resulting in a 90-degree compound angle coolant injection to the freestream. CFD allowed this study to alter individual gas properties leading to a variety of fictitious gases to evaluate their effect on the overall behavior of film cooling and the importance of matching various coolant flow rate scaling parameters.

Considering the gas properties μ, k, and c_p, Rutledge and Polanka [22] found many interesting results varying these properties. The authors found that increasing dynamic viscosity does little to the magnitude of η but it does change the displacement of the coolant. A lower thermal conductivity hinders a fluids absorption of heat, so a higher thermal gradient is required to conduct the same amount of heat. A lower heat absorption causes the coolant to stay colder as it travels downstream which results in a slightly higher η. A lower specific heat coolant reduces the cooling capacity of the coolant, thus increasing the temperature faster. The results reveal a decreased η since the coolant does not remain as cold as it travels downstream of the injection hole. Combining the effects of specific heat and thermal conductivity, the effects tend to offset each other which leaves density to be the main factor to the adiabatic effectiveness variation in scaling experiments. However, when considering *ACR* at experimental conditions compared to engine conditions, while all other parameters are matched, the results show an under-prediction of adiabatic effectiveness.

This validates the need to account for the difference in specific heat between the coolant and the freestream [22].

After considering the various gas properties, the results of the study by Rutledge and Polanka [22] summarize which scaling parameter can best scale adiabatic effectiveness across a wide variety of conditions implemented through the use of fictitious gases provided by CFD analysis. The authors found that *M* provided the best match of the peak value of adiabatic effectiveness but lacked the ability to match the trajectory of the coolant jet. *I* was able to best predict the trajectory of the coolant flow by being able to best match the location of peak adiabatic effectiveness. *ACR* had a large effect on adiabatic effectiveness since the ratio directly relates the resistance of the coolant to temperature changes. A lower *ACR* results in a coolant increasing more readily with temperature, which decreases η. *ACR* was also able to match peak location of η by a difference of 0.04. Therefore, although *M* best predicted the magnitude of peak η and *I* best predicted the location of peak η, *ACR* proved to be a good compromise between the two. A representation of their summarized findings is shown in Figure 7.

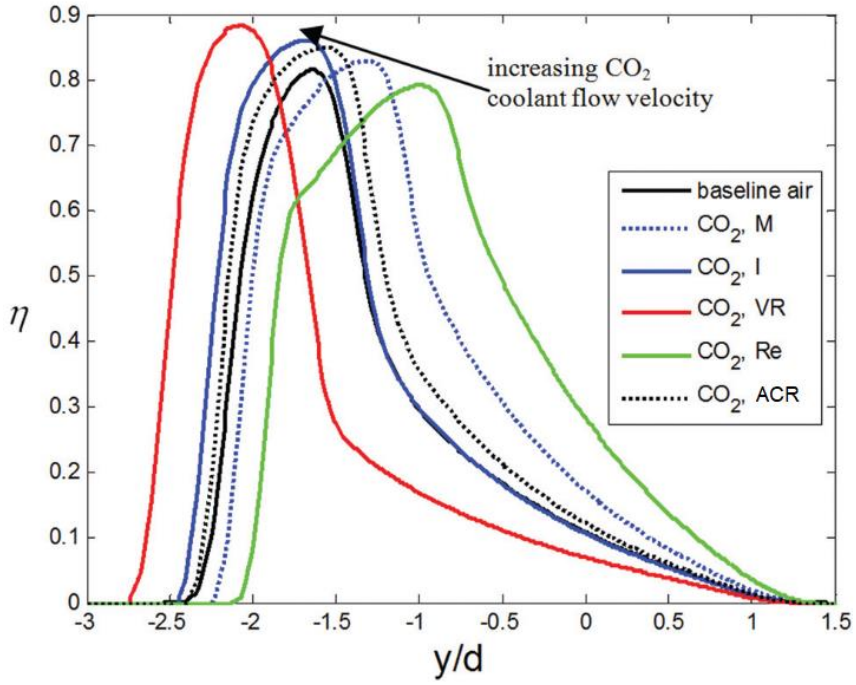

Figure 7: Adiabatic effectiveness at x/d = 3 for air and CO_2; coolant flow rates selected to match *ACR*, *I*, *M*, *ReR*, and *VR* [22].

2.4.5 Thermal Methods Compared to Mass Transfer Methods

Johnson et al. [27] conducted an experimental study of density ratio effects on film cooling injection from discrete holes using the PSP measurement technique. The study achieved density ratio differences using two different foreign gases, nitrogen (N_2) and carbon dioxide (CO_2), to achieve *DRs* of 0.97 and 1.53 respectively. The study investigated adiabatic effectiveness between the differing densities using the common scaling parameters of *M*, *I*, and *VR*. The test conditions of the study were a turbulence intensity of 1.5%, Re = 22,000, cylindrical cooling holes with 30° injection angles, and the PSP used was ISSI's UniFIB. The authors qualitatively used contours and quantitatively used centerline adiabatic effectiveness and laterally averaged adiabatic effectiveness to interpret their results. Qualitatively, the authors noted that the more dense coolant stream, CO_2,

provided a higher cooling effectiveness and a much wider coolant coverage than the less dense coolant stream with N_2 at matched *M*. However, quantitively, Johnson et al. [27] found that the film cooling effectiveness over the test surface was found to be independent of the *DR* and thus, properly scaled when *M* or *I* is matched, at low values of 0.40 and 0.17 respectively, but as *M* or *I* increases, the density ratio was not scaled. The opposite trend is seen with *VR* and that scaling with *VR* becomes useful across different *DRs* as *VR* is increased. The results of Johnson et al. can be seen in Figure 8.

The authors went on to compare the results to thermal experiments by Baldauf et al. [28], by whom they modelled their test conditions after to achieve similar boundary layer flow conditions. They also compared their data to several other thermal studies; the results are shown in Figure 9. Noting that the statistical bounds of their uncertainty allowed results of cooling effectiveness to agree within ±0.09, Johnson et al. state that the film cooling effectiveness using PSP in their study agrees well with the IR thermography measurements of Baldauf et al. However, the authors state that the peak cooling effectiveness from their PSP study resulted in lower peak effectiveness values and contours that were narrower in the spanwise direction. They attribute the higher prediction of η using IR measurements to the effects of heat conduction that are captured using thermal measurement techniques.

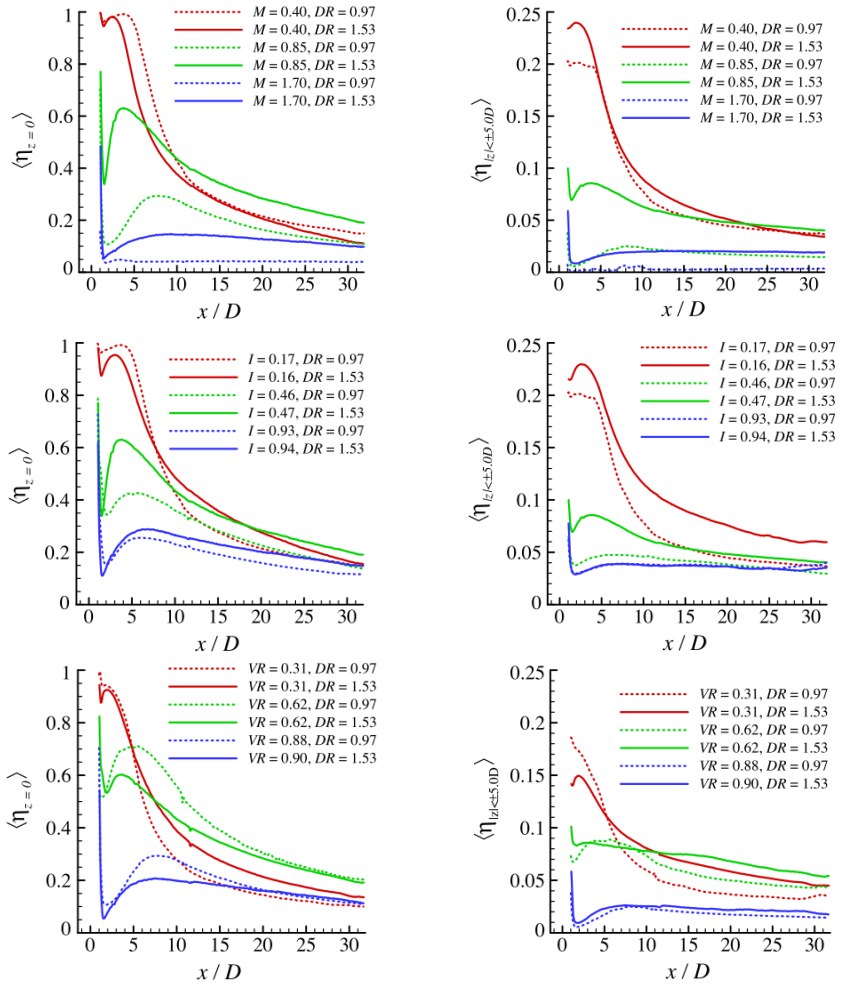

Figure 8: Adiabatic effectiveness using PSP at centerline (left column) and laterally averaged (right column) with matched *M*, *I*, and *VR* [27].

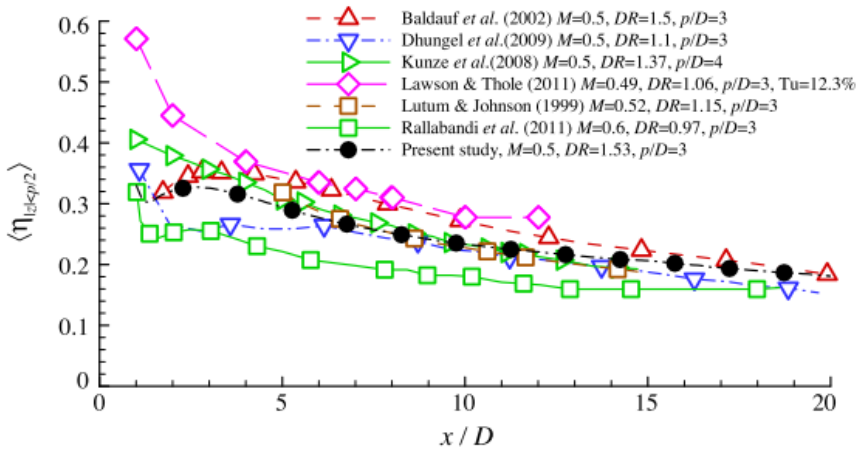

(a). The measurement results at blowing ratio of M≈0.50 and density ratio of DR≈1.5

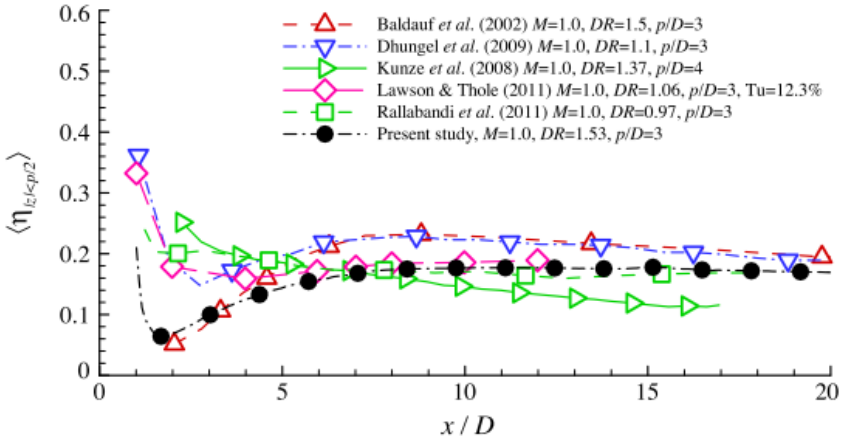

(b). The measurement results at blowing ratio of M≈1.00 and density ratio of DR≈1.5

Figure 9: Comparison of laterally averaged η of Johnson et al. [27] with other published studies at the same or comparable conditions.

Similar to the objective of the current study, Wiese et al. [3] explored the validity of using the mass transfer analogy, through using a PSP measurement technique, as a surrogate to an IR thermal measurement technique. Wiese experimented using the IR thermal method and then painted the model with a binary PSP to test the mass transfer method, a first of its kind to compare the two methods on the same model, in the same facility. The authors [3] used a semi-cylinder

leading edge model with a flat afterbody. The single coolant hole was offset from the stagnation line at 21.5° while the angle between the coolant hole axis and vertical axis was 20°, creating a 90° compound cooling hole. The authors used a variety of foreign gases to achieve a wide variety of different gas properties to explore the effects of matching several scaling parameters. The gases used with both measurement techniques were argon (Ar), CO_2, and N_2. Air was also used with the IR measurement technique. Overall, the authors found that the PSP measurement technique is not a replacement for IR thermography and that when compared to IR, PSP indicates an overprediction of film cooling performance as shown in Figure 10. However, it was found that the PSP technique does predict trends in adiabatic effectiveness well.

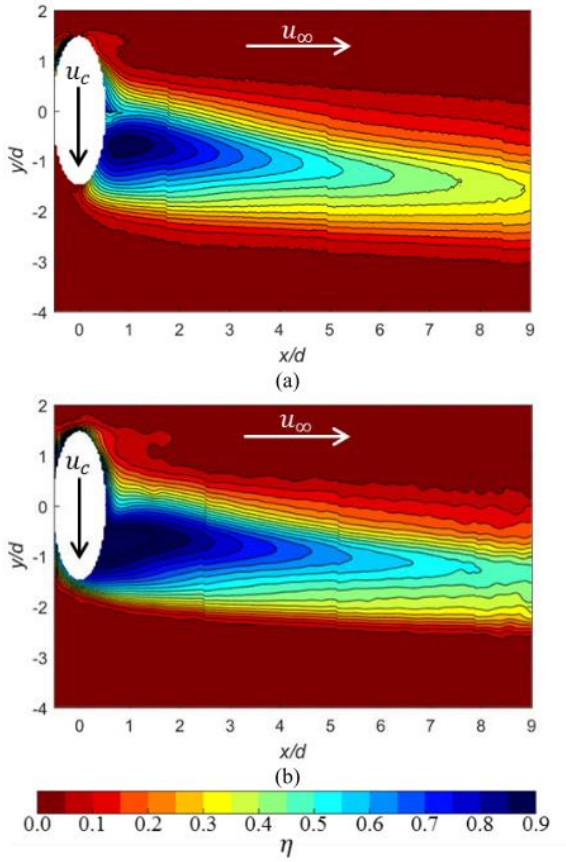

Figure 10: Adiabatic effectiveness contour plots for N_2 coolant at I = 0.5 using IR (a) and PSP (b) measurement techniques [3].

Wiese et al. [3] attribute the greater effectiveness with the mass transfer method to PSP's insensitivity to the thermal diffusion process whereas the IR thermal measurement method is sensitive to that process. The PSP measurement technique is insensitive to the thermal diffusion process because it only tracks the location of the coolant on the surface and doesn't account for how the coolant molecules interact with the freestream through conduction heat transfer between the two fluids. The coolant and the freestream can transfer thermal energy by transferring mass through mixing and by conduction between the fluids. This indicates that the freestream fluid does not need to reach the surface for the surface to experience thermal effects. The ability of a coolant to maintain its temperature does not influence how the coolant diffuses, beyond the changes in the temperature dependent mass transfer properties, since the specific heat of a fluid does not have an influence on mass transfer. Thus, the locations where the IR contours show a subdued effectiveness compared to the effectiveness from the PSP contours indicate that the coolant displaced on the surface had experienced heat transfer from the freestream [3].

Although effectiveness contours show individual cooling performance well, Wiese et al. [3] related multiple cases using scaling parameters such as *VR*, *M*, *I* and *ACR*, and adiabatic effectiveness plots such as that seen in Figure 11. Using spanwise adiabatic effectiveness plots, the authors found that the peak location of effectiveness is best scaled by *I*, relating to Rutledge and Polanka [22]. Another feature to note comparing the spanwise adiabatic effectiveness plots is the slope of the curves. It can be seen in Figure 11, and the other spanwise adiabatic effectiveness contours, that $\frac{\partial \eta}{\partial y}$ of the IR method is less than that of the PSP measurement technique at lower *y/d* values. The authors attribute this to the lateral thermal diffusion within the solid and the fluid in this high thermal gradient region, a region that would go undetected by the PSP measurement technique. The effects of the lateral conduction can be accounted for with a spanwise averaged

adiabatic effectiveness plot [3]. The PSP method again shows a higher effectiveness than the IR measurement technique which indicates that the elevated effectiveness is not solely a result of the lateral conduction decreasing the peak effectiveness. The authors attribute the difference to the IR method being sensitive to the specific heat of the coolant gas and that PSP is not sensitive to the additional thermal diffusive mechanism that IR captures.

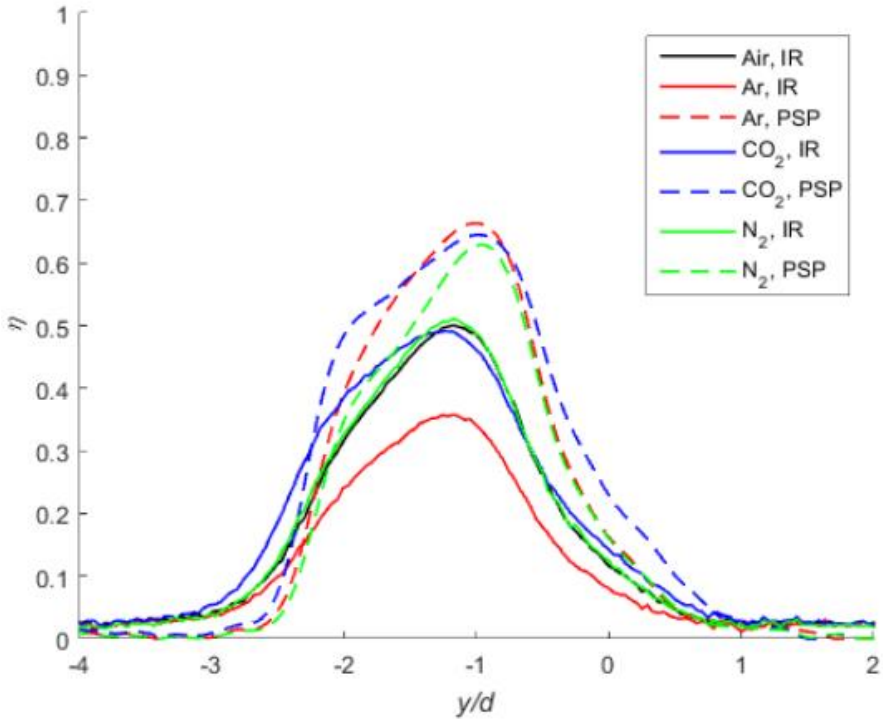

Figure 11: Spanwise adiabatic effectiveness at I = 0.5 and x/d = 5.0 [3].

This leads to then comparing matched *ACR*, which the authors found to not have an influence on how the coolant jet performs with respect to adiabatic effectiveness with the PSP method since mass transfer is unaffected by a fluid's specific heat. Shown in Figure 12, the Ar profile was vastly different from the other three gases, for both measurement techniques, and this was attributed to matching ACR leads to a high I values, which would indicate a separated jet. The leading edge model with a 90° compound angle injection used by Wiese et al. [3] was conducted

in a momentum dominated flow environment that heightened the effects of jet separation and turbulent mixing. Wiese [17] states that in order to alleviate some of these effects and to better characterize the merits of *ACR*, experiments should be run on a flat plate with zero compound angle injection.

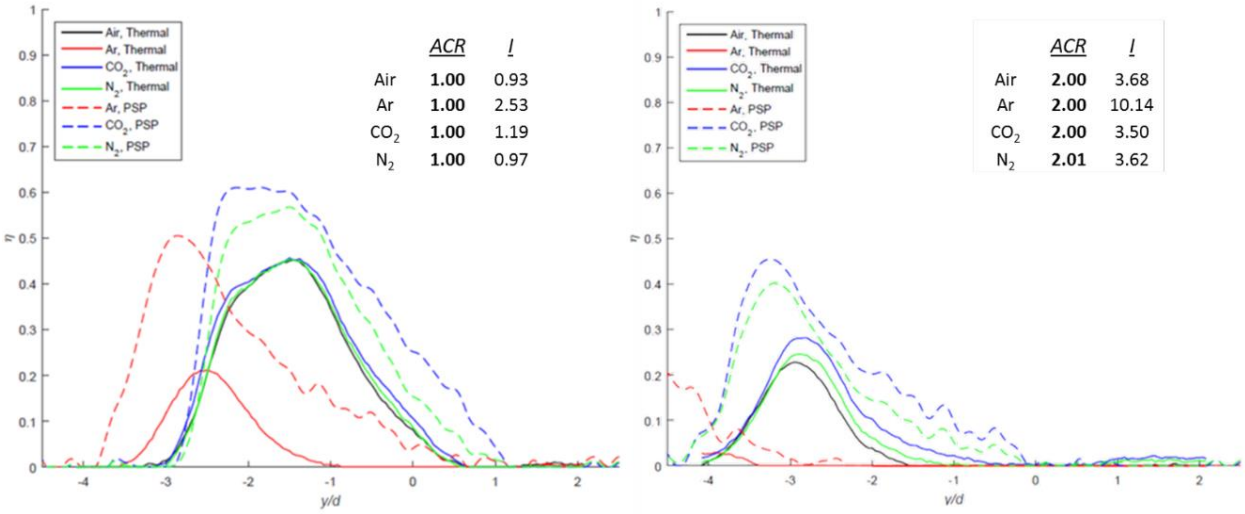

Figure 12: Adiabatic effectiveness distributions at *x/d* = 5.0, at two matched *ACR* values using IR and PSP measurement techniques [3].

2.4.6 *ACR*'s Ability to Scale *η* with Thermal Methods

The findings and recommendations by Wiese [17] and Wiese et al. [3] led to the study that was performed by Fischer [2] and Fischer et al. [29]. Based on the recommendations of Wiese [17], Fischer [2] investigated the efficacy of scaling with *ACR* in an environment that was not momentum dominated. The test was conducted on a flat plate with a 7-7-7 hole geometry, with dimensions to replicate the original boundary layer conditions and flowfield conducted in the original 7-7-7 hole study by Schroeder and Thole [20]. The test was conducted in the same wind tunnel with the same leading edge geometry as Wiese [17] and Wiese et al. [3] but the test surface was applied to an extended afterbody to achieve the flat plate test surface. More detail on the test

rig, flat plate, experimental setup, and conditions are given in Section 3.1, 3.2, and 3.3 as they remained the same for the current study. The thermal results shown in this study (Chapter 4) are the same results as Fischer et al. [29], which are the results of a repeated experiment to that of Fischer [2]. The same overall conclusions were reached for the thermal experiment in Fischer [2] that were reached in the repeated study in Fischer et al. [29], i.e. the current study. To have an identical test comparison between two measurement techniques, the results that are given in this Section are from the repeated experiment. A thorough examination of all the results, including all scaling parameters and data points, from the repeated Fischer et al. [29] study as compared to the current study's PSP experiment are given in Chapter 4.

In summary, the experimental method used by Fischer et al. [29] was an IR thermal measurement technique. The test conditions were Re_D = 5000 and a turbulence intensity of 0.67%. Four foreign gases were used as coolants to achieve a wide range of property variations in order to test the efficacy of the scaling parameters presented in the current study: *M*, *I*, *ACR*, *VR*, and *ReR*. As shown in Figure 13, never before seen in literature, *ACR* proved the ability to near perfectly scale adiabatic effectiveness over a variety of different gases with drastically different gas properties. The *DR* values varied from 0.15 to 1.65 and the inclusion of the ratio of specific heats between the coolant and the freestream allowed *ACR* to collapse the adiabatic effectiveness profiles.

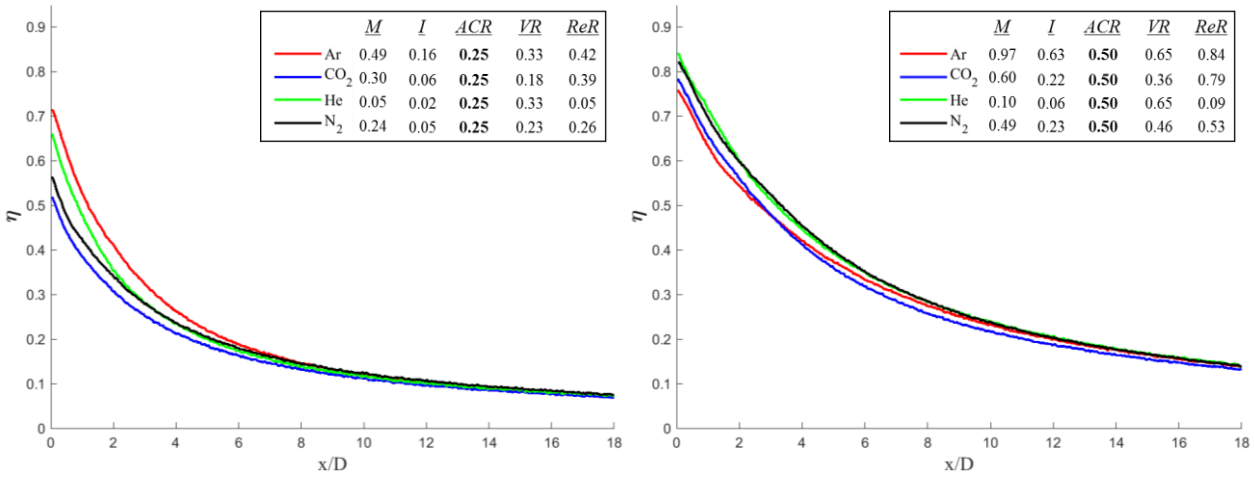

Figure 13: Centerline η_T at matched *ACR* = 0.25 (left) and 0.5 (right) [29].

Fischer et al. [29] also evaluated scaling parameters *M*, *I*, *VR*, and *ReR*. Fischer found that *M* did not effectively collapse the centerline adiabatic effectiveness profiles. *M* was found to scale well for CO_2, N_2, and also air, but when Ar and He were added to the dataset, having lower and higher specific heats, respectively, the inability of *M* to account for specific heat proves to be the breakdown of the scaling parameter. *I* was also found to be an insufficient scaling parameter, although it was found to be able to predict the onset of jet separation, which was a value of $I > 0.5$ for the test configuration and conditions. Fischer et al. [29] also found if there was separation in the centerline η_T profiles in a matched *M* or *I* case, increased *ACR* values resulted in increased adiabatic effectiveness. However, after separation on the centerline η_T profile for matched *ACR*, the trend was now of decreasing *I* values resulting in increased adiabatic effectiveness. *VR* was shown to reveal similar results to matched *M* and does not scale well across all the foreign gases, and deviations between the gases were greater as the flow rate was increased. *ReR* also showed similar results to matched *M*. Although, at high *ReR*, an interesting spreading phenomenon of CO_2 was shown that the gas spread further laterally than the other gases. This phenomenon was also

experienced by Wiese [17], and the authors were unable to attribute the spreading to a specific cause. The results described in this paragraph can be seen as the IR thermal results in Chapter 4.

The most powerful tool of *ACR*, as shown by Fischer et al. [29], can be visualized by Figure 14 which displays the area-averaged adiabatic effectiveness, $\bar{\bar{\eta}}$, vs. *ACR* for all data points collected. Shown by the dashed arrows is the corresponding *I* value where separation occurred using that particular foreign gas as a coolant. The value for He was estimated due to the flow rate being higher than the capabilities at the facility used for the experiment. The difference in the magnitudes of $\bar{\bar{\eta}}$ can be attributed to jet separation, as indicated by *I*, being independent of specific heat. Figure 14 shows that no matter the density or specific heat of the coolant gas, adiabatic effectiveness is scaled at low values of *ACR* as all the gases follow the same curve and then individually deviate from the general trend as the flow rate is increased. The expected deviation from the curve correlates to the onset of jet separation at about $I = 0.6$. Thus, the authors conclude that *ACR* is able to near perfectly scale adiabatic effectiveness for cases where the jet remains fully attached, at values less than $I = 0.5$ for the conditions of the study, and therefore the inclusion of specific heat in scaling research needs to be considered [29].

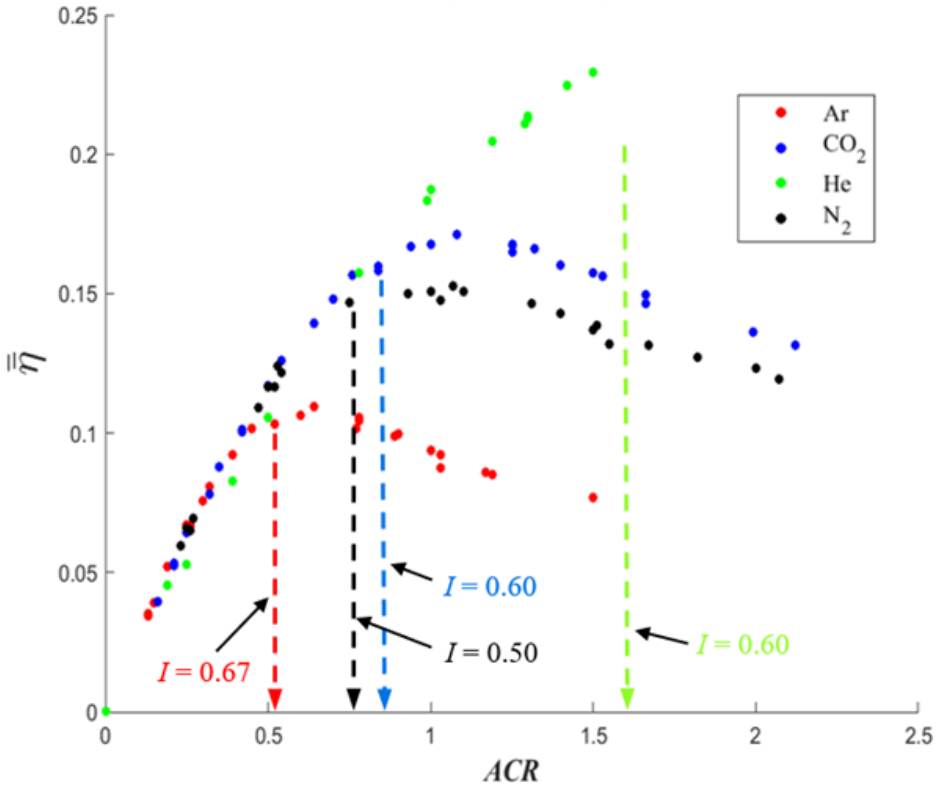

Figure 14: $\bar{\bar{\eta}}$ vs. *ACR* distributions for all test cases [29].

3. Methodology

Pressure sensitive paints are becoming commonly used to implement a boundary condition analogous to an adiabatic wall with the mass transfer analogy for film cooling effectiveness studies. While infrared thermography continues to be a widely used method for the thermal measurement technique, it requires a conduction correction, along with all thermal techniques, for adiabatic effectiveness results. To further investigate the merits of the flow rate scaling parameters used by Wiese et al. [3], this study aims to evaluate and compare adiabatic effectiveness results between two measurement techniques, a PSP method using the mass transfer analogy and an IR thermal method, on a flat plate geometry with a standard expanded exit cooling hole, at a zero degree compound angle flow injection, and determine the efficacy of how several flow rate parameters scale the results. This chapter will describe the tools and methods used in this study to most accurately quantify the objectives of the study. Included in this chapter are descriptions of the facility (Section 3.1), the model (Section 3.2), the IR experimental method (Section 3.3), the PSP experimental method (Section 3.4), and the uncertainty analysis (Section 3.5).

3.1 Facility

The facility used in this study was the Air Force Research Laboratory (AFRL) Heat Transfer and Aerodynamics Lab, Test Cell 21; the same facility used by both Fischer [2] and Wiese [17]. A schematic of the wind tunnel flow path within the facility is shown in Figure 15. The facility consisted of an open loop wind tunnel, 0.368 m by 0.406 m test section, powered by a 50 hp blower. After the air entered the intake, located outside the facility, the air passed through the blower. Immediately downstream of the blower, the freestream flow velocity was controlled by a flow control valve. Next, since the temperature of the intake air depended on the weather

conditions outside, the temperature of the freestream was thermally conditioned using a 70 kW heater or chilled by a cold water chiller. For this study, the freestream temperature was controlled using a temperature control from the 70 kW heater and was set to 327 K. The freestream temperature was validated with a J-type thermocouple placed in the freestream of the test section. The deviation of the freestream temperature was limited to ±0.5 K during all tests run, on all days. Turbulence characteristics of the freestream were first characterized by Rutledge [30] with the current test configuration. However, a new blower was installed, and Rutledge's findings were verified. The tunnel exhibits a turbulence intensity of 0.67% in the current test configuration.

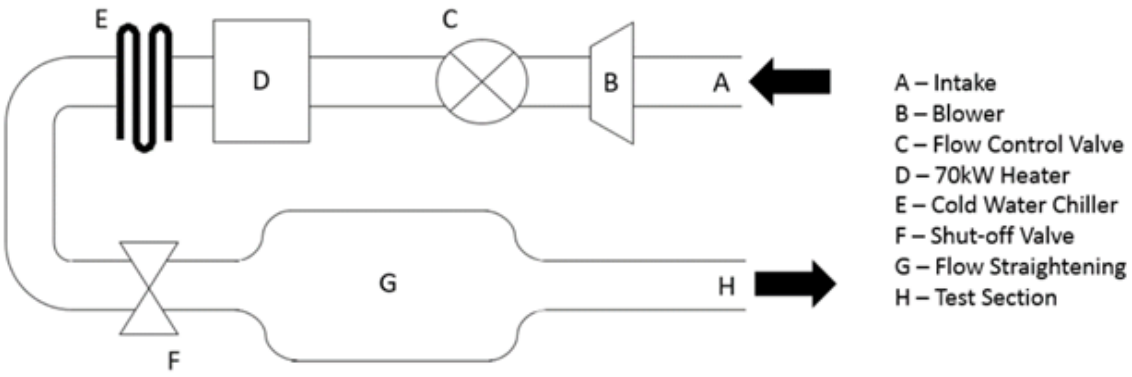

Figure 15: Wind tunnel schematic. Adapted from [2].

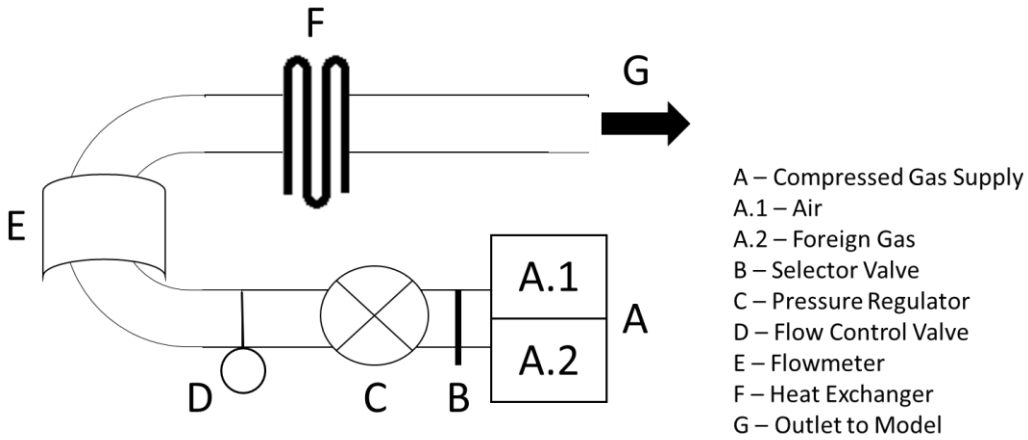

Figure 16: Coolant flow path schematic.

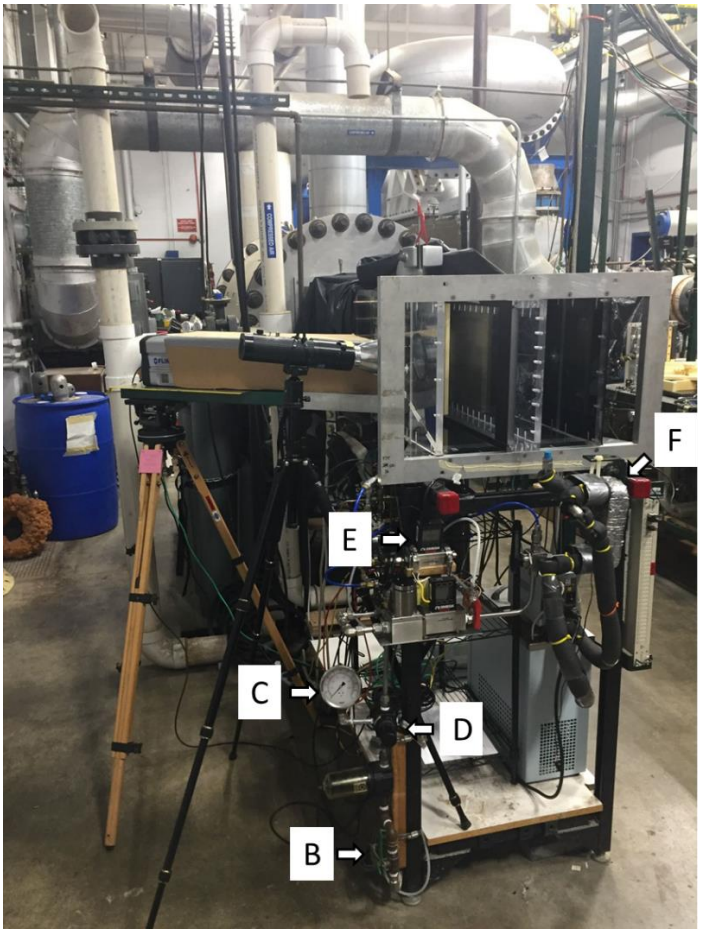

Figure 17: Wind tunnel used in this study.

The coolant flow path can be visualized by the schematic in Figure 16 and an image of the actual tunnel in Figure 17. The coolant gas supply, Figure 16 (A), was routed from two different sources for using either air, Figure 16 (A.1), or one of the foreign gases, Figure 16 (A.2). When air was used as the cooling gas, the compressed gas supply was the facility shop air line that was maintained at a pressure between 100 and 125 psia. When a foreign gas was used, the coolant was routed from a rack of compressed gas cylinders. The same routing configuration was used for each foreign gas and therefore, the line had to be switched between cylinders when changing the gas for testing. The regulated pressure was maintained at 100 psi for all the foreign gas cylinders used. Immediately before the pressure regulator, the coolant supply from Figure 16 (A) to (C) could be

switched between the shop air line and the foreign gas line by opening or closing their respective lever, controlling the selector valve, Figure 16 (B) and Figure 17 (B). This controlled the coolant that would be supplied to the pressure regulator, Figure 16 (C) and Figure 17 (C), through the flow path and out to the model, Figure 16 (G). Once the coolant passed through the pressure regulator, the mass flow was measured and controlled by a digital Omega FMA-1609A laminar flow element flowmeter, Figure 16 (E) and Figure 17 (E). The flowmeter had the ability to monitor a mass flow up to 50 standard liters per minute (SLPM) and was loaded with the various coolant gas' fluid properties. The flowmeter was rated to an uncertainty of $\varepsilon_{m_{dot}}$ = (0.8% reading +0.1 SLPM) up to 50 SLPM. The mass flow of the coolant was controlled by a fine-tuning manual valve, Figure 16 (D) and Figure 17 (D), that was monitored and adjusted to maintain the specific mass flow required for each data point collected during testing. Next, the coolant passed through a Bell and Gossett BP 400-010 heat exchanger, Figure 16 (F) and Figure 17 (F), which used fluid from a chiller that maintained a mixture of ethylene glycol and water at 285 K, supplied from a Cole-Parmer Polystat bath, that allowed for coolant temperature control within ±0.5 K between temperatures of 295 K to 305 K.

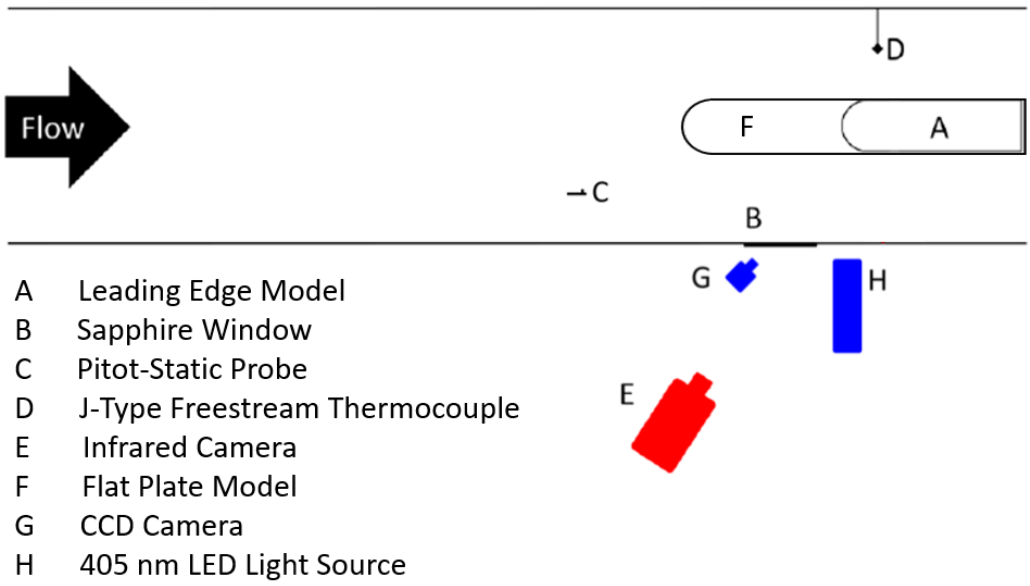

Figure 18: Test section schematic, aerial view, IR (red) and PSP (blue). Adapted from [17].

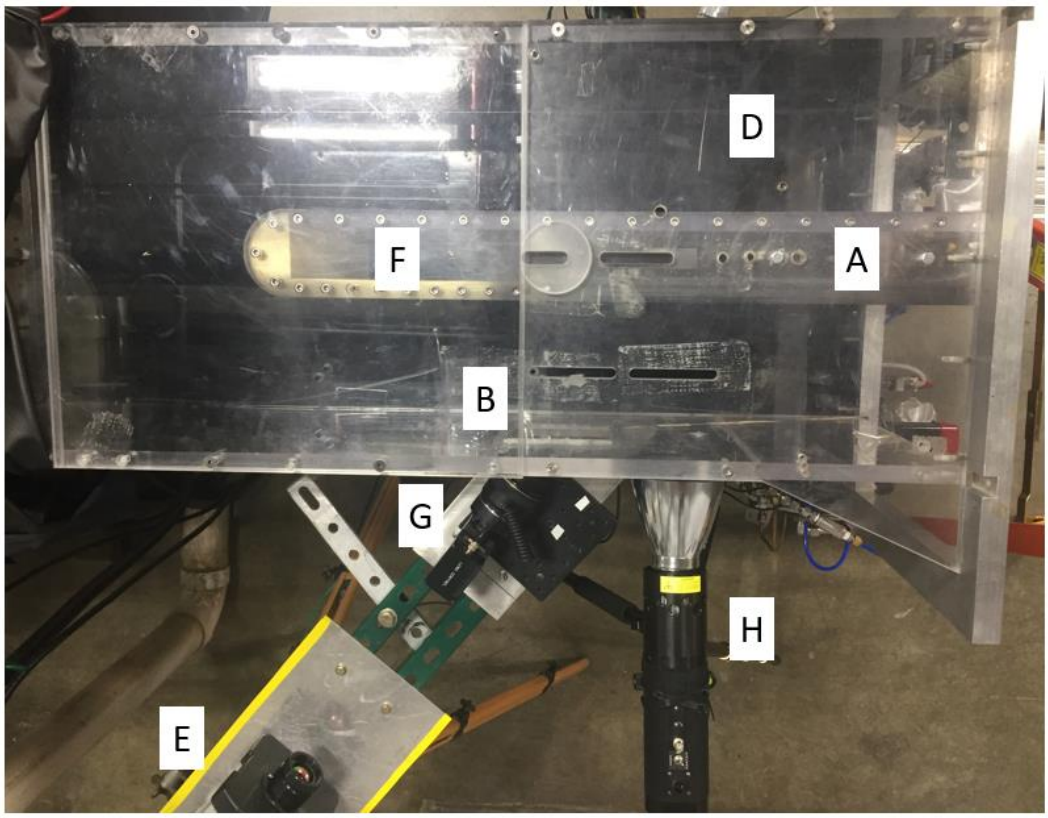

Figure 19: Test section, labelling consistent with Figure 18, no pitot probe pictured.

To aid in the following discussion, a top down view schematic is provided in Figure 18 and an actual top down image of the test section is pictured in Figure 19; both images have consistent labelling. To achieve a desired Re, the flow velocity was set with a tunnel flow control valve and was measured using a pitot-static probe shown in Figure 18 (C). The pitot probe was placed upstream of the flat plate model, out of view from the sapphire viewing window, and located above the region of interest for testing where it would not disturb either the freestream or coolant flow near the test surface. An Omega PCL-1B manometer measured the pitot pressure differential. Also, the freestream density was calculated from the flow temperature and ambient pressure. The freestream flow temperature was measured by the J-Type thermocouple inserted into the freestream shown in Figure 18 (D) and Figure 19 (D). The ambient pressure was determined by the same Omega flowmeter used to control and monitor the coolant mass flow. To determine the ambient pressure, the coolant routing line was first opened on both sides of the flowmeter to expose it to the ambient pressure. The pressure was then recorded and set to that fixed value for the duration of that test. The coolant routing lines were then closed for the flowmeter to monitor only the coolant flow. The specific heats, c_p, viscosities, μ, and thermal conductivities, k, of both the freestream and the coolant were determined by linear interpolation using measured temperatures of the freestream and coolant, T_∞ and T_c, respectively, to that of published data sets [31], [32], and [33].

A series of earlier work conducted in this facility focused on the test section that housed a scaled up turbine airfoil leading edge model, such as the work done by Wiese [17]. Using a leading edge model meant that the camera position, mounting holes, data acquisition code, and data reduction code were set up for that specific type of model. Specifically, a model consisting of a 0.089 m diameter cylindrical leading edge with a flat afterbody, shown in the test section

schematic, Figure 18 (A). However, Fischer [2] was the first to use the facility for testing a scaled up flat plate model geometry. Fischer modified the test rig to simply extend the flat afterbody forward, depicted in a schematic in Figure 18 (F). By extending the afterbody to view the flat plate region of interest for cooling effectiveness, this allowed the IR camera to maintain the same mounting points for viewing both a leading edge geometry or flat plate geometry, interchangeably. Also, all the mounting points were maintained for the test rig placement in the wind tunnel.

Highlighted in blue in Figure 18 was where the CCD camera and LED source were located for the PSP method testing. The CCD camera was mounted to view the same region of interest that IR camera, highlighted in red in Figure 18, captured through the window. A single LED source was chosen for PSP testing. A single source was chosen because with a diffuser placed on the end of the light, the light intensity was able to be evenly distributed onto the viewing region of interest. The LED was also placed perpendicular to the region of interest so that in conjunction with the angle of the camera, minimal light would reflect off the testing surface directly into the camera.

3.2 Model

A CAD model of the test rig designed by Fischer [2] for a flat plate model design is shown in Figure 20. For a detailed discussion on the design process, reference Fischer [2]. To summarize, the model was of a Plexiglas frame (green) and two Last-a-Foam sections (red and blue). The upstream and leading edge Last-a-Foam sections (red) were constructed out of a high density foam, part number FR-7119, to provide both structural integrity and a smooth transition to the test section insert (blue) constructed out of a low density foam, part number FR-7106. The low density foam was chosen for its material properties, specifically the low thermal conductivity: ρ = 96 kg/m^3, c_p = 1260 J/kg-K, and k = 0.03 W/m-K. The low thermal conductivity reduced the conduction,

and hence, uncertainty, through the test plate. This, in turn, required a smaller conduction correction when calculating the adiabatic effectiveness. By design, the flat plate insert could easily be removed from the rig, even while the model was installed in the tunnel. This allowed for easy transition between experimental methods, testing, and calibrations.

The dimensions of the cooling holes and their placement were chosen based on the nondimensional distances from the analysis of the 7-7-7 hole by Schroeder and Thole [20]. Dimensions are shown in Figure 20. The nondimensional distances from Schroeder and Thole's 7-7-7 hole, shown in Figure 5, were multiplied by the metering diameter of the 7-7-7 hole, D = 5.81 mm for this study. The x/D distance from the leading edge to the entrance of the cooling hole was also scaled from [20] to x/D = 69 for this study. Thus, Re_x was matched at the hole exit between [20] and this flat plate model to provide a better comparison between the data collected from the two groups. The second x/D dimension, x/D = 20, was the maximum viewing distance through the sapphire window from the IR or CCD camera for the test setup in this study.

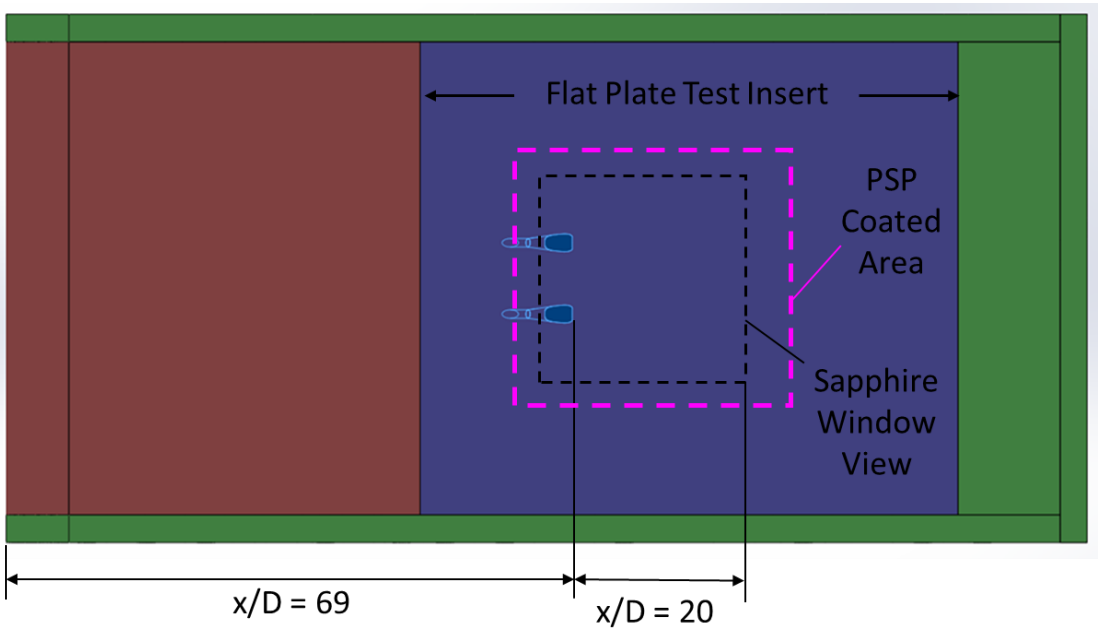

Figure 20: CAD model of flat plate test rig. Adapted from [2].

To apply the IR calibration used by Baldauf et al. [12], overviewed in Section 2.2.1, and the implementation discussed in Section 3.3.2, Fischer [2] designed a flat plate test section consisting of two 7-7-7 cooling holes. The test surface containing the two cooling holes can be seen in Figure 21. The purpose of two coolant holes was so one hole could be used for IR calibration with thermocouples placed downstream of the coolant hole on the surface, indicated by dashed red circles in Figure 21. The non-instrumental hole was used as the test hole so that the embedded thermocouples and attached wires would not interfere with the coolant as it was injected onto and travelled along the test surface. The holes were spaced at y/D = 6.0 so that the coolant plume of one hole would not affect the coolant plume of the other during testing. However, only one hole was used at a time during this study. Each cooling hole had its own supply plenum, identical in construction, so that each hole could be individually tested without any coolant flowing out of the other hole. For a detailed description on plenum design, see Fischer [2].

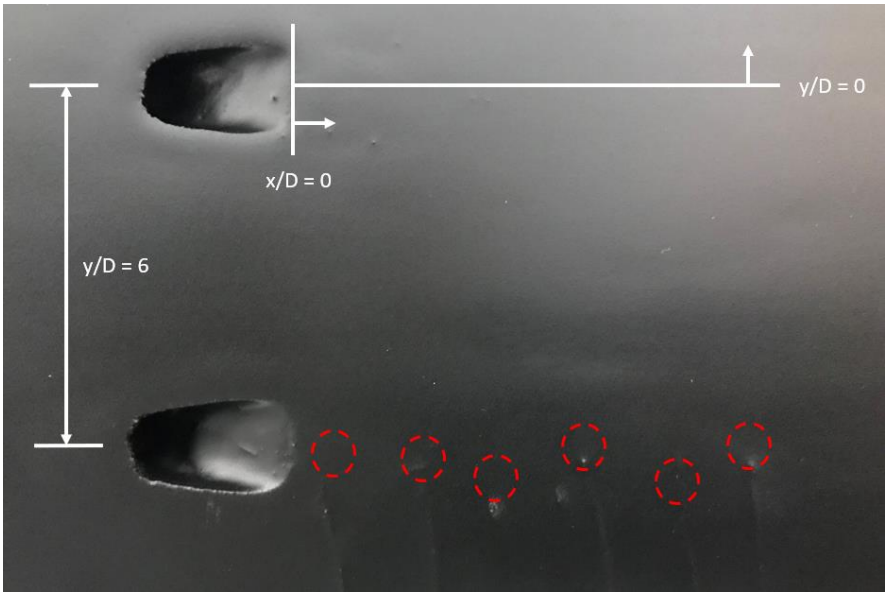

Figure 21: Test surface of two hole test plate with origin, spacing, and thermocouples indicated. PSP has not been applied [2].

3.3 Infrared Thermography Experimental Methods

The experimental methods and testing conditions in this study were the exact same as Fischer [2] and Fischer et al. [29]. The test conditions can be seen in Table 3. Originally, the intent was only to conduct experiments using the PSP method and compare the results to Fischer's IR results [2]. However, after the model was painted with PSP, the trajectory of the coolant onto the surface had changed. A drip of the basecoat of the PSP had settled on the surface in the coolant hole's expanded exit causing the flow to eject asymmetrically downstream of the exit. The drip was filed down to the original coolant hole shape. Filing down the basecoat required the paint inside the coolant hole to be removed as well, which meant that the partial pressure of oxygen could not be detected in those locations. The results of the paint removal can be seen in a later figure inside of the holes, depicted as the white sections in Figure 33. Figure 33 shows white inside both cooling holes as filing corrections were made to both holes. To avoid any discrepancy between the two measurement techniques and eliminate the differences in flow trajectory from the IR results of Fischer [2], the thermal test was repeated with the surface painted with the PSP. The only difference in experimental methods between the experiment by Fischer and this study is that the lights in the test facility needed to be turned off to avoid light exposure to the PSP painted surface which would cause paint degradation.

Table 3: Test Conditions at Steady State.

Test Parameter	Re_D	Mach	T_∞	T_w	T_c	Tu
Value	5000	0.03	327 K	325 K	295 – 305 K	0.67%

The first step in performing a thermal test was turning on the chiller for the mixture of ethylene glycol and water to reach steady state before turning on the coolant flow. The chiller was

set to 285 K so that the coolant for all test points would be between 295 K and 305 K, to achieve a temperature difference of about 30 K between the coolant and the freestream. The next step was to darken the room by turning off all the lights and putting shades over the windows. The clear wind tunnel walls were also coated with Window Whirl, an opaque adhesive cover, to further limit any light coming from electronic devices or any other source in the test facility. After the room was darkened, the test plate was installed in the tunnel and the thermocouples attached to their respective channels in the data acquisition system. Once the model was installed, the tunnel was turned on and heated to steady state testing temperature which was indicated by thermocouples on the tunnel walls reaching steady state at approximately 325 K. The freestream and tunnel wall temperatures were monitored as they were heated. Careful attention was given to the tunnel wall temperature as it was found to have a significant effect on the IR accuracy. More detailed discussion on the IR calibration and accuracy is in Section 3.3.2.

After the test conditions reached steady state, the coolant gas was selected, the coolant flow was turned on, and the data acquisition began. Steady state conditions were reached in two minutes after the coolant flow rate was set. Fischer [2] performed an equilibrium experiment to determine the time to steady state. Fischer performed this by changing the coolant flow rate, then recording the data and taking an image every 10 seconds up to eight minutes. Fischer found that after two minutes settling time, the difference in adiabatic effectiveness values reached steady state condition which were values bounded between $\Delta\eta_T$ = ±0.02 which was less than the expected uncertainty of ±0.04. Thus, two minutes was chosen as steady state for the IR thermal measurement technique.

3.3.1 Infrared Spatial Calibration

Before the data could be processed, a spatial calibration was performed immediately before testing began, for each day of testing. Any slight movement of the model or the camera would result in a dataset of images with a different spatial orientation than the previous dataset. Therefore, a spatial calibration was performed before each new day's dataset to be compared to any other day's dataset. A spatial calibration was necessary since the camera was mounted at an angle to the flat plate test surface. This allowed for the raw IR image to be corrected for size and orientation in the results analysis.

The spatial calibration used in this study was the same as the one used in Fischer [2] and was developed from the methods used in Wiese [17]. In summary, the spatial calibration was accomplished with an identical non-painted plate in lieu of the test plate to avoid damaging the painted surface. A laminated engineering graph paper with pins was attached to the surface of the non-painted plate. With this, the pins could be heated, and a picture taken to get the location of the grid of pins, as seen in Figure 22. The locations of the pins were used in the data reduction to apply a calibration to the image to obtain results of a flat image for analysis.

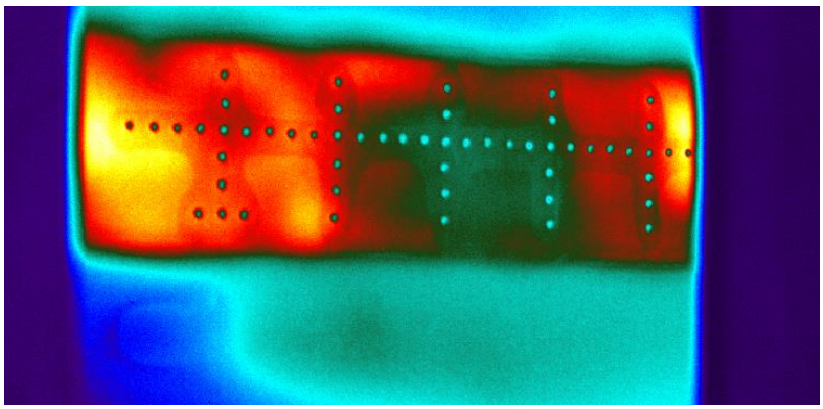

Figure 22: IR spatial calibration image with pin locations.

3.3.2 Infrared Camera Calibration

Along with the spatial calibration, before the data could be processed, an IR camera calibration was performed. The IR camera calibration was performed because the IR camera takes an image in the units of IR counts. IR counts was a unit of the FLIR IR camera data system that was proportional to the radiation that was detected from the surfaces of the camera view. Therefore, the IR counts were converted to temperature in the units of Kelvin through the calibration process. Dissimilar to spatial calibrations, Fischer [2] proved that once the tunnel walls were heated to steady state, the day to day IR calibration remained the same. Thus, a single IR calibration could be used across multiple testing days.

The IR calibration process followed the same methods performed by Fischer [2]. In summary, as previously described, the bottom hole was used for the IR camera thermal calibration and followed the calibration process described by Baldauf et al. [12]. Downstream of the bottom hole, there were six thermocouples embedded in the surface, as shown previously in Figure 21. The data acquisition followed the same experimental methods as described in Section 3.3. However, as the tunnel was heating up, an image was captured so the location of the thermocouples in the IR image could be determined. The thermocouples were distinguishable in the IR image taken as the tunnel was heating since their emissivity was different from the foam plate. Once the tunnel walls reached the steady state temperature of 325 K, the coolant was set to increments of 5 SLPM up to 20 SLPM, and then by increments of 10 SLPM up to the flowmeter max at 50 SLM. At each increment, a data point was recorded at steady state after two minutes had elapsed from the change in flow rate. Once 50 SLPM was reached, the flow rate was decreased in reverse order to detect any hysteresis. Fischer [2] showed that if the tunnel walls had not reached steady state, i.e. if the walls were still heating, this would result in hysteresis and therefore, a bad calibration.

Once the data points were taken, as described by Fischer [2], a MATLAB code would first obtain the recorded location of the pixels where each of the six thermocouples were located, the thermocouples' temperatures, and the associated IR counts for each data point taken. Next, the code would take this dataset and apply a calibration curve fit. The IR calibration curve fit used in this study is shown in Figure 23. The uncertainty, ϵ, was calculated using the standard deviation of the difference in temperature (K) between the data points and the curve fit multiplied by a Student T factor to account for all the data points. The calibration curve resulted in an uncertainty of ±0.5 K.

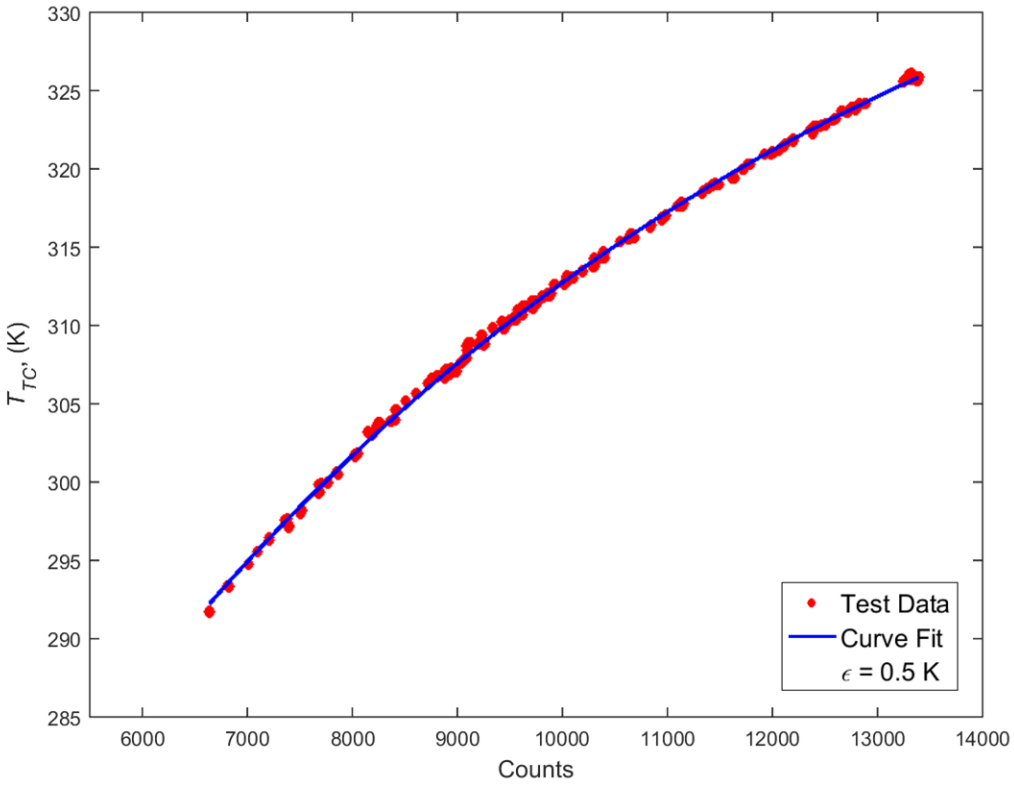

Figure 23: IR thermal calibration used in this study.

Fischer coated the surface of the test plate over the entire region of interest (the view of the sapphire window) with a thin layer of Smooth-On epoxy so that the black paint could be removed, and the surface painted with the PSP. In Fischer's study, the epoxy was painted with a flat black paint as to provide a uniform emissivity surface and reduce reflection for the IR experiments. However, the PSP was pink in color and was a different paint material composition, so the IR calibration for thermal experiments in this study had to be repeated since the emissivity of the surface had changed, and thus shifted the calibration curve. The difference in calibration curves between Fischer [2] and this study can be seen in Figure 24.

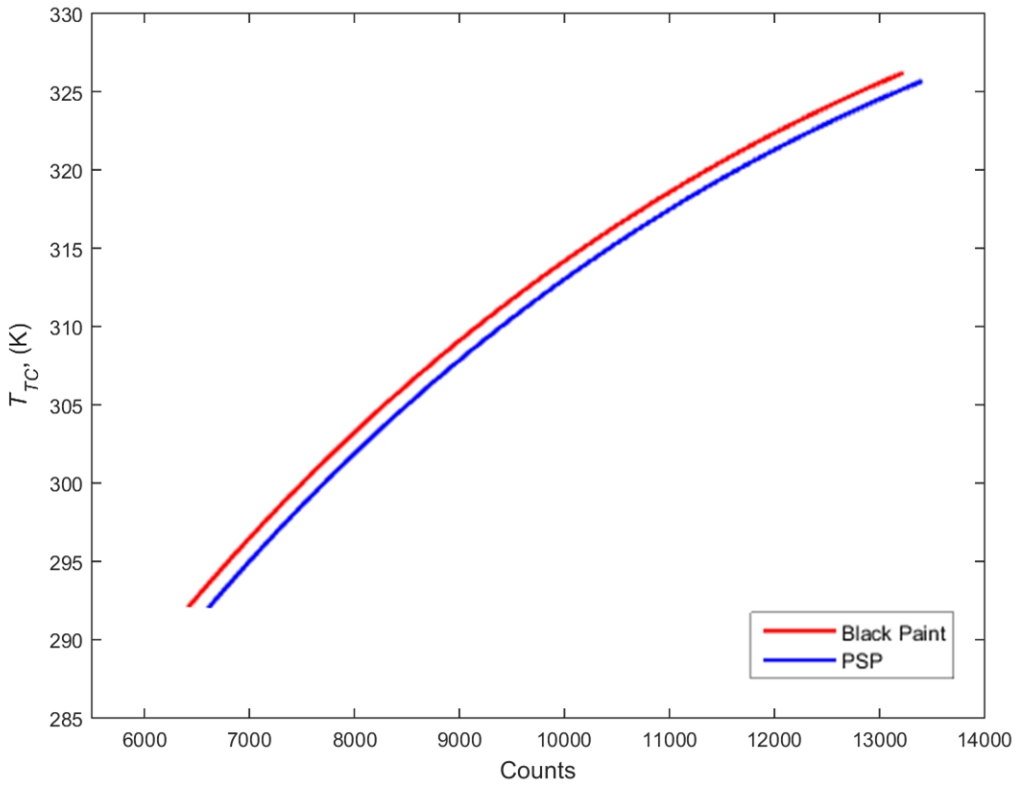

Figure 24: IR thermal calibrations with surface finish comparison.

3.3.3 Thermal Data Reduction

The data reduction process for the thermal measurements followed much of the same procedures and original code written by Weise [17] for a leading edge model, and then adjusted to be applied to a flat plate by Fischer [2]. To record the data, a LabView graphical user interface (GUI) was used to trigger the IR camera as well as record the necessary data. A "Take Data" button was triggered in the LabView GUI after steady state conditions were reached for each data point. The "Take Data" trigger sent a TTL signal through a BNC cable to the IR camera to trigger an image to be taken. The IR camera was connected to a separate computer than where the LabView was hosted and recorded each raw IR image in ExaminIR once the camera captured the image. The data that was recorded in LabView from the test conditions consisted of the freestream Reynolds number, the coolant temperature, and the coolant gas selected with its respective properties at the given temperature. An example of a raw IR test image can be seen in Figure 25.

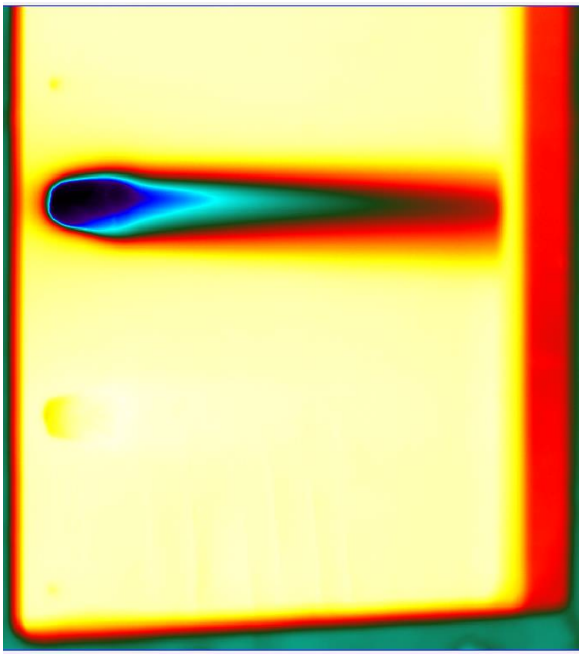

Figure 25: Example of raw IR image with coolant flowing out of test hole.

The data reduction process took the raw IR image, resized it with the spatial calibration, and then applied the IR calibration, Figure 23, to convert IR counts to temperature (K). Now that the surface temperature had been reduced, adiabatic effectiveness could be calculated. First, η_{app} was calculated using Equation (4). Next, η_0 was calculated using three points above and three points below the coolant plume as seen in Figure 26 and described in Section 2.2.1. Typical values of η_0 in this study were between 0.02 and 0.04. Finally, η_T could be calculated using Equation (5). The final η_T results are shown in Chapter 4.

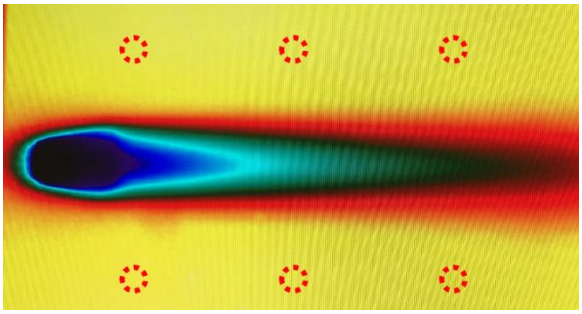

Figure 26: Approximate locations where η_0 is determined, locations where η should be zero.

3.4 PSP Experimental Methods

Another tool commonly used for film cooling experimentation is pressure sensitive paints. PSPs are becoming increasingly popular for conducting adiabatic effectiveness experiments due to their ability to implement the analogy to an adiabatic wall boundary condition even if the material is not adiabatic. Whereas thermal experiments require conduction corrections since the thermal measurement technique cannot account for the fact that no material is truly adiabatic. The question then arises for how the two measurement techniques compare, IR thermography versus mass transfer with PSP. This study is the first to compare adiabatic effectiveness measurements between an IR thermal method and a PSP mass transfer method over a range of the coolant flow

rate parameters *ACR, I, M, ReR,* and *VR* on the exact same PSP painted test article in a non-momentum driven environment: a flat plate geometry, zero degree compound angle coolant injection, with a 7-7-7 cooling hole.

3.4.1 PSP Network and Data Acquisition Setup

The PSP system network consisted of a few more participating devices and programs than for the IR system. A PSP system computer was networked to the LabView host computer, which were both networked with all the PSP system devices on its own local area network (LAN), as seen in Figure 27. The PSP system consisted of a computer, a pulse generator (PSG 3), a lens controller, a CCD camera, and a UV LED excitation light source. The PSP computer hosted two device operating programs, one for the lens controller, and one for the pulse generator. The camera lens aperture and focus were adjusted with the lens controller software prior to any images being taken. The PSG 3 program allowed the user to set the number of pulses for the UV light as well as the time delay for the camera trigger after the UV LED was pulsed. The PSP computer also hosted a data acquisition program called ProAcquire. Through ProAcquire, the user can view the image as seen from the camera. The number of frames, or snapshots, to be taken and averaged for one image was set in ProAcquire. The number of frames would match the number of pulses in the PSG 3 program. Through ProAcquire, the pressure sensitive probe images, the reference probe images, and the average image of the frames taken for both the pressure sensitive probe and the reference probe were recorded for each data point.

The same LabView program and host computer used for the IR data acquisition were used for the PSP system. To swap between experimental techniques, the PSP CCD camera was set up and the BNC trigger cable was swapped from the IR camera to the PSG 3. That BNC cable can be

seen in Figure 27 as the cable between NI BNC 2110 and the PSG 3. Within the LabView program, the only change from IR measurements to PSP measurements would be setting the "Trigger" menu from "Camera" to "PSG", respectively. The TTL signal would trigger the PSG 3, which would in turn send signals to the UV LED and the CCD camera, instead of sending the signal to the IR camera. The LabView program triggered a recording with "Take Data", recorded the same test condition data, and used the same processes as it did for the IR data acquisition. Like ExaminIR, ProAcquire would record an image each time the camera was triggered to capture. However, two more steps needed to be taken to record the PSP images in ProAcquire than it did to record the IR images in ExaminIR. ExaminIR automatically renamed the recorded image when the IR camera was triggered. ProAcquire does not provide sequential naming so each data point had to manually be renamed to save. Also, before hitting "Take Data" in LabView, the user needed to manually set ProAcquire to "Trigger" to record the images for each time the camera was triggered to capture.

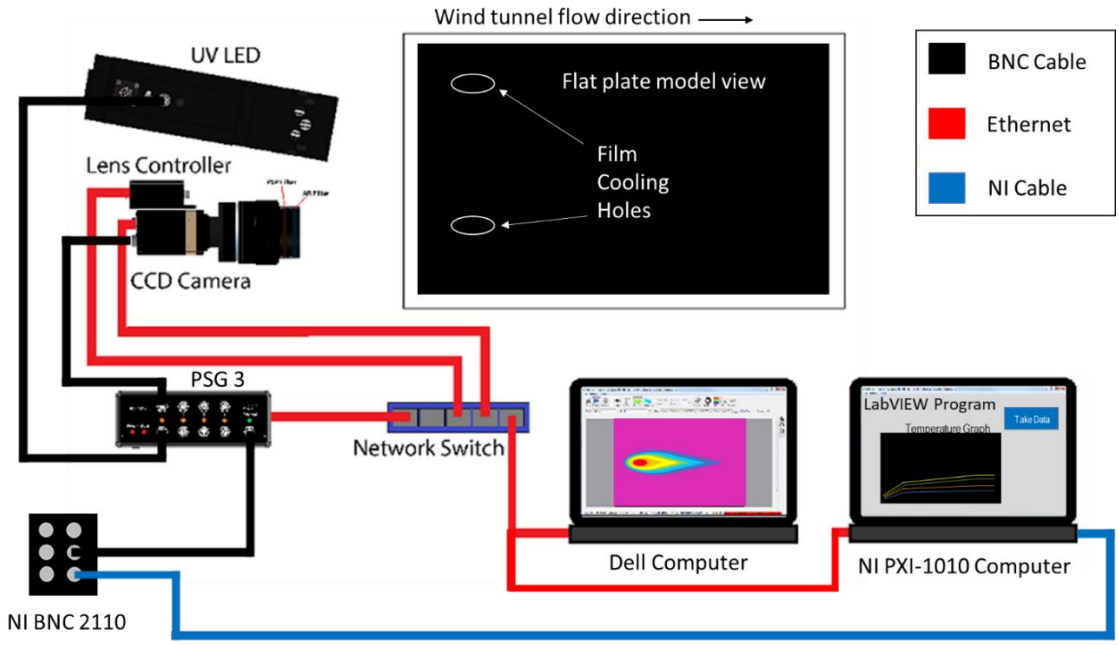

Figure 27: PSP System LAN.

3.4.2 PSP Experimental Methods

The same experimental conditions and methods were used for the PSP measurement technique as were described in the IR thermal experimental methods, the opening of Section 3.3. The test conditions in Table 3 were kept the same between measurement techniques. The same lab setup and model installment were also employed. Although the temperatures and temperature differences used in the IR thermal measurement technique should be irrelevant in the PSP measurement technique using ISSI's BinaryFIB PSP, the tunnel walls were heated, and the chiller was set to the same temperatures for the PSP technique as they were for the IR technique. This was done to limit the difference between IR and PSP measurements to only the measurement technique and to have the same flow conditions and similar uncertainties for both techniques. However, the IR method's required time of two minutes to reach steady state did not need to be applied using this PSP measurement technique as the reaction time to change in pressure for ISSI's BinaryFIB was 300 ms [34].

3.4.3 PSP Image Averaging

Although the reaction time of the BinaryFIB PSP was 300 ms, the flow conditions were considered steady nearly immediately after the flow rate was set and dialed in to match the desired flow rate parameter. Random temporal and spatial fluctuations, from turbulence, were observed in the coolant's placement on the model when the UV light illuminated the PSP coated surface. Due to these coolant flow fluctuations, a single frame for a captured image to record the partial pressure of oxygen on the surface would not entirely depict how the coolant was distributed on the surface downstream of the cooling hole. As previously explained in Section 2.2.4, Han and Rallabandi [8] stated that it was typical to average 200 frames for one data point image. By averaging 200 frames

into one image, the coolant flow interaction with the freestream and the distribution of the coolant on the surface would be considered the average values for steady state conditions.

To validate these findings, an experiment was conducted to test how many frames needed to be averaged to consider the flow conditions to be steady state and to minimize the noise in the adiabatic effectiveness results. Also, the least number of frames averaged for one image was desired. This was because of how much the paint degrades throughout a test with a large dataset. Paint degradation in a large dataset is discussed in further detail in Section 3.4.6. Shown in Figure 28 is the centerline adiabatic effectiveness with the mass transfer analogy, η_M, of a chosen baseline datapoint, N_2 at M = 1, after averaging a series of a set number of frames: 1 frame, 10 frames, 30 frames, 60 frames, and 90 frames. To compare the variation between the different number of frames averaged, each series of frames was subtracted from the 90 frame average image. The results can be seen in Figure 29. To visualize the variation in the images with different numbers of frames averaged, the associated contours are shown in Figure 30. The goal of choosing the appropriate number of frames to average for each image, i.e. data point, for this study would be to select the least number of frames averaged to reduce paint degradation, while also reducing the noise from the fluctuations of partial pressure detected on the surface. The maximum variation in $\Delta\eta_M$ was calculated using Figure 29 for deviations away from the 90 frames averaged image. As soon as the frames averaged was 30 frames or greater, $\Delta\eta_M$ was bounded between $\pm 0.02\ \Delta\eta_M$, the maximum amount of acceptable variation based on uncertainty for the PSP method. Therefore, 30 frames averaged was chosen as the appropriate number for each data point to limit paint degradation while also limiting noise. This meant that the paint was exposed to 30 pulses of the UV light for each data point.

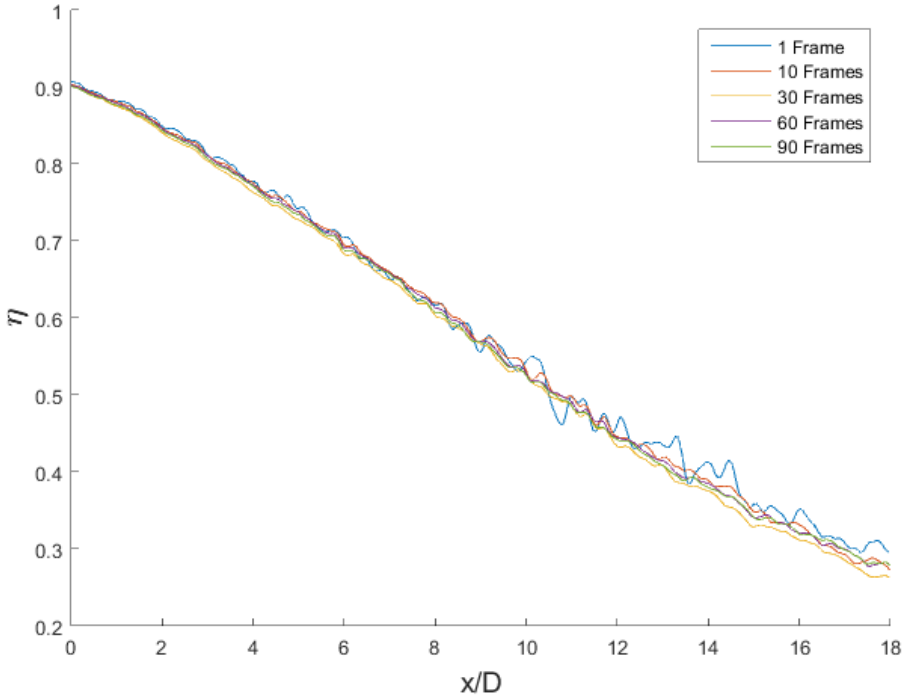

Figure 28: Frame averaging differences in centerline effectiveness.

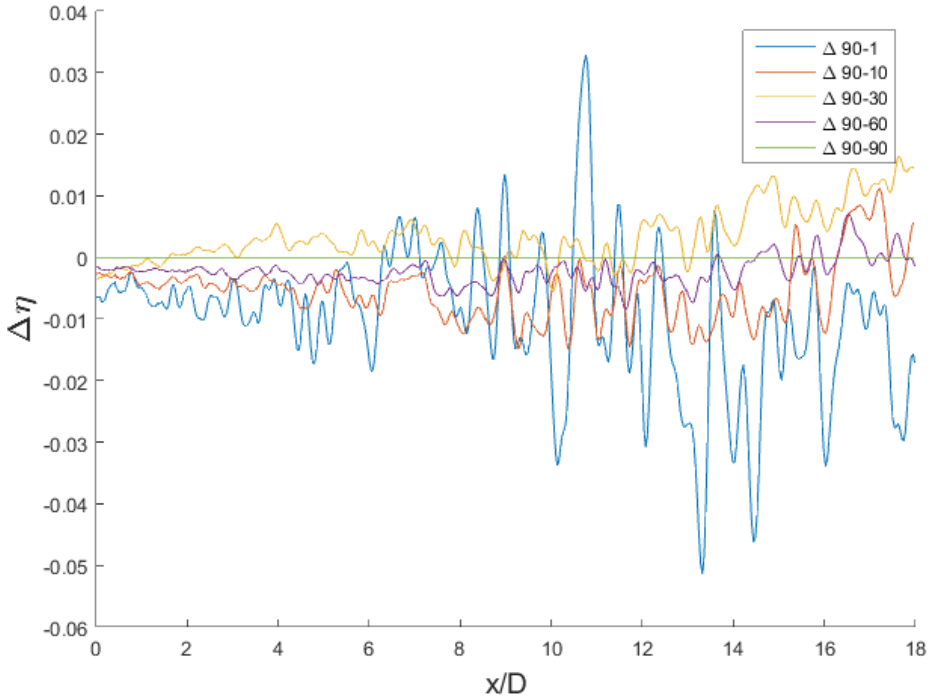

Figure 29: Frame averaging study comparing variation in the number of frames averaged.

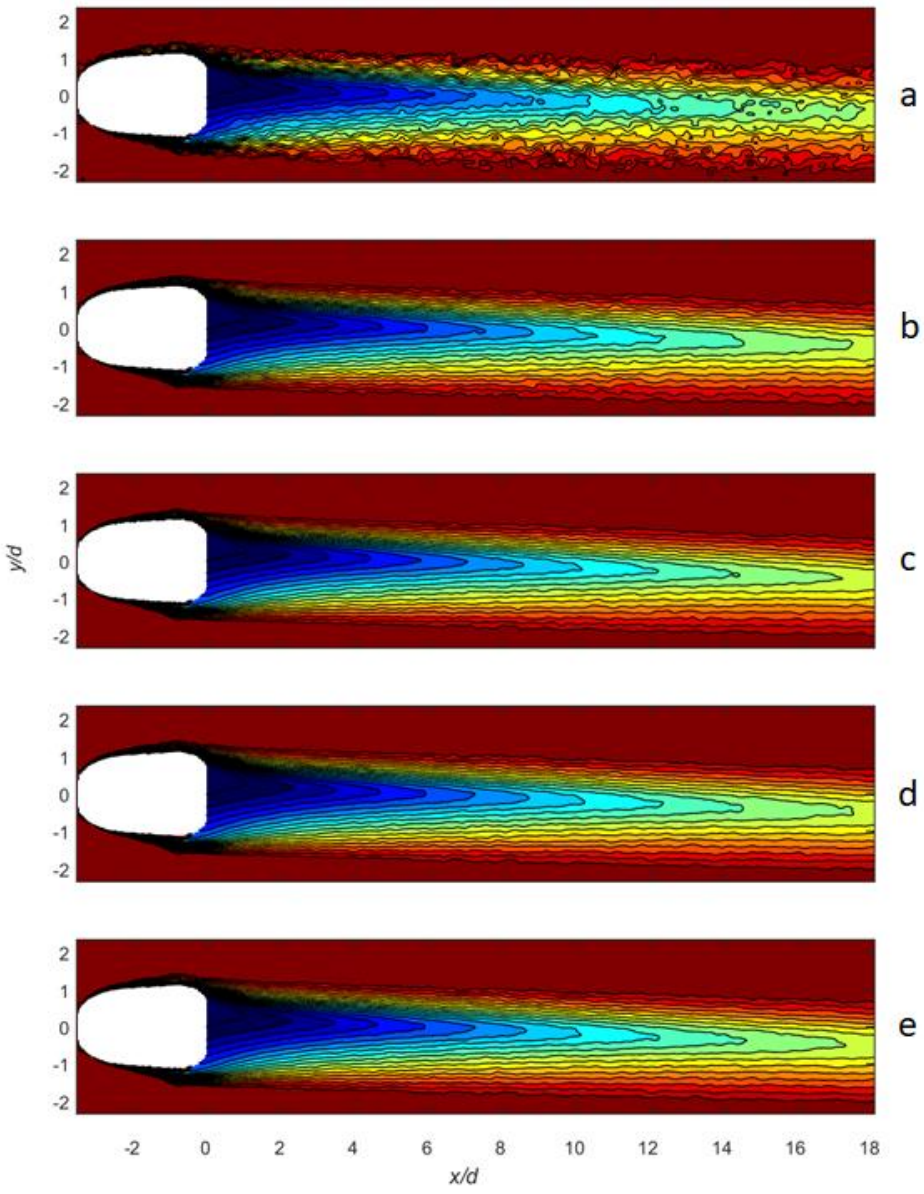

Figure 30: Frame averaging contours: a) 1 Frame, b) 10 Frames, c) 30 Frames, d) 60 Frames, e) 90 Frames.

3.4.4 PSP Spatial Calibration

The spatial calibration using the PSP measurement technique was almost identical in manner to that used with the IR spatial calibration. However, the CCD camera can view the image it sees in black and white, therefore the engineering graph paper with the pins was not used. A regular sheet of engineering paper was applied to the same spatial calibration non-painted plate used in the IR spatial calibration, making sure the paper was level. Then, after the image was taken, several black dots with white borders were added to the grid, as seen in Figure 31, similar to the pins used for the IR spatial calibration. The white dot with a black border, indicated by the yellow arrow, determined the location of the center of the exit of the cooling hole. The code was altered to recognize and reduce the spatial location of the added dots as opposed to the location of the heated pins in the IR spatial calibration. The same calibration technique was applied to the added dots, as was to the pins with IR, to spatially calibrate the image so that a flat image could be analyzed for the results.

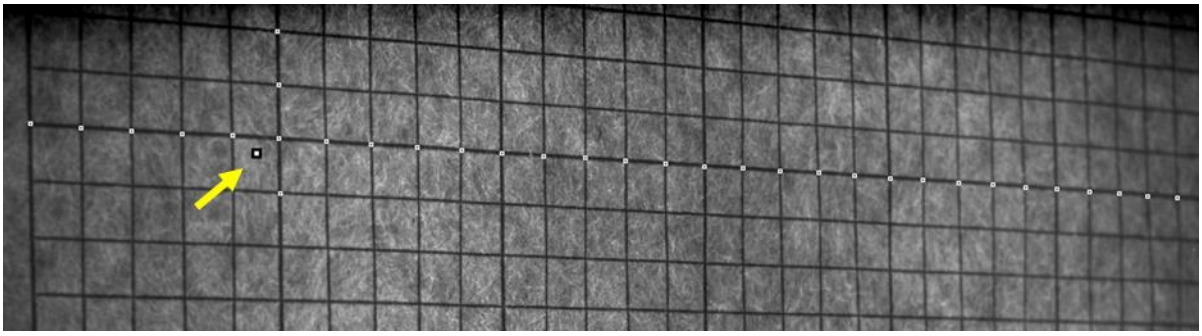

Figure 31: PSP spatial calibration image with added dots.

3.4.5 PSP Reference Image Method and Data Reduction

To recall from Equation (14) in Chapter 2, the adiabatic effectiveness using the heat-mass transfer analogy, η_M, is given by:

$$\eta_M = 1 - \frac{1}{1 + \left(\left(\frac{p_{O_2,\infty}}{p_{O_2,w}} - 1\right)\frac{\mathcal{M}_c}{\mathcal{M}_\infty}\right)}$$

where the two unknowns are the partial pressure of O_2 at the wall when air was flowing as a coolant, $p_{O_2,\infty}$, and the partial pressure of oxygen when a foreign gas was flowing as a coolant, $p_{O_2,w}$. Standard practice, as described by Han and Rallabandi [8] was for a single component PSP where there was only a single pressure and temperature sensitive probe and thus, the experiments using that description needed each data point to have the coolant and the freestream at the same temperature. However, to match the IR thermal experimental conditions from Fischer [2], the coolant and the freestream were at different temperatures. Thus, a binary PSP was used that had a signal probe as well as a reference probe to reduce the function of light intensity off the surface of the PSP to a function of only partial pressure of O_2, as was described in Section 2.2.3 using the wind off/wind on ratio of ratios.

The idea behind taking four images for a data point remained the same between a single component PSP and a binary PSP. The only difference when applying the ratio of light intensities from the wind off reference image to the test image with coolant flowing was that binary PSP adds another ratio of the signal probe to the reference probe to eliminate temperature, with the proper calibration. ISSI has developed a program to reduce the data, called ProImage. ProImage took the three images needed for each coolant scenario, either a foreign gas or air, applied the ratio of ratios along with the calibration curve, and then reduced the result to an image of partial pressure of oxygen on the surface with every pixel in the camera being its own pressure tap. Figure 32 shows

an example of the raw pressure sensitive images taken with the CCD camera for both the foreign gas as a coolant and air as a coolant images. Again, the process to take the pictures was to take the background image, the wind off image, then the wind on images in either order (foreign gas as a coolant and then air as a coolant or vice versa). Since the wind on images were taken consecutively, they can be compared to the same reference images, background and wind off.

Explained in Section 3.3, the cooling hole needed to be fixed due to the base coat of the PSP dripping down into the cooling hole's expanding exit disturbing the flow trajectory onto the surface of the flat plate. Filing down the base coat also removed some paint on the surface inside the cooling hole's exit. The black spots shown in Figure 32 b), c) and d) are the result removing the paint inside the cooling hole. The result of having no paint on the surface also results in the white spots seen inside the hole in the ProImage results, shown in Figure 33.

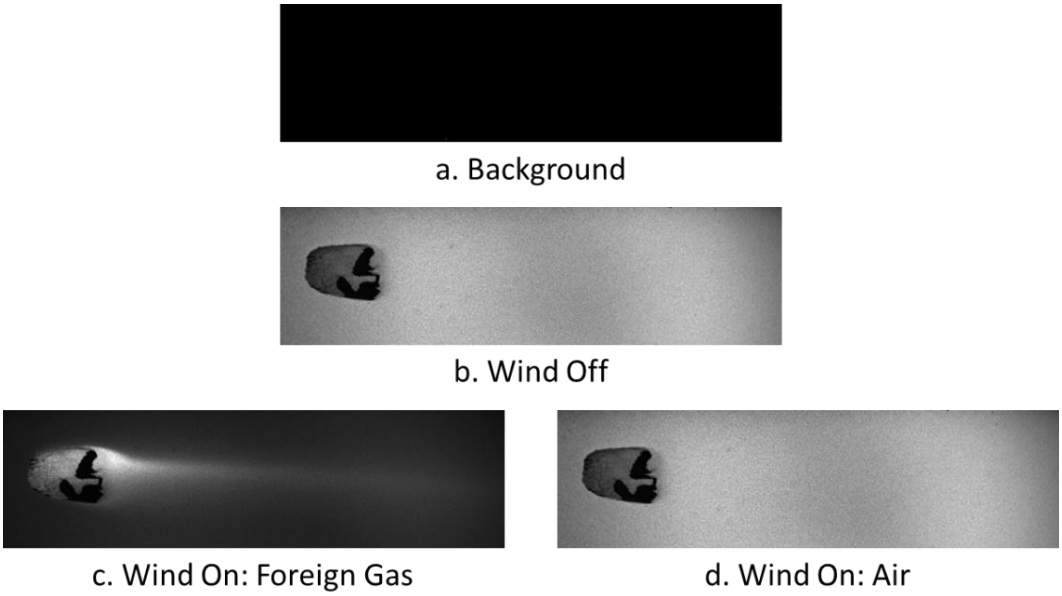

Figure 32: CCD camera images for pressure sensitive probe: reference images a) and b), test images with coolant c) and d).

ProAcquire recorded and saved the average image for each data point as a *.lst* file; one file for each the signal probe and the reference probe. For each coolant case, six *.lst* files were read into ProImage, along with the calibration curve. The six files were the signal and reference *.lst* files for the background, wind off, and wind on images. The files were reduced and converted to the partial pressure of O_2 on the surface, as seen in Figure 33. These partial pressures at each pixel location for a) foreign gas as a coolant and b) air as a coolant, are the values for $p_{O_2,w}$ and $p_{O_2,\infty}$, respectively to put into Equation (14) to solve for η_M.

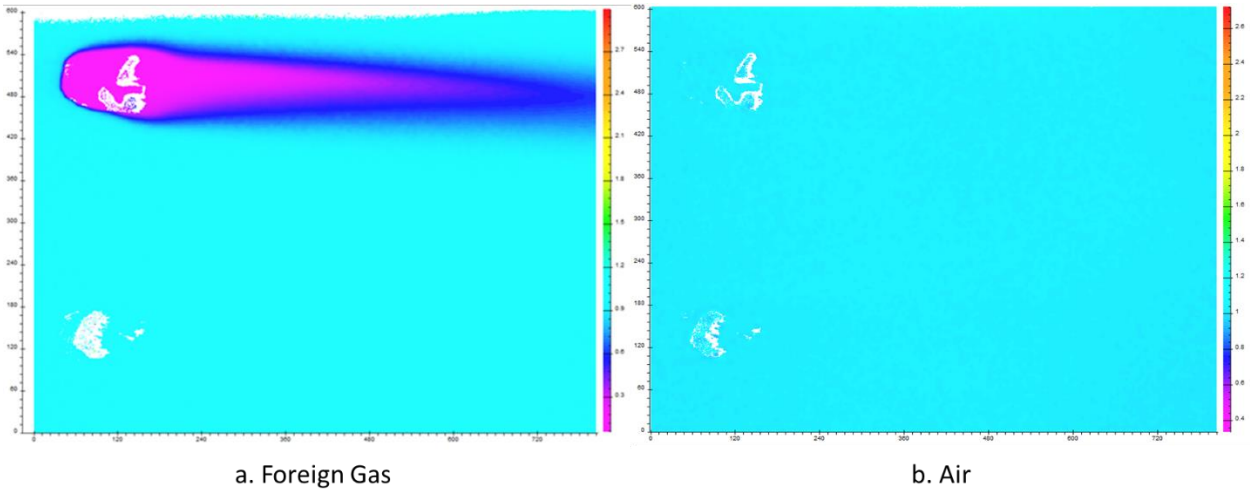

Figure 33: ProImage reduced wind on/wind off ratio of ratios for each coolant case.

A phenomenon experienced by Wiese [17] was that with a scaled up geometry and relatively low Re, the partial pressure of O_2 on the surface did not change when air was flowing as a coolant compared to no coolant flow. This is also shown in Figure 33 b) for this study where air as a coolant is flowing out of the top hole and no coolant is flowing out of the lower hole. Therefore, Wiese developed a new method of taking images for large datasets, as it is crucial to limit the amount of light exposed to the paint to reduce paint degradation. Instead of taking an air

as a coolant image for every foreign gas as a coolant image, Wiese [17] took the foreign gas as a coolant image and averaged the partial pressure of O_2 on the surface where the coolant wasn't flowing. This way, Wiese was able to obtain a surrogate image for actually taking the air as a coolant image. Wiese then took multiple foreign gas as a coolant images and referenced them to the same background and wind off images, assuming the paint had not degraded. The crucial assumption was that the paint had not degraded between images.

3.4.6 Paint Degradation and New PSP Data Collection Method

The current study applied Wiese's method since the air as a coolant case did not produce any partial pressure change where the coolant was flowing on the surface compared to where it was not. It should be noted that where the foreign gas was flowing was where there was little to no oxygen present on the surface. Therefore, where there was foreign gas on the surface was where the luminophores were fluorescing to a higher energy state since they were not being quenched by the presence of O_2 on the surface. This repeated process of the excitation and luminophores fluorescing was what caused the paint to degrade. Thus, where the foreign gas coolant was flowing, the paint degraded at a faster rate than where the coolant wasn't flowing.

The experimental method used in this study for taking reference images and data points is shown in Table 4. Reference images were taken as the first data point (DP), DP 55 near the middle of data points taken, and as the last data point at DP 99. Between these data points are where the test points were taken with foreign gas flowing as a coolant. Throughout the test, five baseline data points were taken at data point numbers 2, 28, 54, 80, and 95 to compare for in test repeatability. The baseline data point was N_2 at $M = 1$. Since the reference images consist of the background image and the wind off image where only the wind off image exposed the paint to the UV light,

the reference images were considered to be one data point. Each data point was considered to expose the paint to the same light degradation since each data point consisted of 30 pulses of the UV light. All data points were taken on the same day and the same test run; about four hours passed between the first data point and the last data point.

Table 4: Baseline Repeatability Test.

Test Data Point (DP) Number	Image Taken
1	Reference images
2	Baseline 1
28	Baseline 2
54	Baseline 3
55	Reference images
80	Baseline 4
95	Baseline 5
99	Reference images

Using Wiese's [17] method for comparing multiple data points to the same reference image while accounting for the partial pressure of oxygen on the surface of each test image individually, the current flow conditions and configuration showed much more paint degradation where the coolant was flowing than where it was not. This proved to be a new prominent issue when using a PSP to collect a large dataset of matched coolant flow rate parameters using Wiese's method to avoid having to repeat the four image method (wind on, wind off, air as coolant, foreign gas as coolant) for every data point taken. Figure 34 shows the centerline η_M for each of the baseline cases referenced to the reference images taken at DP 1, using Wiese's method. The corresponding contours for each baseline in Figure 34 are shown in Figure 35. These figures indicate that averaging the partial pressure of O_2 on the surface in a region out of the coolant plume, even though from the same image, does not account for the paint degradation over the entire surface. In the

current study, the paint showed more degradation where the coolant was flowing than where it was not. Figure 36 and Figure 37 show the centerline η_M, using Wiese's method, for all baselines compared to the reference images taken at DP 55 and DP 99, respectively.

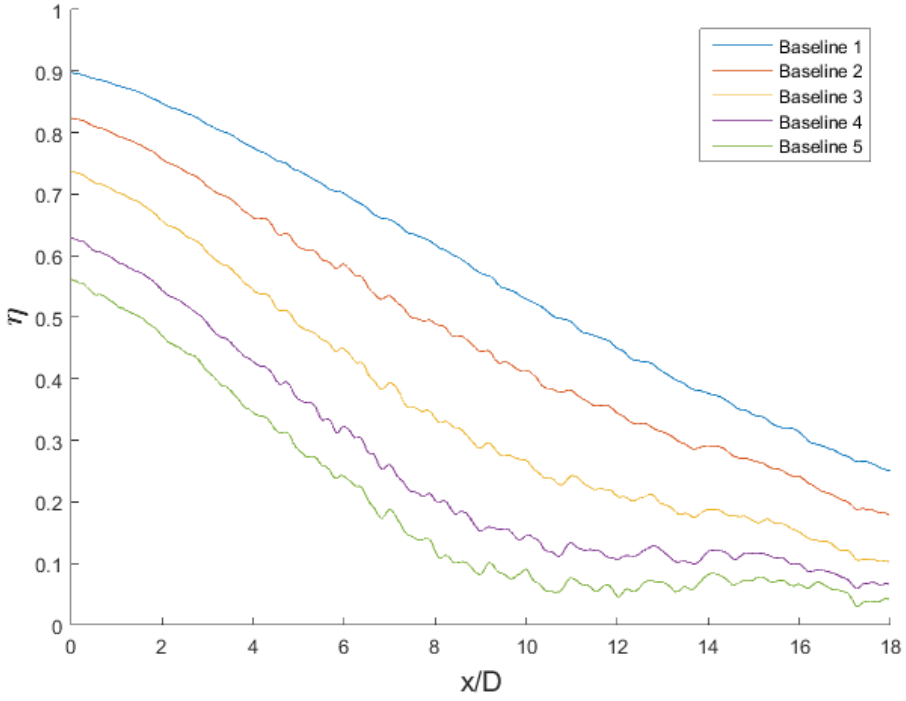

Figure 34: Centerline η_M for all baselines referenced to reference images taken at DP 1.

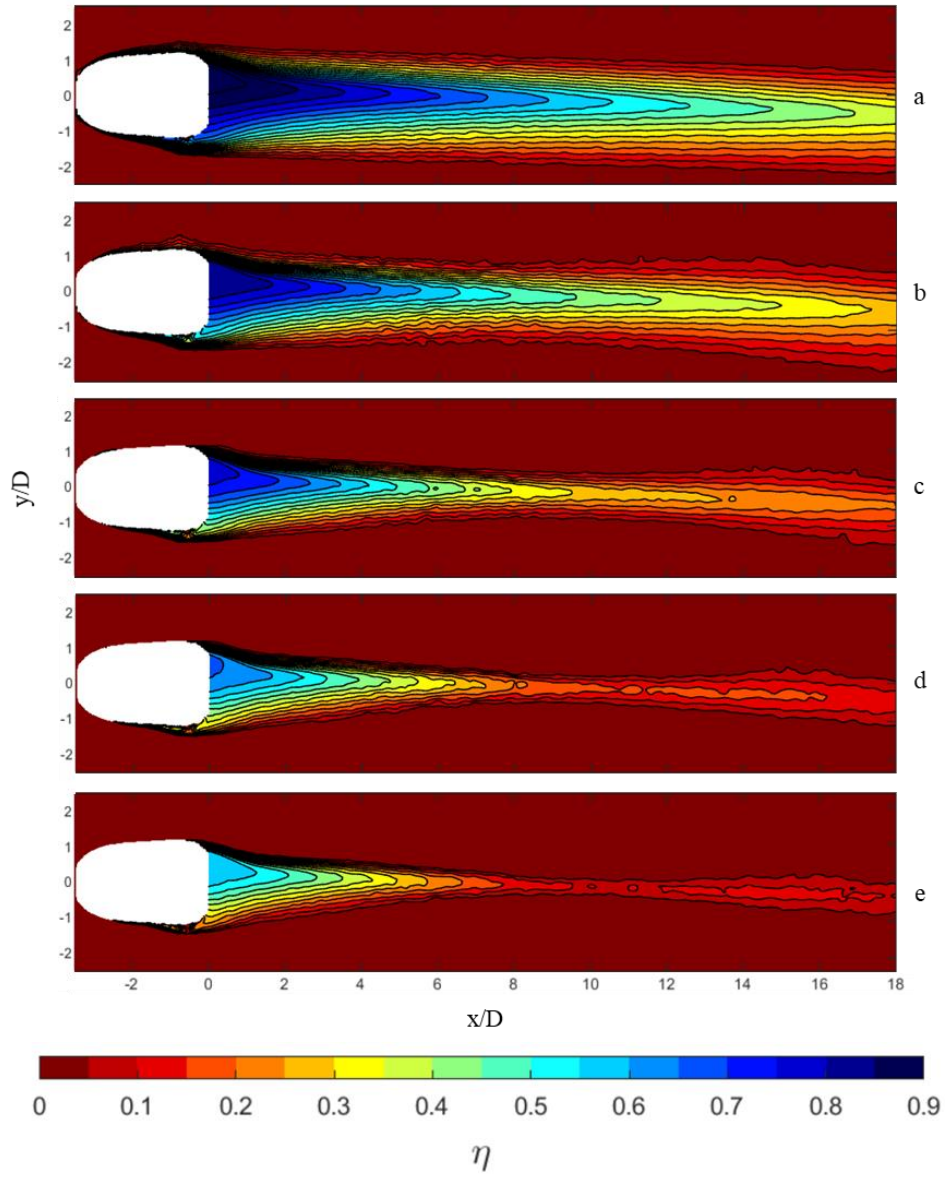

Figure 35: η_M contours for all baselines referenced to reference images taken at DP 1.

a) Baseline 1, b) Baseline 2, c) Baseline 3, d) Baseline 4, and e) Baseline 5.

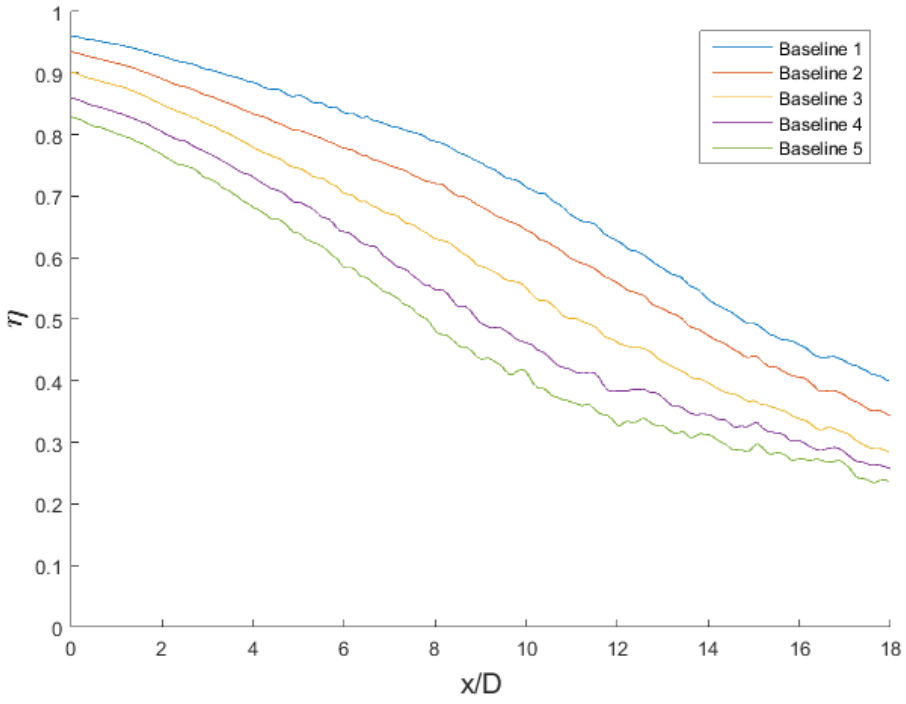

Figure 36: Centerline η_M for all baselines referenced to reference images taken at DP 55.

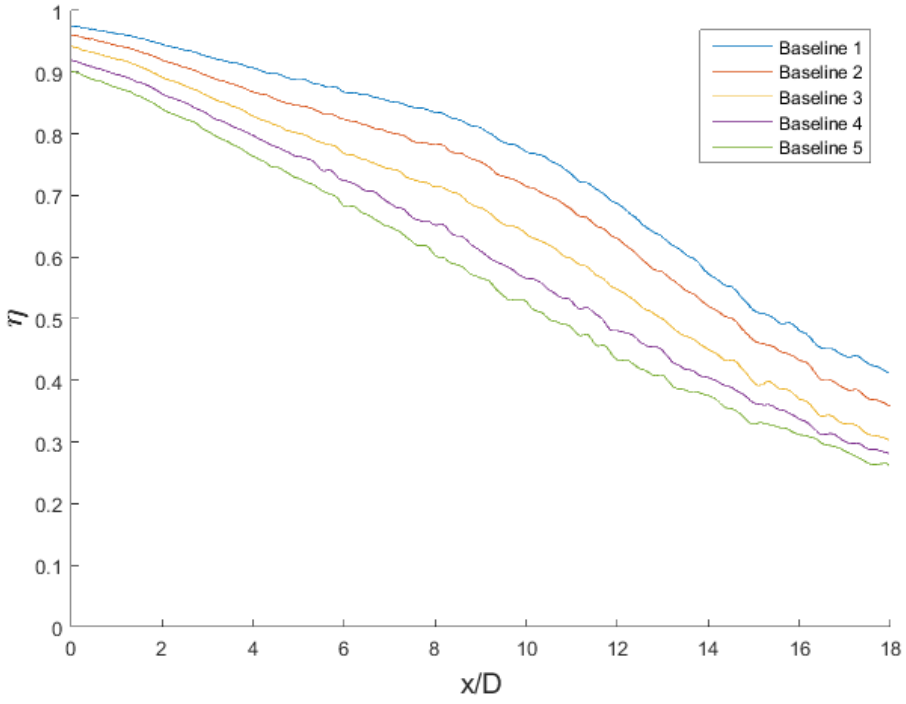

Figure 37: Centerline η_M for all baselines referenced to reference images taken at DP 99.

Figure 34 through Figure 37 show that a new method of comparing test images to references images needed to be developed. The figures also show how much the paint degrades when taking a large dataset. As previously stated, the experimental method in this study reduced the number of averaged frames from a standard 200 frames per data point to 30 frames per data point and reduced the number of total images by a factor of three since the wind off image and air as a coolant wind on image were not taken for every foreign gas as a coolant data point. The ratio of ratios process using Wiese's method still indicated an apparent lower effectiveness, which was the result of the paint degrading. Therefore, a new method of using reference images was developed.

The new method began with the idea of Wiese's [17] method to use each foreign gas as a coolant image for the partial pressure of O_2 for the air as a coolant image to reduce the number of images taken and therefore, paint degradation. Also, the paint did not degrade at the same rate where the coolant was flowing to where it was not. Thus, instead of averaging the partial pressure of O_2 on the surface only where the coolant wasn't flowing, the entire region was averaged. Then, it was compared to reference images taken before the test data point and after the test data point. A linear interpolation of each pixel in the test image was taken between the reference images before and after the test data point. The weighted average interpolation was based on the PSPs amount of exposure time to the UV LED between each set of references images. Now, the paint degradation at each individual pixel location had been accounted for. Figure 38 shows the centerline η_M of the baselines using the new method of taking large datasets with PSP to account for, and limit paint degradation. Figure 39 shows the respective new contours for the baseline images. The weighted average interpolation between reference images allowed the baseline images to converge to $\pm 0.02\ \Delta\eta_M$. This method was applied to the entire dataset.

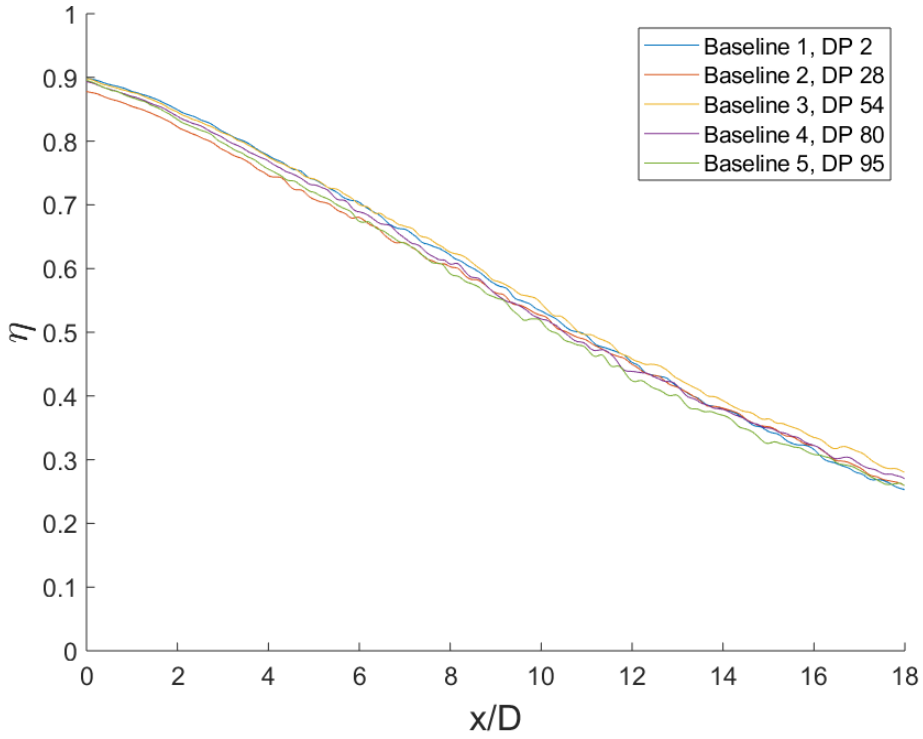

Figure 38: Centerline η_M for all baselines using the weighted average interpolation.

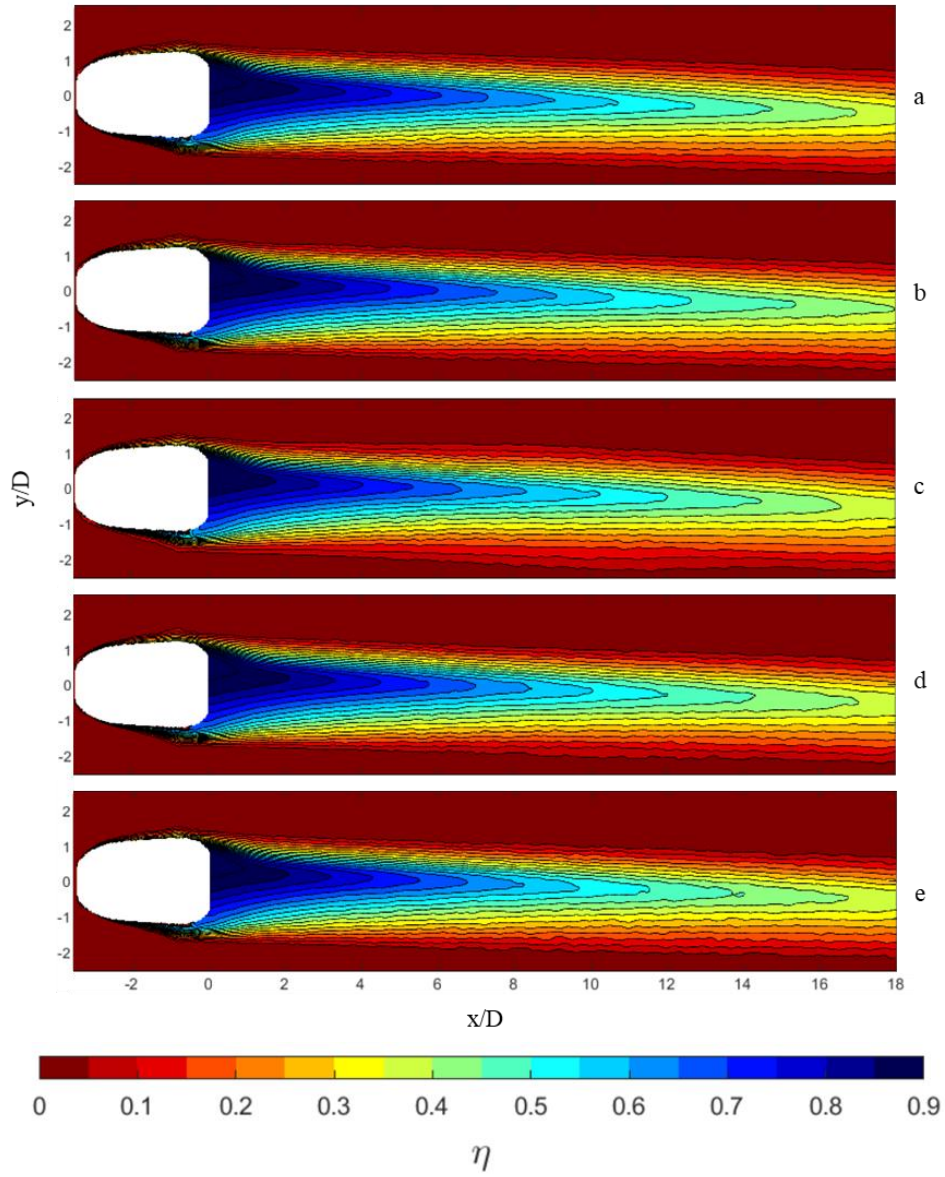

Figure 39: η_M contours for all baselines using the weighted average interpolation.

a) Baseline 1, b) Baseline 2, c) Baseline 3, d) Baseline 4, and e) Baseline 5.

3.5 Uncertainty Analysis

The uncertainty analysis presented in this study used the root-sum-square (RSS) method of Kline and McClintock [35]. The objective of the RSS method is to express the result of the overall uncertainty by combining the estimation of the uncertainty of the individual measurements, ζ_i. The effect of the uncertainty of an individual measurement is the partial derivative of the resulting uncertainty with respect to the individual measurement, $\frac{\partial \zeta}{\partial \zeta_i}$, called the sensitivity coefficient, multiplied by the known uncertainty of that measurement, ε_{ζ_i}. These individual uncertainties are combined by the RSS method to give the overall uncertainty, shown in Equation (23).

$$\varepsilon_\zeta = \sqrt{\left(\frac{\partial \zeta}{\partial \zeta_1}\varepsilon_{\zeta_i}\right)^2 + \left(\frac{\partial \zeta}{\partial \zeta_2}\varepsilon_{\zeta_2}\right)^2 + \cdots + \left(\frac{\partial \zeta}{\partial \zeta_n}\varepsilon_{\zeta_n}\right)^2} \tag{23}$$

3.5.1 Freestream and Coolant Flow Uncertainty

Many experiments have been run in the same facility of the current study, from Wiese [17] to Fischer [2], and utilized much of the same data reduction methods and processes, a detailed explanation of the uncertainties for the freestream flow, the coolant, and all gas properties can be found in Wiese [17]. Uncertainty of the freestream Reynolds number was calculated to be ±1% from the test condition set at Re_D= 5000. Temperatures collected with thermocouples: freestream temperature, tunnel wall temperature, and coolant temperature, were subject to the thermocouple's standard uncertainty of ±0.3 K. As previously stated, the gas properties used were found using the ideal gas law with linearly interpolated values from published datasets. The corresponding uncertainties for coolant-to-freestream gas property ratios can be seen in Table 5. The flowmeter used in this study carried a factory uncertainty and as the coolant flow rate increased, the relative uncertainty decreased. The uncertainty as a function of mass flow rate reading, in SLPM, can be

seen in Figure 40. A flow rate greater than 5 SLPM was required for every data point taken in this study, therefore, the maximum uncertainty was ±3%.

Table 5: Gas Property Ratio Uncertainty. Adapted from [17].

$\varepsilon_{\rho_c/\rho_\infty}$	$\varepsilon_{c_{p,c}/c_{p,\infty}}$	$\varepsilon_{\mu_c/\mu_\infty}$	$\varepsilon_{D_{AB,c}/D_{AB,\infty}}$
0.2%	0.7%	2.8%	8.5%

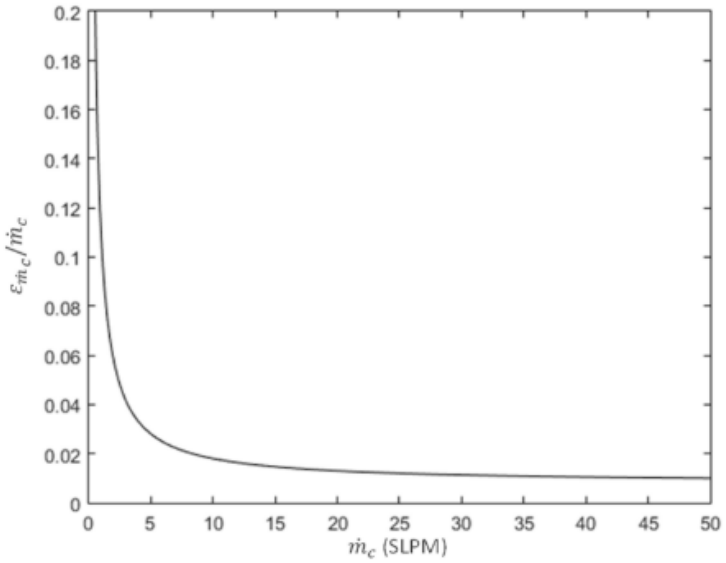

Figure 40: Uncertainty of coolant mass flow rate [17].

3.5.2 Thermal Adiabatic Effectiveness Uncertainty

The total adiabatic effectiveness uncertainty for the thermal measurement technique, $\varepsilon_{\eta,T}$, was calculated using Equation (23). All uncertainties listed in this section were used, as well as the IR camera calibration uncertainty of ±0.5 K. $\varepsilon_{\eta,T}$ was determined by first calculating the uncertainty with respect to the apparent adiabatic effectiveness, $\varepsilon_{\eta_{app}}$, and the uncertainty with respect to the conduction correction, ε_{η_0}, from the methods presented by Fischer [2]. The

maximum and minimum $\varepsilon_{\eta,T}$ were calculated at two surface locations of two test points. The two test points were chosen to have the highest and lowest temperature differences, ΔT, from the freestream to the coolant, $\Delta T = T_\infty - T_c$. The highest ΔT was 38K and the lowest ΔT was 18 K. The maximum and minimum surface temperatures were then selected for the highest and lowest ΔT data points to result in the maximum and minimum uncertainties. The final $\varepsilon_{\eta,T}$ values for the selected data points can be seen in Table 6. The highest uncertainty, ±0.042, resulted from low η values and low ΔT, whereas the lowest uncertainty, ±0.024, resulted from high η values and high ΔT.

Table 6: Maximum and minimum η uncertainties for the IR measurement technique.

	$\Delta T = 38K$		$\Delta T = 18K$	
	Lowest T_s	**Highest T_s**	**Lowest T_s**	**Highest T_s**
$\varepsilon_{\eta,T}$	0.024	0.034	0.032	0.042

As $\varepsilon_{\eta,T}$ provides the advantage that any measurement error resulted in some bias error, it does not, however, provide any randomly distributed error. Since the entire dataset with the thermal measurement technique was accomplished on the same day, the observed repeatability at a specific coolant flow rate condition throughout the testing day provides a better characterization of the measurement uncertainty. The coolant flow rate condition chosen was selected as M = 1 with air as the coolant gas. The facility conditions remained the same as described in Section 3.3. Six baseline data points were taken resulting from points taken as the first data point of the testing, between each gas, and as the last data point during testing. Figure 41 shows the centerline adiabatic effectiveness for each of the baseline cases. On a 95% confidence interval using a t-distribution,

the average repeatability was 0.007 across *x/D* values from 0 to 18. The maximum $\Delta\eta$ between the six baseline cases resulting in η_T bounded by ±0.014.

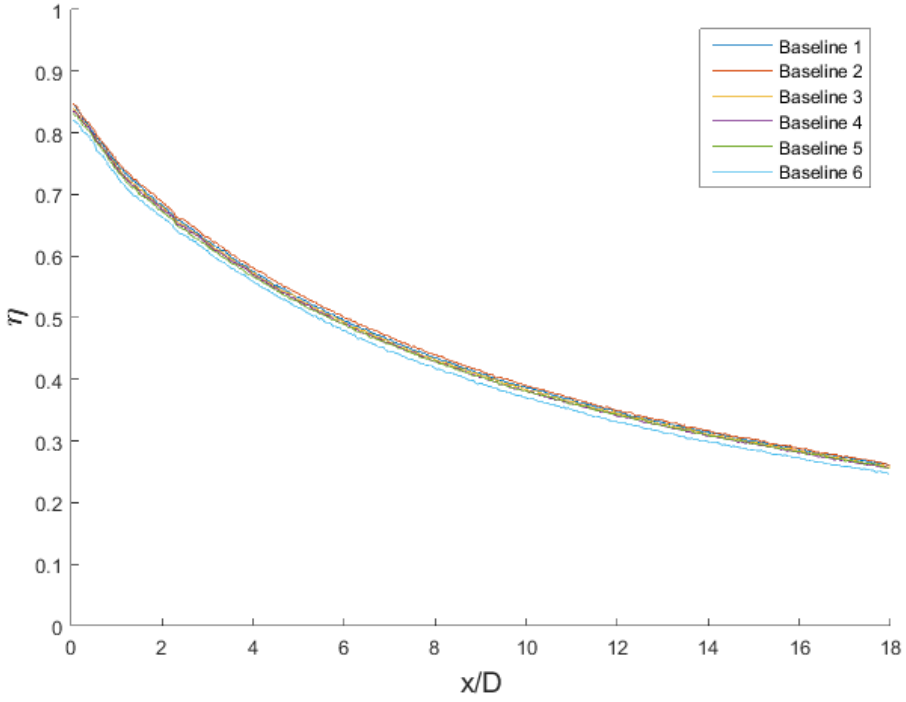

Figure 41: Baseline repeatability using IR measurement technique.

3.5.3 PSP Adiabatic Effectiveness Uncertainty

The uncertainty for adiabatic effectiveness using the PSP measurement technique was based on the uncertainty in the partial pressure of oxygen at the wall. In Equation (14), only $p_{O_2,w}$ and $p_{O_2,\infty}$ were based on measurements as all other variables were considered constant for this study. However, there is uncertainty in the measurement of p_{O_2} for both coolant scenarios, air and foreign gas. In Section 2.2.3, it is explained in detail how the measurement of p_{O_2} on the surface begins as a function of pressure, temperature, illumination, and luminophore concentration, then reduces to a function of only pressure using ISSI's developed method of the ratio of ratios and the

calibration of the paint over a range of temperatures shown in Figure 3. The methods using a binary PSP reduce the uncertainty in the measurement of p_{O_2} to 50 Pa/K [16]. However, using the uncertainty in the measurement of p_{O_2}, the RSS method was applied to test cases where the highest uncertainty occurred: at the highest ΔT in the location where Δp_{O_2} on the surface was the greatest, immediately downstream of the coolant hole exit. Δp_{O_2} is defined as $\Delta p_{O_2} = p_{O_2,\infty} - p_{O_2,w}$. The total adiabatic effectiveness uncertainty for the mass transfer measurement technique, $\varepsilon_{\eta,M}$, as calculated using Equation (23), was ±0.014.

In Section 3.4.6, a new method was developed for using a binary PSP to conduct an experiment with a large dataset. Like the IR experiment, the observed repeatability of a coolant flow rate condition throughout a test provides better characterization of uncertainty over the measurement uncertainty, p_{O_2} on the surface in the case for the PSP experiment. Same day repeatability was accomplished by taking a baseline data point, N_2 at M = 1, multiple times throughout the test: at the beginning of testing, between each gas, and at the end of testing. The repeatability using the new data methods of this study were shown previously in Figure 38 for centerline adiabatic effectiveness. On a 95% confidence interval using a t-distribution, the average repeatability was 0.012 across *x/D* values from 0 to 18. The maximum $\Delta\eta$ between the five baseline cases resulting in η_M bounded by ±0.019.

4. Results and Discussion

The purpose of this chapter is to analyze the completed experiments of this study to accomplish the objectives of the research. The first objective was to determine the best coolant flow rate parameter to use with a pressure sensitive paint measurement technique and the second objective was to compare the two experimental techniques, thermal and mass transfer. The first objective will be discussed in Section 4.1, while also discussing part of the second objective comparing the adiabatic effectiveness results between the two techniques. Section 4.2 analyzes a broader scope when comparing the two experimental techniques. Finally, Section 4.3 offers an analysis of an observation that was not an objective of this study, upstream adiabatic effectiveness.

4.1 Adiabatic Effectiveness Results

To evaluate the efficacy of the five studied coolant flow rate parameters (*ACR*, *I*, *M*, *ReR*, and *VR*) to scale adiabatic effectiveness, each parameter was matched to the values in Table 7 using four foreign gases (Ar, CO_2, He, and N_2) with IR and PSP. The flow rate for each gas was incrementally increased to set matched values of each coolant flow rate parameter, values of 0.25, 0.50, 1.00, 1.50, and 2.00. Due to limitations of the flowmeter for flow rates greater than 50 SLPM, not every value could be matched, specifically those that required high flow rates for He. However, once the dataset given in Table 7 was completed during the PSP experiment, the coolant flow was switched to a flowmeter with a 500 SLPM limit flow rate to accommodate unreached matched parameters for He, values shown in Table 8. The higher flow rate He datapoints were only gathered using the PSP measurement technique. This is the first time that data points requiring flow rates higher than 50 SLPM for He were acquired in this facility.

Table 7: Data points collected with 50 SLPM limit flowmeter with IR and PSP.

Gas	Coolant Flow Rate Parameter	Matched Value
Ar, CO_2, N_2	*ACR*	0.25, 0.50, 1.00, 1.50, 2.00 (Ar did not have 2.00)
	I	0.25, 0.50, 1.00, 1.50, 2.00
	M	0.25, 0.50, 1.00, 1.50, 2.00
	ReR	0.25, 0.50, 1.00, 1.50, 2.00
	VR	0.25, 0.50, 1.00, 1.50, 2.00 (IR did not have 2.00)
He	*ACR*	0.25, 0.50, 1.00, 1.50
	I	0.25, 0.50
	M	0.25
	ReR	0.25
	VR	0.25, 0.50, 1.00, 1.50, 2.00 (IR did not have 2.00)

Table 8: Data points collected with 500 SLPM limit flowmeter with PSP.

Gas	Coolant Flow Rate Parameter	Matched Value
He	*ACR*	2.00
	I	1.00, 1.50, 2.00
	M	0.50, 1.00, 1.50, 2.00

To compare the data, several methods were used: η contour plots, centerline η values, spanwise η values, laterally averaged η values ($\bar{\eta}$) and area averaged η values ($\bar{\bar{\eta}}$). The contour plots show the adiabatic effectiveness distributions over a region showing the entire hole and the entire region of interest, defined as downstream distances of *x/D* from 0 to 18, and the lateral region of *y/D* ±2.5. The centerline η plots show values of η for both techniques at *y/D* = 0 over *x/D* from 0 to 18. The spanwise η plots show values of η at *x/D* = 3.0 over *y/D* ±2.5. The $\bar{\eta}$ plots laterally

average the data from *y/D* ±2.5 for every *x/D* value between 0 and 18. The $\bar{\bar{\eta}}$ plots average over downstream distances of *x/D* from 0 to 18, and the lateral region of *y/D* ±2.5. This method of analyzing and displaying the data was applied in the same manner for both the IR and PSP experimental techniques. In the plots comparing PSP to IR for centerline η, $\bar{\eta}$, and $\bar{\bar{\eta}}$, the IR data is shown as the solid lines and the PSP data is shown as the dashed lines. Furthermore, to reiterate, the thermal results shown in this study using the IR measurement technique are from a repeat of the study performed by Fischer [2], and the same data used in Fischer et al. [29]. However, the bounds and calculations of η, $\bar{\eta}$, and $\bar{\bar{\eta}}$ for the thermal dataset follows what was previously mentioned for this study.

The data shown for the following centerline η plots and $\bar{\eta}$ plots will also display the value of the other coolant flow rate parameters for each gas at the specified matched parameter value. Along with the coolant flow rate parameters, density ratio (*DR*), Lewis number ratio (*LeR*), specific heat ratio (*CpR*), dynamic viscosity ratio (μR), thermal conductivity ratio (*kR*), and binary diffusion coefficient ratio (*BDR*) were calculated at each data point. A summary of the average values over the entire dataset, with bounds, of these ratios can be seen in Table 9.

Table 9: Experimental gas property ratio values.

	Ratio					
Gas	*DR*	*LeR*	*CpR*	μR	*kR*	*BDR*
Ar	1.50 ±0.04	0.92 ±0.02	0.52 ±0.00	1.15 ±0.02	0.63 ±0.02	0.95 ±0.00
CO_2	1.68 ±0.06	0.56 ±0.02	0.83 ±0.01	0.75 ±0.02	0.58 ±0.03	0.81 ±0.00
He	0.15 ±0.01	2.08 ±0.07	5.16 ±0.00	0.99 ±0.03	5.25 ±0.15	3.47 ±0.01
N_2	1.08 ±0.02	0.90 ±0.01	1.03 ±0.00	0.89 ±0.01	0.91 ±0.01	1.00 ±0.00

4.1.1 Advective Capacity Ratio (*ACR*)

ACR was the first parameter to be evaluated based on the findings of Fischer [2] which showed ACR's ability to near perfectly scale adiabatic effectiveness over a variety of gases. With *DR* values ranging from 0.15 to 1.65, the inclusion of the ratio of specific heats to the blowing ratio allowed *ACR* to collapse adiabatic effectiveness profiles for cases where the jet remains fully attached, values of $I < 0.50$, on a flat plate with zero-degree compound angle coolant injection. The contours for $ACR = 0.25$ are shown in Figure 42 for visualization of η distributions on the surface. Figure 43 and Figure 44 show the collapse of η for the IR technique. For the success seen with *ACR* using an IR technique, it was not expected for the results to correlate to the PSP measurement technique.

The thermal measurement technique was able to capture the thermal relations between the coolant and the freestream with *ACR* by the inclusion of the ratio of specific heats, or more importantly the ratio of heat capacities, $\frac{(\rho c_p)_c}{(\rho c_p)_\infty}$. The PSP measurement technique loses that capability by only being able to detect the concentration of O_2 on the surface which is analogous to where the coolant was not on the surface. The effect of how the coolant is able to maintain its temperature as thermal diffusion and conduction occurs from the hot freestream is lost with PSP. This is shown in Figure 43 and Figure 44 for low values of *ACR* where the coolant is assumed to be attached at $I < 0.50$, according to Fischer et al. [29]. The figures show that the IR method was able to collapse the data with the inclusion of *CpR*, where the PSP method was not and the adiabatic effectiveness with the mass transfer method was ordered with decreasing *CpR* values, Ar having the lowest and He having the highest. The hypothesis is confirmed as PSP was not able to scale adiabatic effectiveness with *ACR*.

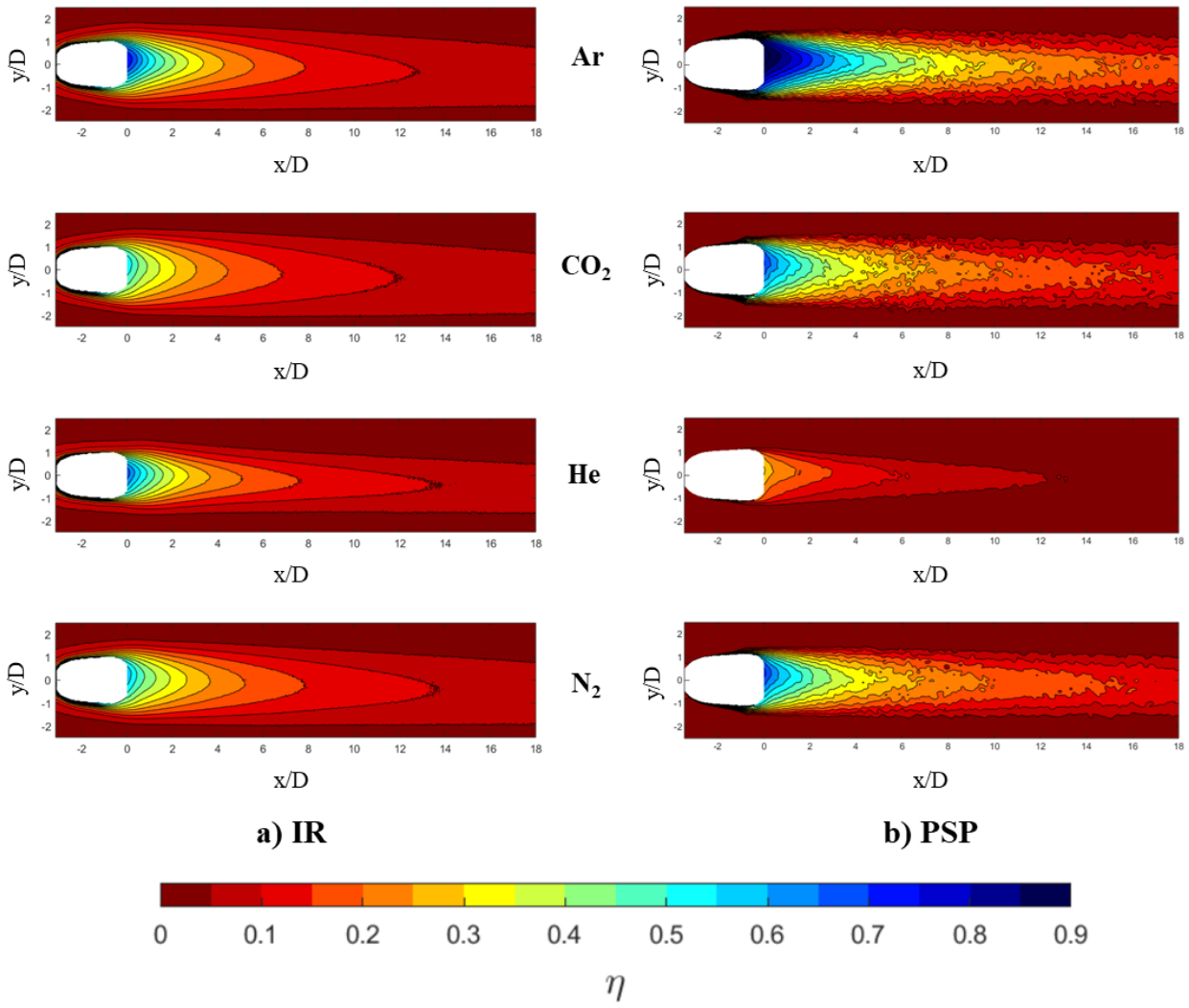

Figure 42: Contours of η at ACR = 0.25 for IR and PSP. a) IR and b) PSP.

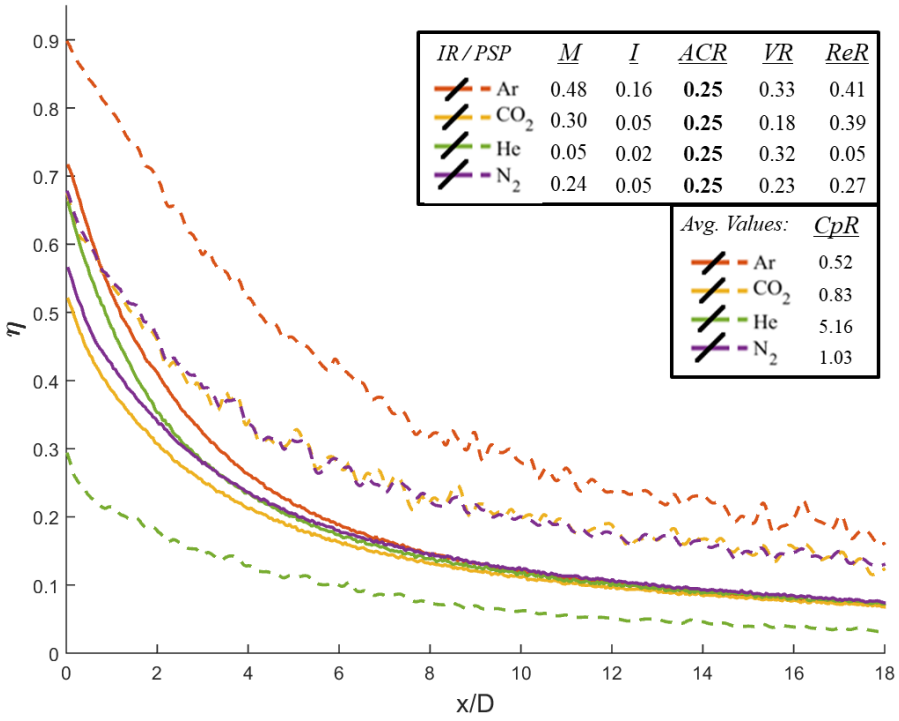

Figure 43: η distributions along y/D = 0 at ACR = 0.25 with IR and PSP.

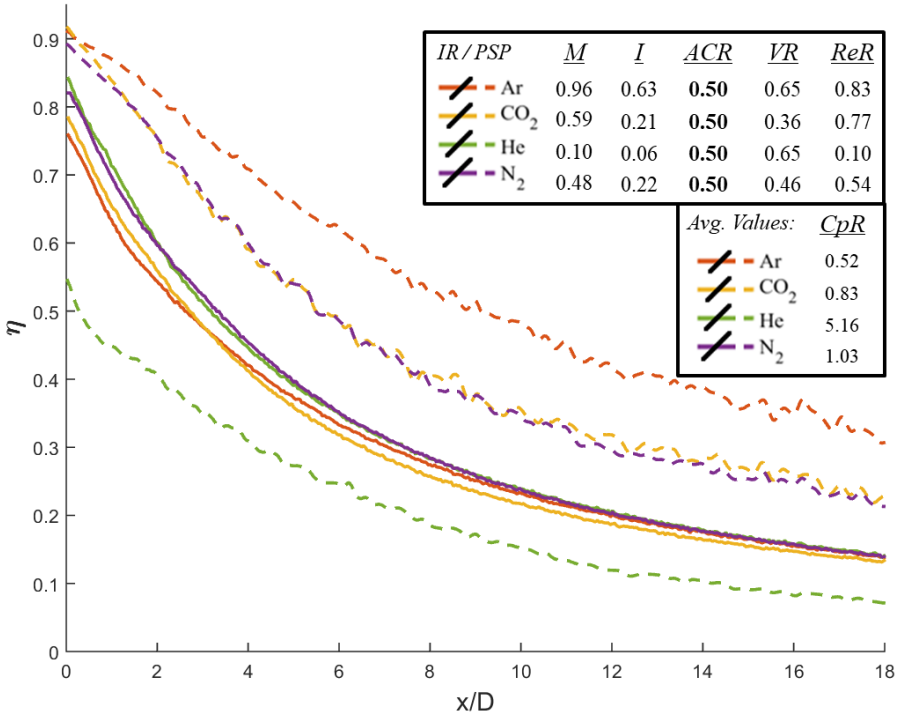

Figure 44: η distributions along y/D = 0 at ACR = 0.50 with IR and PSP.

At higher values of *ACR*, the *I* values also increased which has been linked to jet separation effects, discussed in detail in Section 4.1.2. When separation effects began to occur, the grouping of the gases with *ACR* began to split with the thermal data. Fischer et al. [29] attributed this to having an *I* value greater than where the onset of separation began after $I = 0.50$. Figure 45 shows the centerline η values after separation for all gases except He. The trend for the IR method is that the highest value of η corresponded to the lowest *I* value with He where the lowest value of η corresponded to the highest *I* value with Ar. The grouping of CO_2 and N_2 had similar *I* values. Fischer [2] noted that the trend was as *I* increased, the magnitude of η decreased and the discrepancy of CO_2 having a lower *I* value than N_2 but having a higher η can be attributed to uncertainty as the grouping was close enough that if both gases fall on the opposing sides of the uncertainty bounds, the η values can oppose the trend of increasing *I* with decreasing η. However, that trend of the IR data does not track with the PSP method.

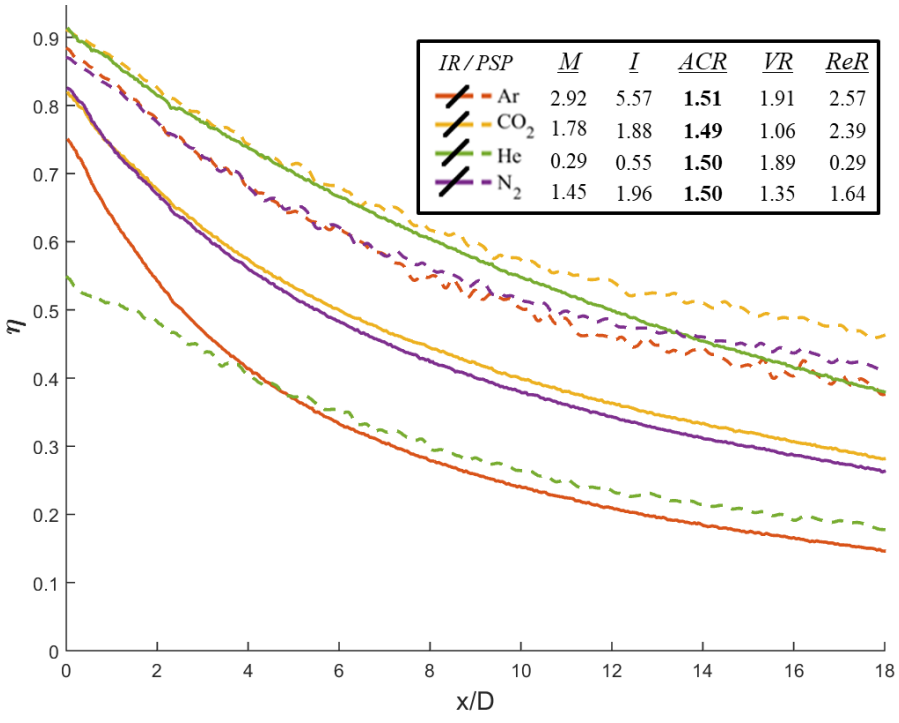

Figure 45: η distributions along *y/D* = 0 at *ACR* = 1.50 with IR and PSP.

The most powerful visualization of the scaling ability of *ACR* with the thermal measurements is with $\bar{\bar{\eta}}$ plots. Shown in Figure 46 are the $\bar{\bar{\eta}}$ plots with IR and PSP. For the IR case, Figure 46 shows that no matter the density or specific heat of the coolant, adiabatic effectiveness was scaled at low values of *ACR* as the gases follow the same curve and then one by one begin to deviate from the curve. The deviation from the curve is attributed to the *I* value of jet separation near $I = 0.60$. The *I* values at the deviation point for each gas is labelled in Figure 46 for the IR method. For the PSP method, the $\bar{\bar{\eta}}$ plots with *ACR* do not collapse the data like the IR method which further indicates that *ACR* is not the appropriate coolant flow rate parameter to scale η results between different gases with mass transfer methods.

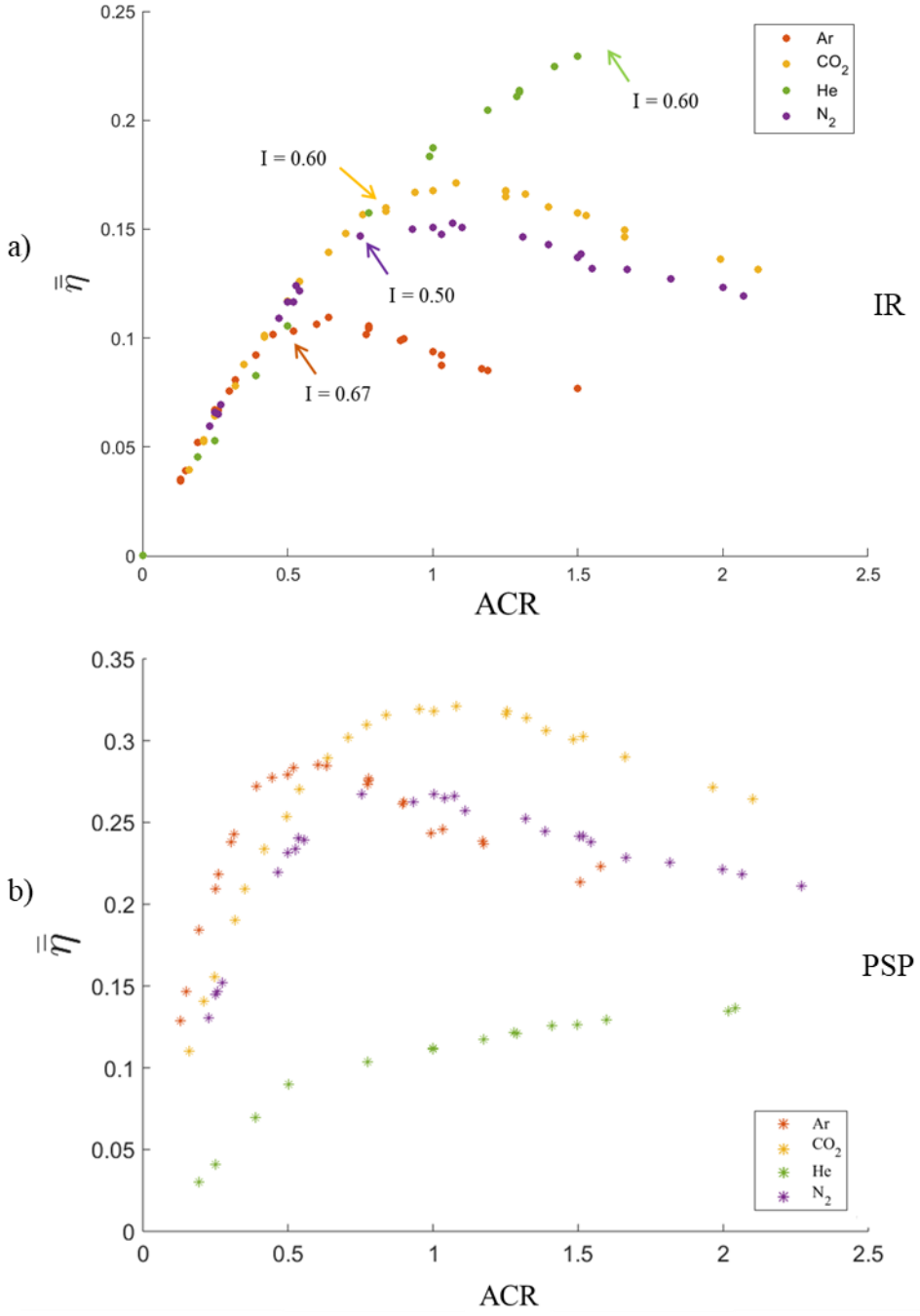

Figure 46: $\overline{\overline{\eta}}$ vs. *ACR* for all test cases. Deviation points with corresponding *I* values labelled for the IR data. a) IR and b) PSP.

4.1.2 Momentum Flux Ratio (*I*)

As jet separation has been shown to influence adiabatic effectiveness distributions, the momentum flux ratio was the next parameter evaluated. Shown in Figure 47 is the centerline η plot at $I = 0.25$ for both experimental techniques. It can be seen that for the IR method, *I* was not able to scale the data. However, similar to how with matched *ACR*, for the thermal method, the highest magnitude of η corresponded to the lowest value of *I*, and as *I* increased, the magnitude of η decreased. The opposite trend is seen here as the IR data shows that at matched *I*, the highest η values correspond to the highest values of *ACR*, and the close grouping of CO_2 and N_2 correspond to very similar *ACR* values, then the lowest η value corresponds to the lowest *ACR*. This is expected as a higher heat capacity means it takes a greater amount of energy to change the temperature of the flow, so at matched *I*, the highest magnitude of η corresponds to the highest value of *ACR* and the trend shows as the value of *ACR* decreases, the magnitude of η decreases.

For the PSP method in Figure 47, if He was removed from the data, one may be inclined to think that *I* is the appropriate scaling parameter for mass transfer methods. This shows the importance of having a gas with properties drastically different than the other gases, such as He compared to Ar, CO_2, and N_2. Until recently, with the study by Fischer [2], He has not been used in film cooling studies. He drastically increases the spectrum of gas property variations to truly assess the ability of the nondimensional coolant flow parameters to scale film cooling effectiveness. Shown previously in Table 9, He's gas property ratios are on the opposing side of unity compared to Ar, CO_2, and N_2 with the main exception being the μR. One other exception exists with the specific heat ratio of N_2. However, He's *CpR* is five times unity. Also, with He, the *DR* is much lower, but *CpR*, *LeR*, *kR*, and *BDR* are higher values. Furthermore, the close grouping

of Ar, CO_2, and N_2 in Figure 47 does not appear to be by accident as all three of those gases have very similar M values where He shows lower η values for a lower M value.

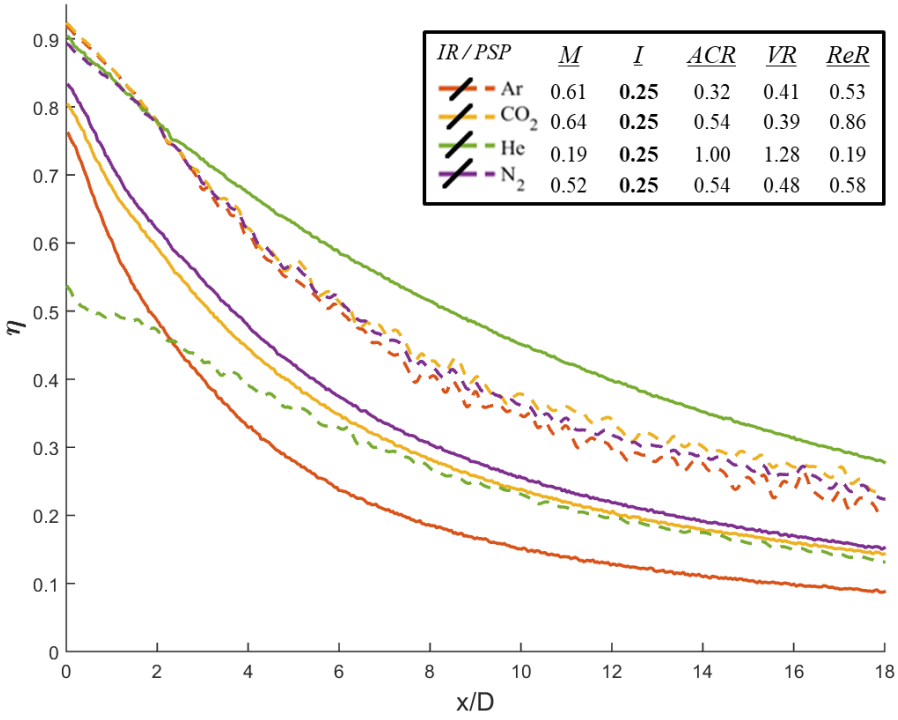

Figure 47: η distributions along y/D = 0 at I = 0.25 with IR and PSP.

Although I does not prove to be a good scaling parameter for either thermal or mass transfer experiments, it does offer insight for the dynamics of the jet and can be used to predict jet separation. This relationship of I with jet separation has been consistent with many findings in previous literature. To best analyze and visualize the jet dynamics, $\bar{\bar{\eta}}$ plots are used and shown for both IR and PSP in Figure 48. When I is matched, the peak value for the IR method and the PSP method occur at about the same value at I = 1.00. Although, there is an exception with He for PSP. The peak value of I for He with PSP seems to occur at about I = 1.70, but the peak value is nearly reached at I = 1.00 and the magnitude of $\bar{\bar{\eta}}$ maintains near the peak value for He much longer than the other three gases. The $\bar{\bar{\eta}}$ plots show that I scales the peak $\bar{\bar{\eta}}$ between both techniques.

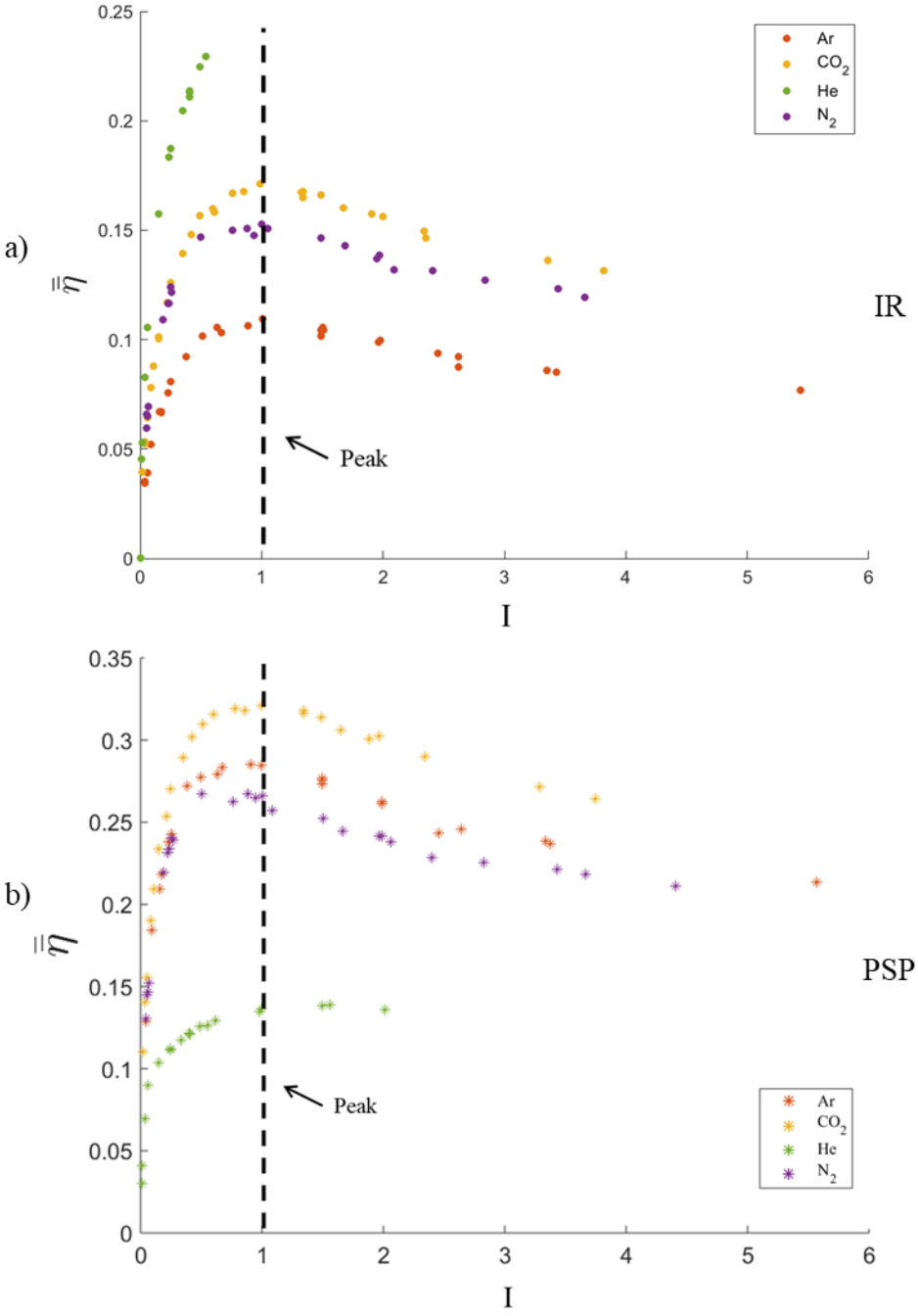

Figure 48: $\overline{\overline{\eta}}$ vs. *I* for all test cases with peak *I* value labelled. a) IR and b) PSP.

Figure 49 shows the centerline η plot at I = 1.50, after the critical value for both IR and PSP. He is not a part of the dataset with the IR technique as the flow rate was beyond the 50 SLPM limit of the low flow rate flowmeter that was in use for the thermal experiment. The reason higher flow rates for He using the thermal method were not needed was that the dataset involving only Ar, CO_2, and N_2 was sufficient to show that I was not a good scaling parameter at I = 1.50. However, as previously stated, He data was acquired with PSP at high values of *ACR*, *I*, and *M* with a higher flow rate flowmeter. It is shown here that the same trend with matched I is prevalent with the IR method as the close grouping of CO_2 and N_2 correspond to similar *ACR* values and Ar has a low *ACR* value. However, with PSP, the grouping of Ar, CO_2, and N_2 began to separate with increased I values higher than the peak value of I = 1.00. Like the $\bar{\bar{\eta}}$ plot, the highest value of η corresponds to highest value *DR* and also the lowest value of *BDR*. As *DR* decreases and *BDR* increases, η decreases with the PSP technique.

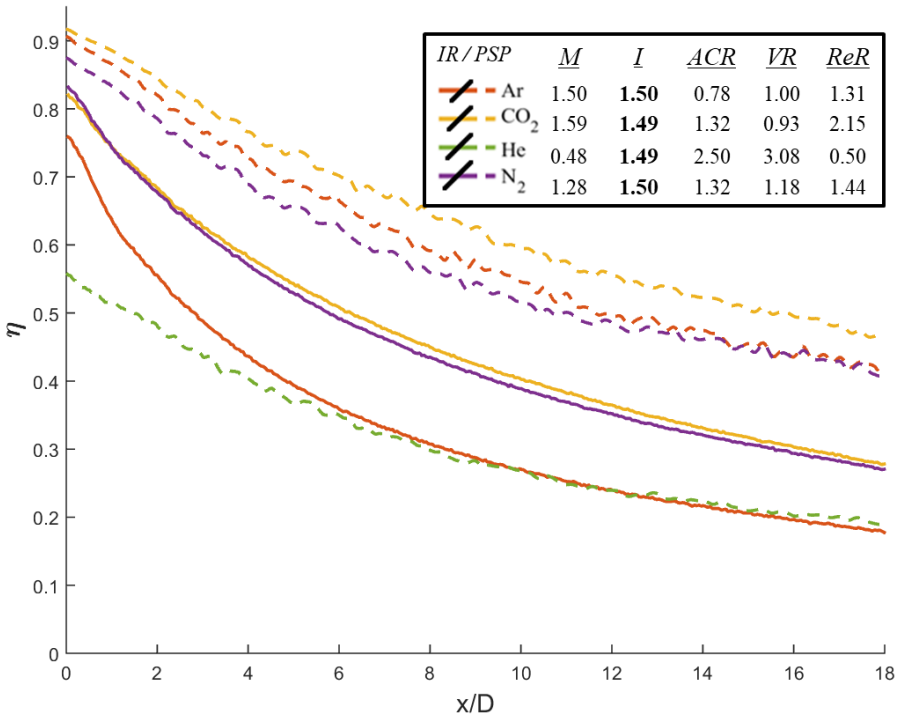

Figure 49: η distributions along y/D = 0 at I = 1.50 with IR and PSP.

4.1.3 Mass Flux Ratio (*M*)

ACR is the *M* multiplied by *CpR*. The inclusion of *CpR* to *M* was what allowed *ACR* to scale adiabatic effectiveness with the IR thermal measurement technique. However, as described in Section 4.1.1, *ACR* could not scale adiabatic effectiveness between the different gases with the PSP technique because the mass transfer analogy loses the thermal physics that are captured with the inclusion of *CpR*. Figure 50 shows the contours at $M = 0.25$ and Figure 51 shows the centerline η values at matched $M = 0.25$ for both techniques. When *M* was matched, the specific heats of the gases were not accounted for and thus, *M* did not scale η with the IR technique. Although, it should be noted that with the IR method, the values of increasing η magnitude between the gases with matched *M* correspond to increasing values of *ACR*, and therefore, *CpR*. However, with the PSP technique, when the mass flux ratios for each gas were matched, *M* was able to scale η fairly well in the centerline η plot. When the data was laterally averaged from *y/D* ±2.5 along *x/D* values of 0 to 18, *M* collapsed η with the PSP mass transfer method, shown as $\bar{\eta}$ values in Figure 52. It should be noted that *y/D* ±2.5 was chosen as the bounds for lateral averaging because the adiabatic effectiveness coolant plume was bounded by those values for both the IR and PSP techniques for the entire dataset. Despite the large variations in gas properties between the gases, *M* near perfectly scaled η between the four gases by laterally averaging over the entire coolant plume with the PSP data. It is important to note that since *M* is the coolant flow rate parameter that scaled the PSP data between the four gases and *M* does not capture thermal relations, the mass transfer technique cannot scale η from ambient to engine conditions because the thermal effects are not accounted for.

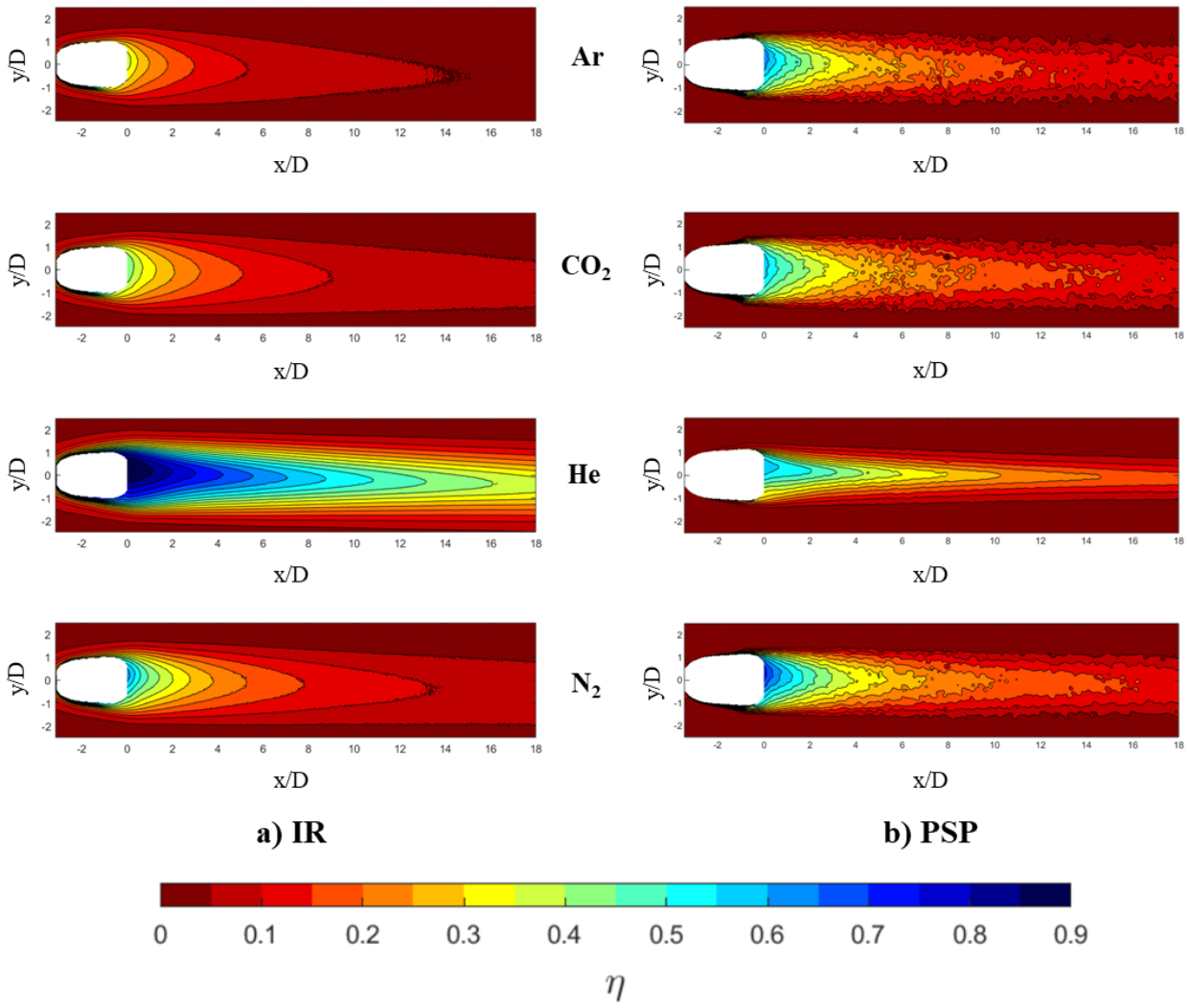

Figure 50: Contours of η at M = 0.25 for IR and PSP. a) IR and b) PSP.

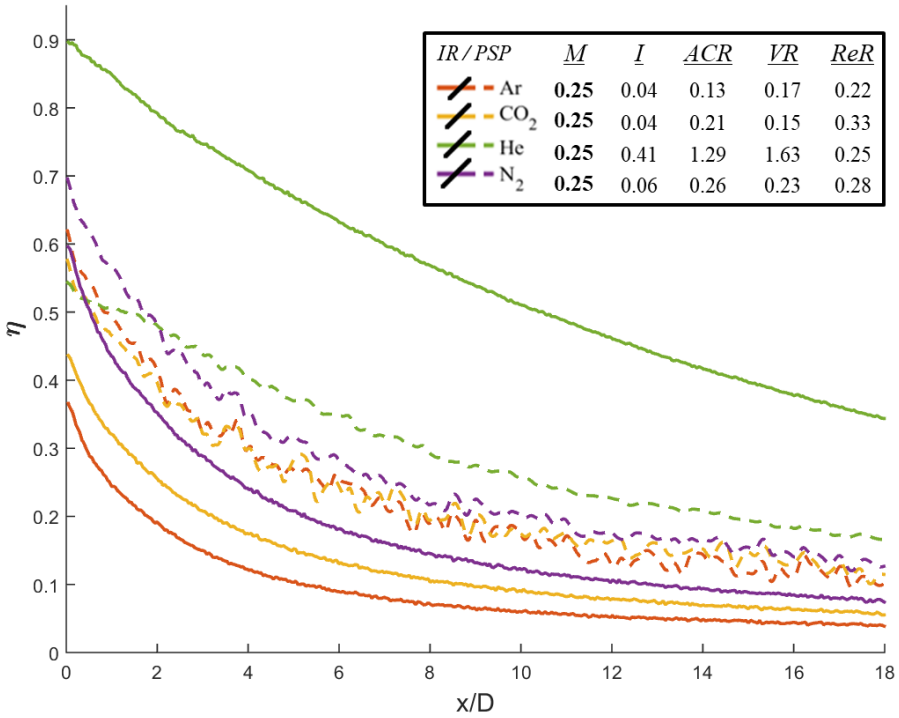

Figure 51: η distributions along y/D = 0 at M = 0.25 with IR and PSP.

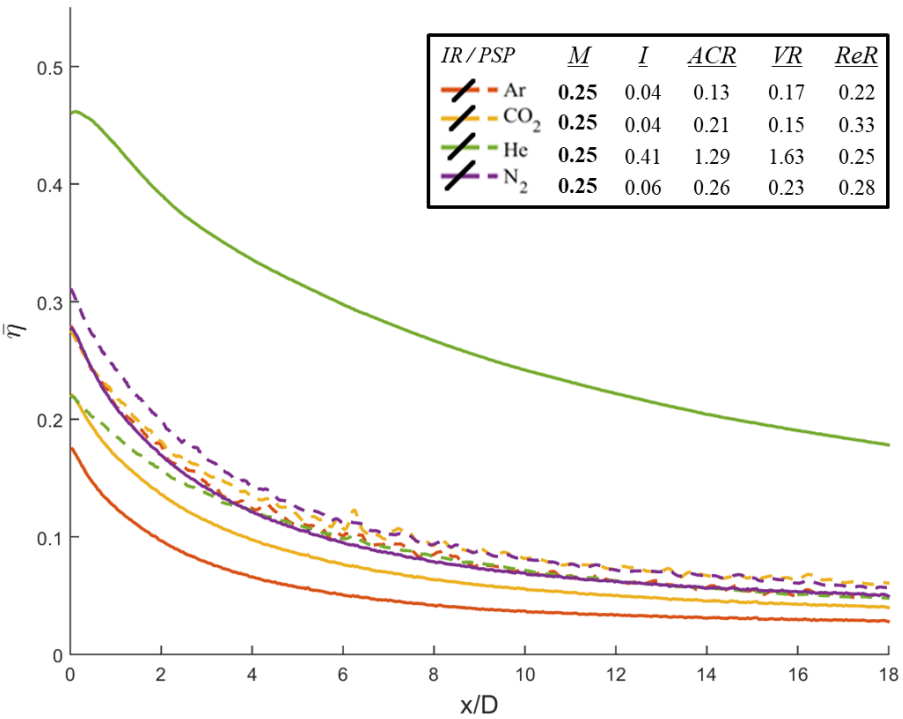

Figure 52: $\bar{\eta}$ distributions averaged over y/D = ±2.5 at M = 0.25 with IR and PSP.

Figure 53 helps to show why the $\bar{\eta}$ plots were able to scale He with the other three gases more effectively than the centerline η plot at M = 0.25. Figure 53 shows the spanwise η plot for both techniques at x/D = 3.0 over y/D ±2.5. Although the peak value of He was greater than Ar, CO_2, and N_2 with PSP, He did not spread as far laterally. One difference between He and the other three gases is that He has a *VR* of only about a factor of 1.6 times greater than unity. However, the *VR* of the other three gases are about 4.3 to 6.7 times less than unity, a much greater factor from unity. It has been reported in literature [4] that *VR* scales the shear layer between the coolant and the freestream. Therefore, the results shown in Figure 53 indicate that Ar, CO_2, and N_2 have a greater strength of a shear layer than He which reveals a further lateral spreading of those coolant gases.

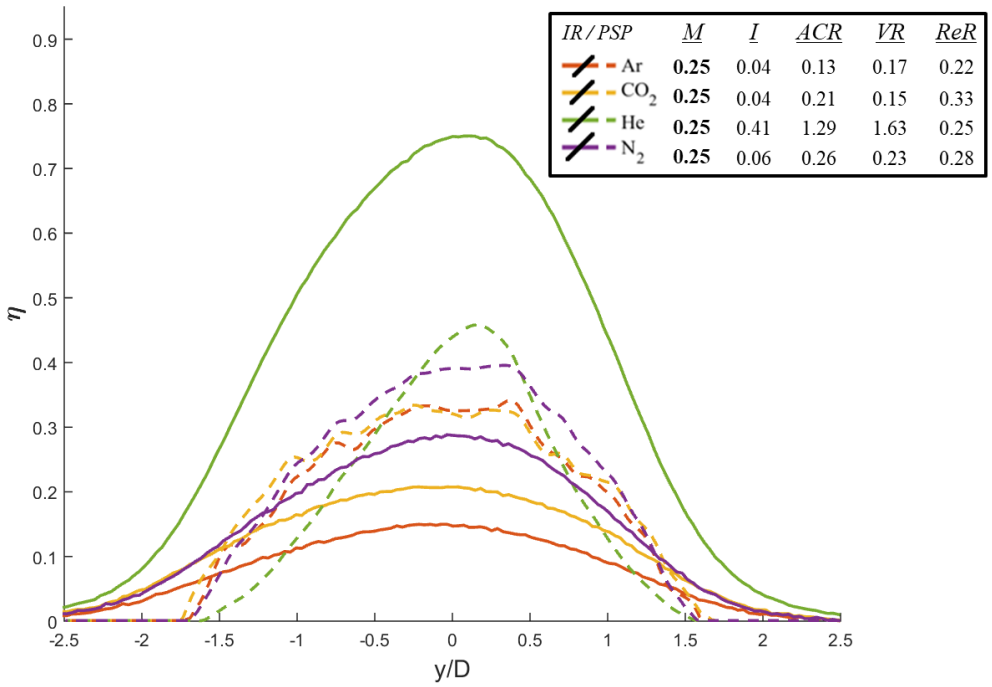

Figure 53: η distributions at x/D = 3.0 over y/D = ±2.5 at M = 0.25 with IR and PSP.

The effects of jet separation began to show when M was matched at higher values. Figure 54 shows the $\bar{\eta}$ plot for matched M = 0.50 using IR and PSP. Jet separation effects were shown by He having a lower $\bar{\eta}$ value than the collapsed grouping of Ar, CO_2, and N_2 with PSP. The value of I for He raised to a value of I = 1.56, beyond the peak value of I = 1.00, whereas the values of I for Ar, CO_2, and N_2 all remained at low values. When M is matched at 1.50, the values of I for every gas are beyond the peak value. Thus, at matched M = 1.50 for centerline η and $\bar{\eta}$, shown in Figure 55 and Figure 56, respectively, the collapsed grouping of Ar, CO_2, and N_2 separate in the same trend that was seen at matched I = 1.50.

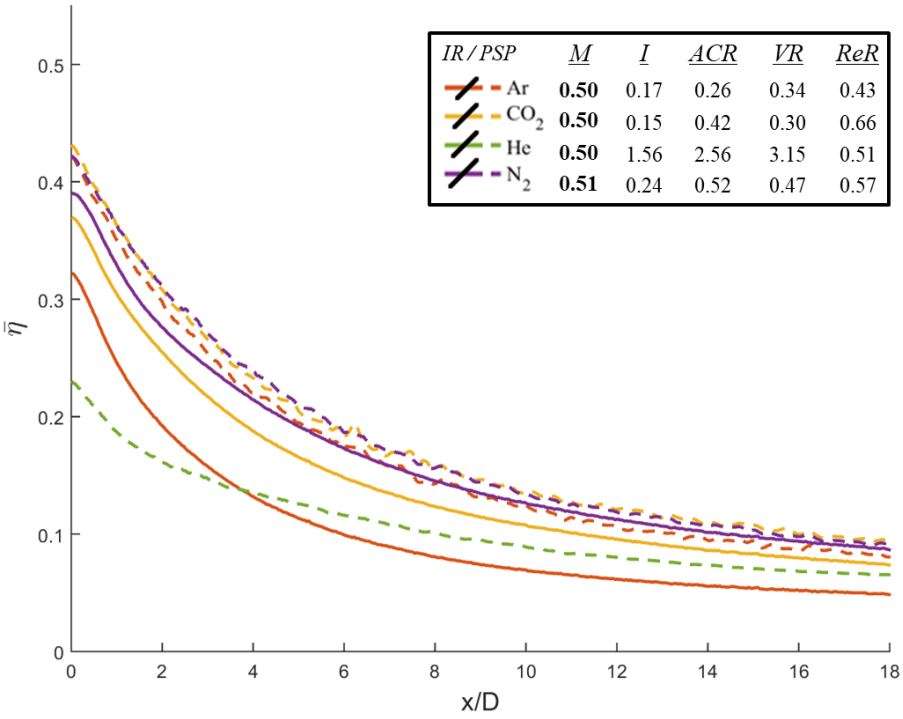

Figure 54: $\bar{\eta}$ distributions averaged over y/D = ±2.5 at M = 0.50 with IR and PSP.

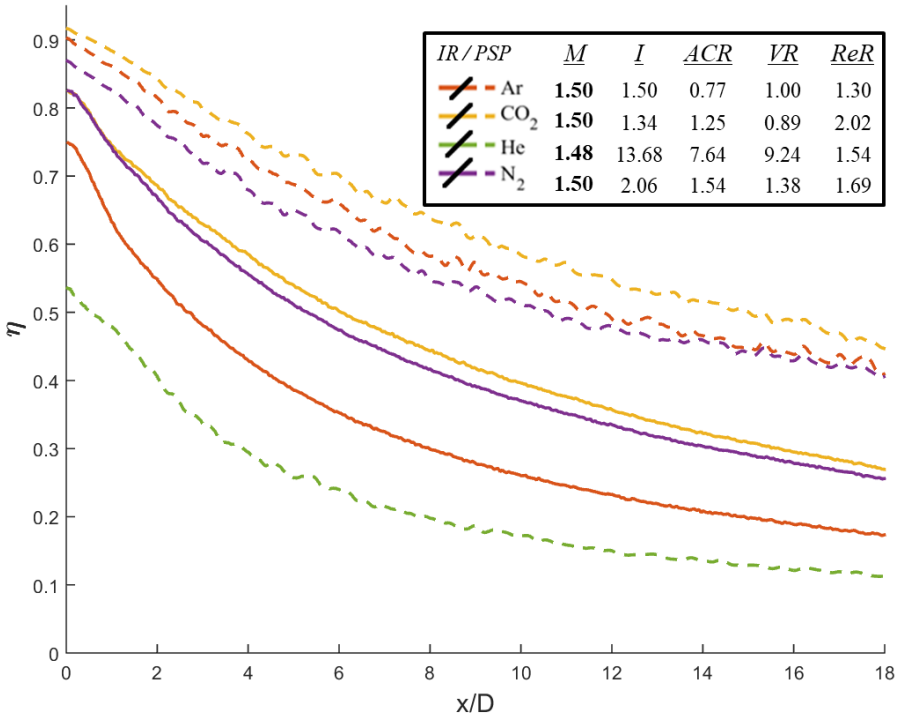

Figure 55: η distributions along y/D = 0 at M = 1.50 with IR and PSP.

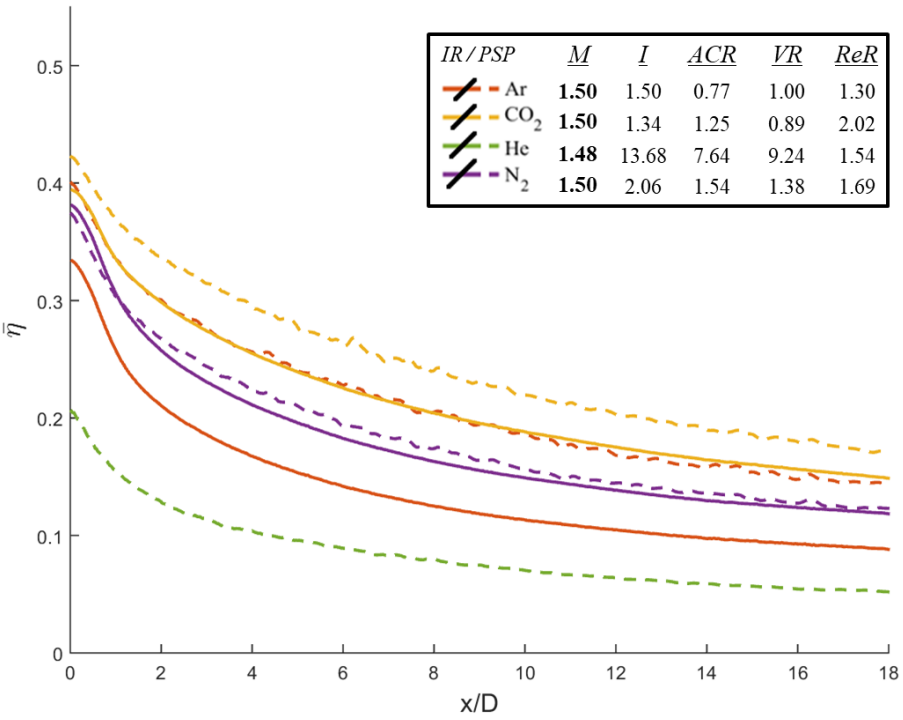

Figure 56: $\bar{\eta}$ distributions averaged over y/D = ±2.5 at M = 1.50 with IR and PSP.

Similar to *ACR* with IR, it was very powerful to analyze and view matched M vs. $\bar{\bar{\eta}}$ with the PSP method, shown in Figure 57. The $\bar{\bar{\eta}}$ values collapse the data into one curve for all four gases and then each gas individually deviates from the general trend. Shown at the location of deviation for each gas is the corresponding I value. The deviation can be attributed to the onset of jet separation for the particular gas. Thus, it was concluded that M is the appropriate parameter to scale adiabatic effectiveness with PSP for cases where the jet remains fully attached to the surface, at values less than $I \approx 0.40$ for the conditions of this study. Note that the higher flow rates for He were acquired for the purpose of obtaining He's deviation point from the general collapsed curve of the matched M vs. $\bar{\bar{\eta}}$ plot with the PSP technique. He had not yet deviated from the general trend with only the low flow rate (below 50 SLPM) data points.

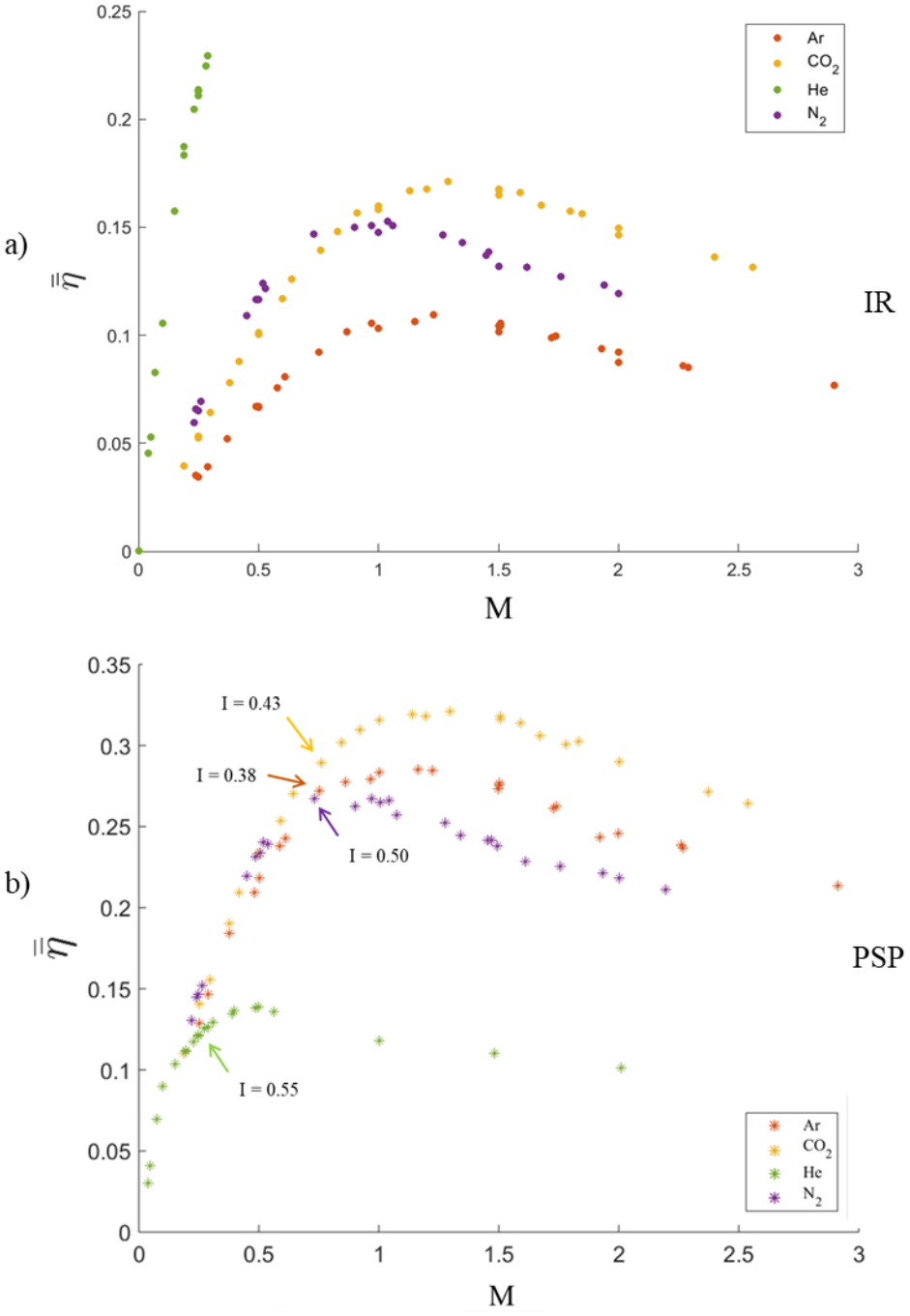

Figure 57: $\overline{\overline{\eta}}$ vs. *M* for all test cases. Deviation points with corresponding *I* values labelled for the PSP data. a) IR and b) PSP.

4.1.4 Reynolds Number Ratio (*ReR*)

ReR was matched next. *ReR* is the first parameter in this study to consider the dynamic viscosity ratio between the coolant and the freestream. *ReR* is equal to *M* divided by the coolant-to-freestream μR, values given in Table 9 for each of the four gases. Figure 58 and Figure 59 show the centerline η plot and $\bar{\eta}$ plot, respectively, at matched *ReR* = 0.25. Although high flow rate He data is not shown for *ReR*, the $\bar{\eta}$ plot at matched *ReR* = 1.50 is shown in Figure 60. With both techniques, it appears that matched *ReR* performs very similarly to matched *M*. It is evident with the IR technique that *ReR* is not an appropriate scaling parameter. However, upon initial inspection of Figure 58, Figure 59, and Figure 60 with the PSP technique, one might initially be inclined to believe that *ReR* scales adiabatic effectiveness nearly just as well as *M* for low values of *ReR*. However, shown in Figure 61, analyzing $\bar{\bar{\eta}}$ vs. *ReR*, it becomes apparent that *ReR* couldn't scale adiabatic effectiveness as well as *M* in Figure 57 analyzing $\bar{\bar{\eta}}$ vs. *M*. This is shown by the wider grouping of the collapsed general trend with *ReR* (Figure 61) as compared to *M* (Figure 57).

It should be noted that the difference in μR from unity is small, from the lowest at 0.75 with CO_2 to the highest at 1.15 with Ar. Therefore, the *ReR* values do not change very much from the *M* values and this makes the adiabatic effectiveness results similar. However, the distribution of the coolant on the surface depends on the mass flux of the coolant being injected into the freestream and does not depend as much on the shear layer interaction between the coolant and the freestream. To test this hypothesis, a gas with a much different dynamic viscosity would need to be used and compared to these four gases. The proposed result would be similar to how *I* = 0.25 was able to scale the PSP data between Ar, CO_2, and N_2 but when He was added to the dataset, with a much higher heat capacity, it was shown that *I* was no longer able to scale the PSP data between all four gases. Evidence to support this hypothesis is that CO_2 appears to be the gas that

deviates furthest from the general trend of collapsed $\bar{\bar{\eta}}$ values with the PSP data in Figure 61, and CO_2 is the gas with μR furthest from unity.

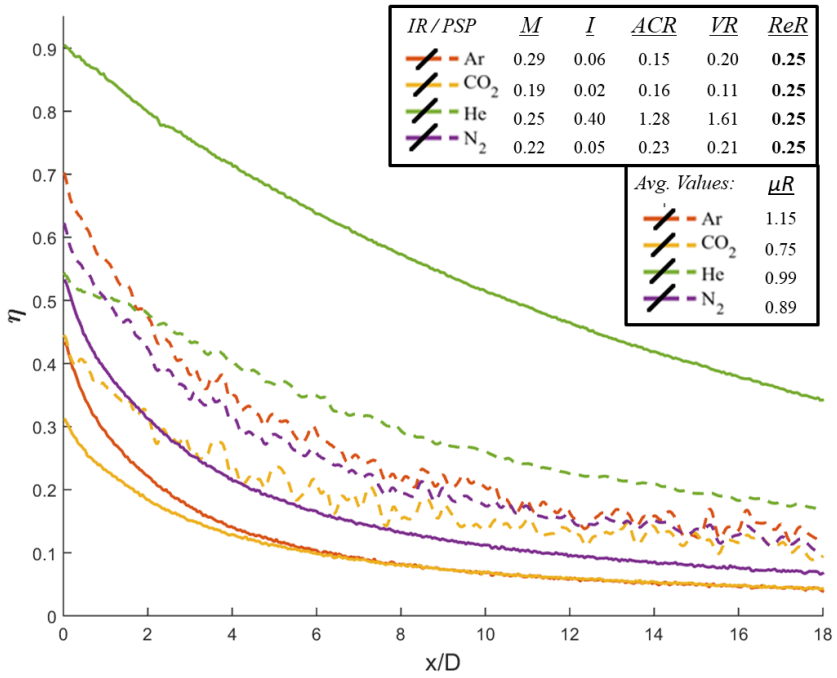

Figure 58: η distributions along y/D = 0 at ReR = 0.25 with IR and PSP.

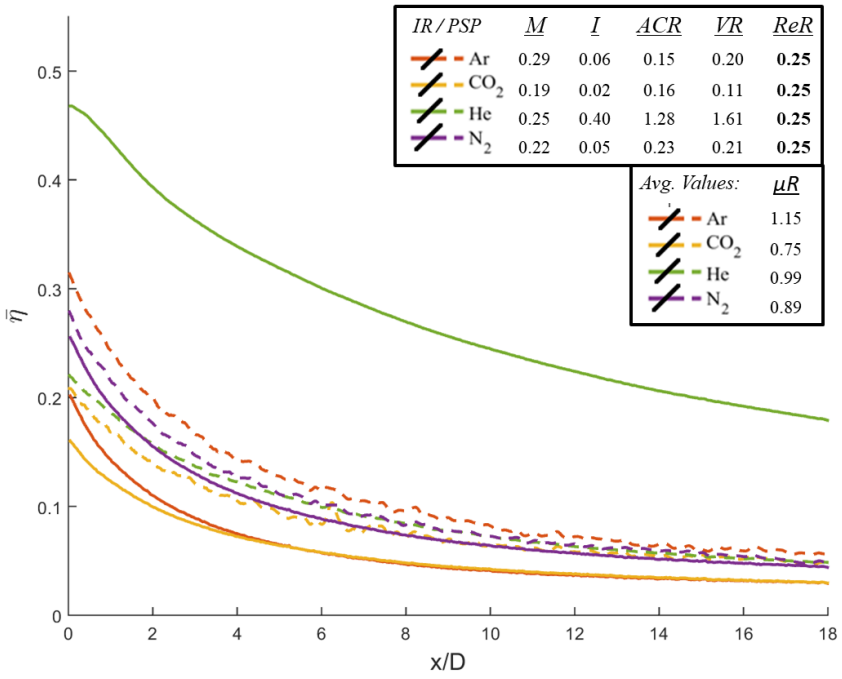

Figure 59: $\bar{\bar{\eta}}$ distributions averaged over y/D = ±2.5 at ReR = 0.25 with IR and PSP.

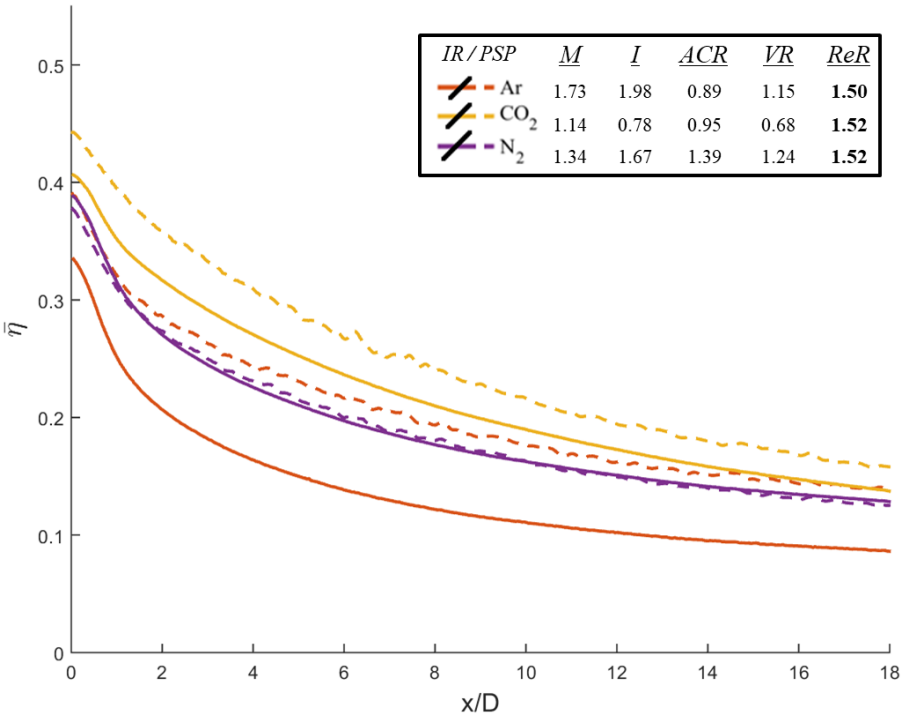

Figure 60: $\bar{\eta}$ distributions averaged over *y/D* = ±2.5 at *ReR* = 1.50 with IR and PSP.

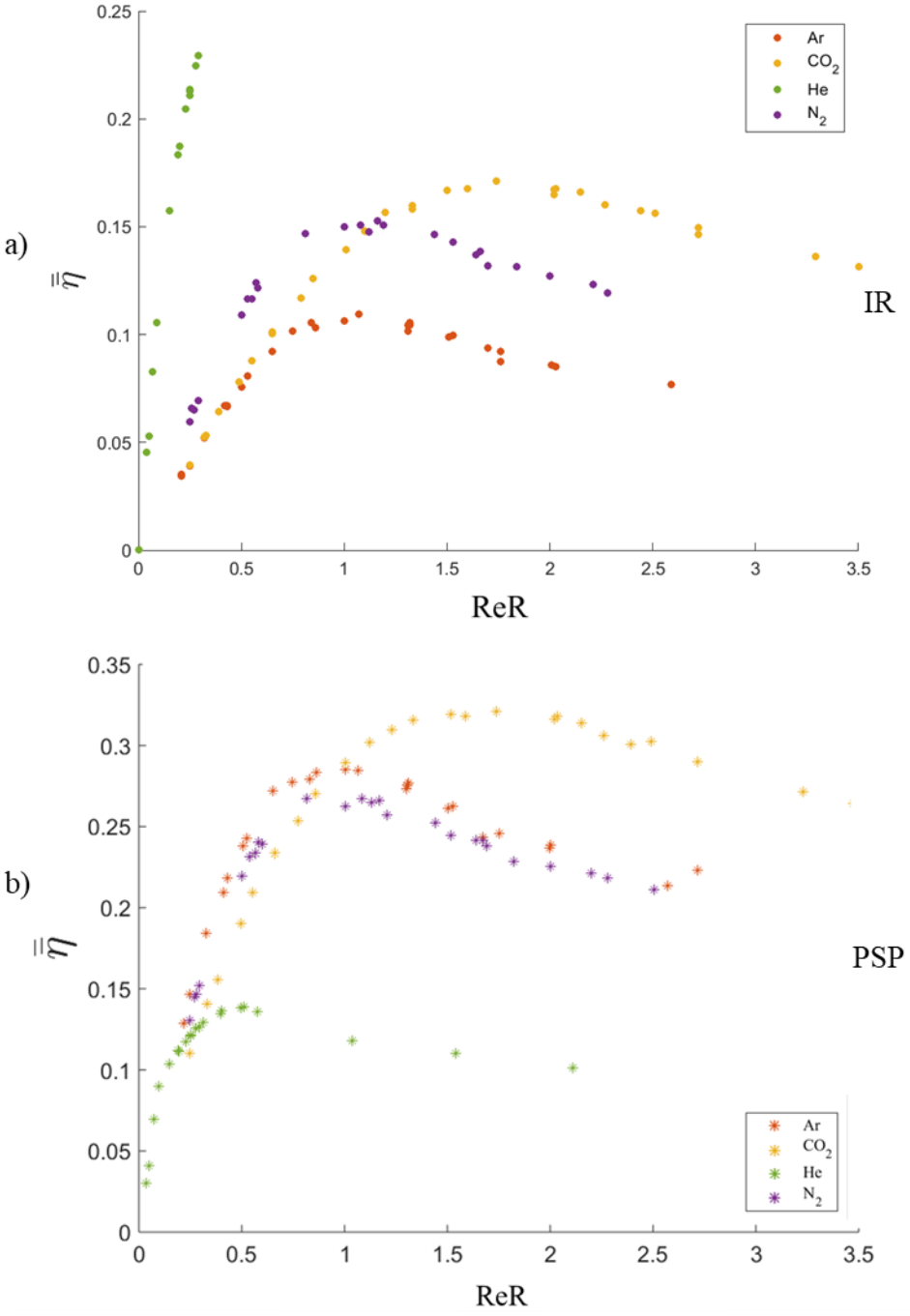

Figure 61: $\overline{\overline{\eta}}$ vs. *ReR* for all test cases. a) IR and b) PSP.

4.1.5 Velocity Ratio (*VR*)

VR was the last coolant flow rate parameter to be analyzed because it only accounts for the velocities of the coolant and the freestream. By not accounting for any gas properties, *VR* allows gas properties to influence the adiabatic effectiveness data when the properties differ. Shown in Figure 62 and Figure 63, at matched *VR* = 0.25 and 1.50, respectively, *VR* is unable to scale η. Figure 64, with a plot of $\bar{\bar{\eta}}$ vs. *VR*, also shows that *VR* is not an appropriate scaling parameter for either IR or PSP. It should be noted though with the PSP data, after separation occurs with Ar, CO_2, and N_2, the gases separate in the same order as high values of matched *I*, *M*, and *ReR* cases. Even though *VR* does not account for *DR*, the highest η is associated with the highest *DR* and the lowest *BDR*. Then as η decreases, the trend of decreasing *DR* and increasing *BDR* follows. Since *VR* does not account for *DR*, as *M* and *I* do, it appears that the ratio of the binary diffusion coefficient may be of importance when experimenting with PSP. A higher *BDR* means that the coolant diffuses molecularly into the freestream more readily than a coolant with a low *BDR*. When a coolant diffuses more readily into the freestream, there is more mixing with the freestream and less coolant on the surface downstream of the coolant injection. Therefore, the presence of the coolant on the surface would be undetected by the PSP which would, in turn, indicate a lower adiabatic effectiveness.

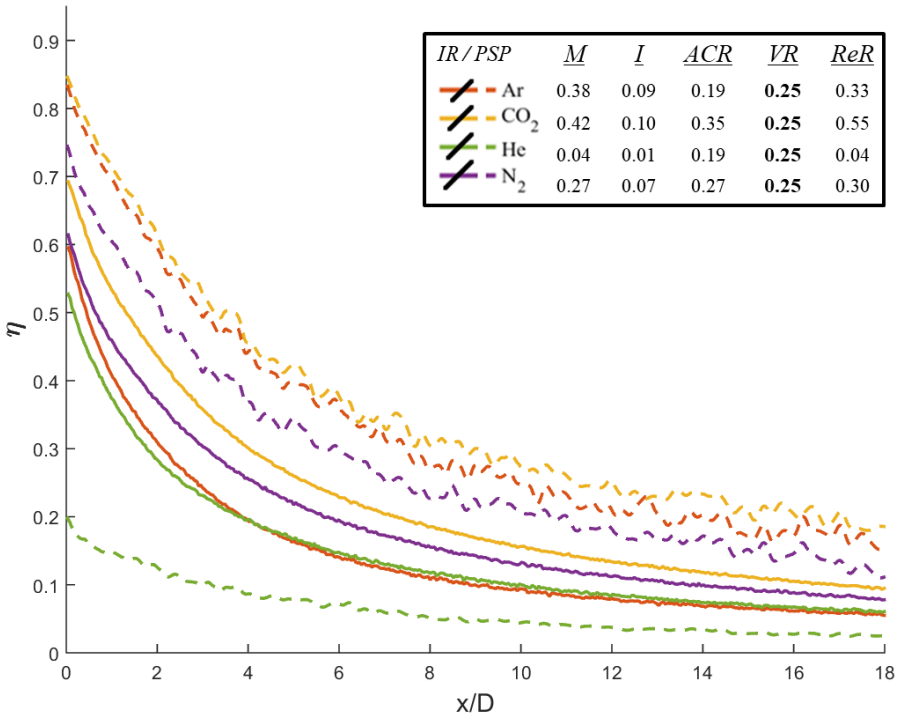

Figure 62: η distributions along y/D = 0 at VR = 0.25 with IR and PSP.

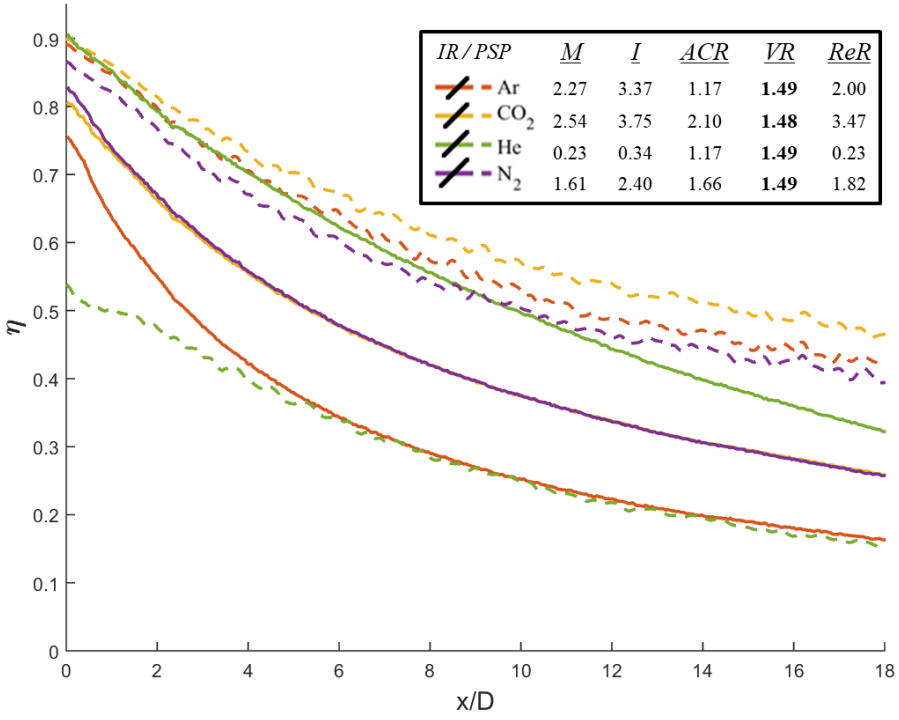

Figure 63: η distributions along y/D = 0 at VR = 1.50 with IR and PSP.

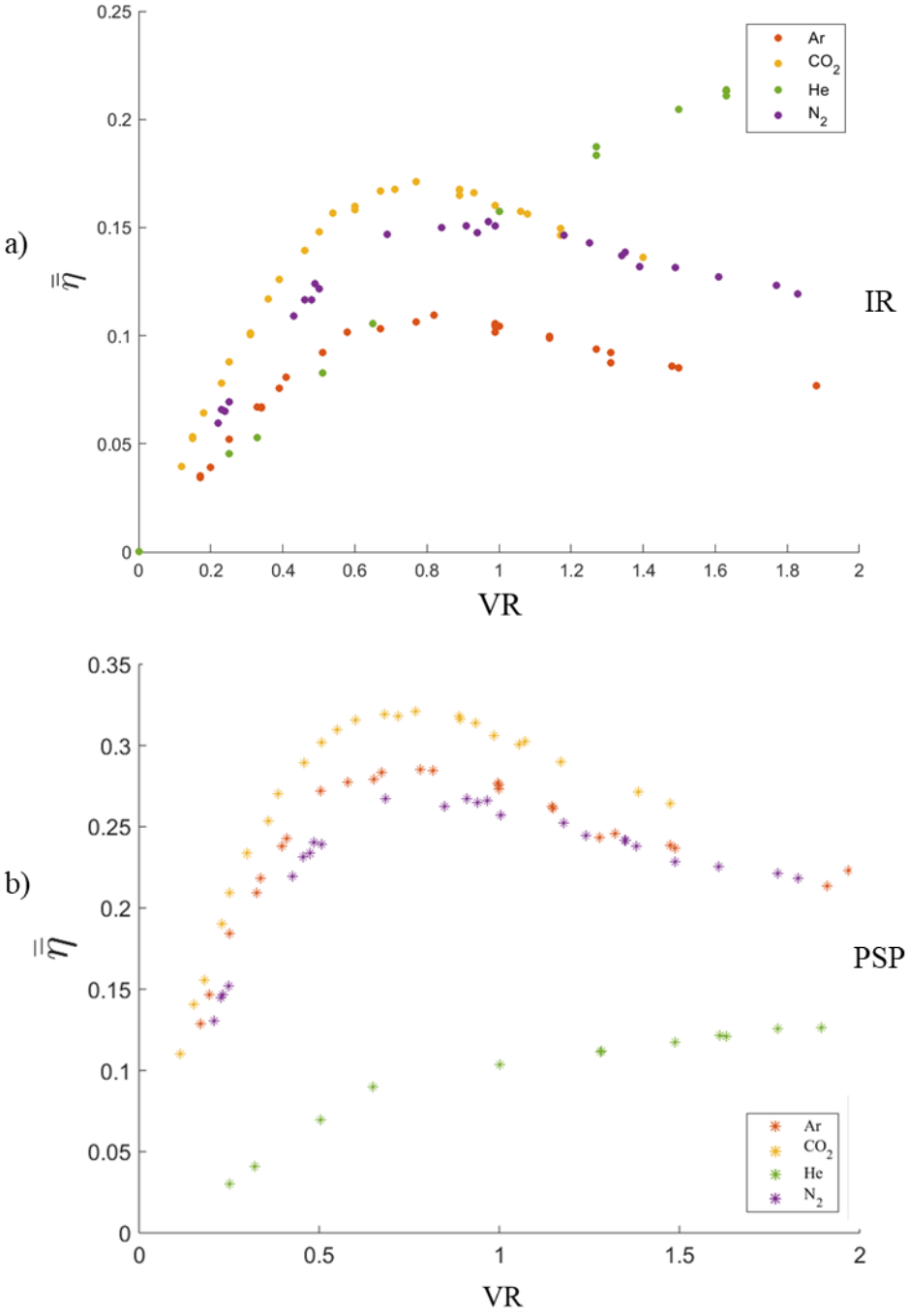

Figure 64: $\bar{\bar{\eta}}$ vs. *VR* for all test cases. a) IR and b) PSP.

4.2 Comparison of IR and PSP Measurement Techniques

The second objective of this study was to compare the pressure sensitive paint measurement technique to the infrared thermography measurement technique. This study was a first of its kind to evaluate both techniques on the exact same model that was painted with PSP for both the thermal and mass transfer techniques: a flat plate with a single zero-degree compound angle coolant injection 7-7-7 hole. This made it so the test and plate conditions were nearly identical between experiments. Another study, like Wiese et al. [3], used the model for the IR method, then painted the model with PSP and used it for the mass transfer method. However, in this study, it was found that painting the model can affect how the flow is distributed on the surface by imperfections on the surface and the model, specifically at the exit of the hole. Painting the surface can also change the roughness of the surface, again affecting how the coolant is distributed on the surface. Johnson et al. [27] applied another method that matched geometries and flow conditions of other studies to compare methods. The authors [27] performed a PSP study and compared the results to thermal studies previously conducted. Therefore, this study was able to directly compare measurement techniques by using the exact same model and the exact same test conditions between IR and PSP measurement techniques.

The first objective of this study was to determine the best coolant flow rate parameter to use scaling adiabatic effectiveness between various gases with the PSP measurement technique. To compare techniques, the same matched values of coolant flow rate parameters were observed with both measurement techniques. In doing so, Section 4.1 accomplished the first objective but also touched on the second objective as the Section does directly compare the two techniques through the sweeps of the coolant flow rate parameters in determining each parameter's efficacy

in scaling adiabatic effectiveness. However, a detailed discussion of other observed differences is in order.

Wiese et al. [3] observed that the PSP measurement technique indicated higher adiabatic effectiveness than the IR thermal measurement technique. The authors' experiment directly compared the PSP measurement technique to the IR measurement technique on a leading edge model with a 90-degree compound angle coolant injection cylindrical hole. The authors used Ar, CO_2, and N_2 as the foreign gases. Johnson et al. [27] took a different approach and compared their PSP measurement technique to an IR measurement technique by which they modelled their flow conditions and geometry [28], a flat plate with cylindrical holes at 30-degree coolant injection angles. The results of Johnson et al. showed that the PSP measurement technique indicated a lower effectiveness than the study they modelled their conditions after. Although, the bounds of the comparison fall within their large bounds of uncertainty, ±0.09 over the entire *x/D*, which proves an inconclusive result. The authors [27] attribute the higher indicated effectiveness using thermal methods to the thermal methods being subject to conduction. However, Wiese et al. [3] ground their results in the physics of the fluid interaction between the coolant and the freestream.

Although the geometries and flow environment were significantly different in Wiese et al. [3], this study also found that PSP indicated a higher adiabatic effectiveness compared directly to IR thermography using foreign gas coolants Ar, CO_2, and N_2. However, the gases used in Wiese et al. [3] produced a dataset with similar fluid property variations, rendering the results incomplete. The current study additionally observed He using both PSP and thermal methods. With the addition of He to the dataset, a gas that has a drastically lower *DR*, but a much higher *CpR*, *BDR*, and *LeR* as compared to Ar, CO_2, and N_2, the PSP measurement technique observed lower adiabatic effectiveness values than were found using the IR technique. This study was the first to find an

exception to the general trend outlined by Wiese et al [3]. The results found in this study, higher observed η with PSP for Ar, CO_2, and N_2 but a lower observed η with He, compared to IR, were consistent for every matched parameter value. This can be readily seen in all figures of centerline η and $\bar{\eta}$ plots, no exceptions were found for this behavior.

The observed difference in the adiabatic effectiveness values between the two measurement techniques can first be explained by physics that govern fluid interactions as well as fundamental differences between the two measurement techniques. The observed findings are in line with the explanation given in Wiese [17], a preceding study to Wiese et al. [3]. Coolant jets experience several different diffusional processes as they enter the freestream: mass, momentum, and thermal diffusion. A fundamental difference between the two techniques is that the PSP technique is not sensitive to the thermal diffusion as the IR technique is. In particle kinetics, thermal diffusion occurs as a particle with a higher thermal energy collides with a particle of lower thermal energy, transferring the energy to the lower thermal energy particle. Thus, through a series of collisions, higher thermal energy from the freestream can make its way to the surface through the lower thermal energy coolant plume.

A particle from the freestream can penetrate through the coolant plume and make its way to the surface. However, a particle is very unlikely to penetrate the coolant plume without any collisions that transfer thermal energy. This is supported by the result of Jennings [36], corroborated with three other studies, that found the mean free path in air to be about 6.6×10^{-8} m. Assuming the thickness of the coolant film is on the order of the coolant hole diameter, about 5.8×10^{-3} m, the mean free path is about 10^5 times smaller than the thickness of the coolant plume. As an O_2 molecule penetrates through the coolant plume to the surface, where it is detected by the PSP, the particle has also transferred thermal energy to the surface and into the boundary layer

fluid, by a domino effect of collisions. Therefore, even the O_2 particles that do reach the surface are not at T_∞ but rather something closer to T_c. Some O_2 particles from the freestream will also transfer thermal energy through the coolant plume affecting the temperature of the surface, without making their way to the surface, an affect that goes undetected by the PSP measurement technique. Not only is the IR technique sensitive to the lateral conduction through the model itself, but it is also sensitive to the thermal diffusion of the freestream gas to the coolant gas. This explanation held true and satisfied the reason why PSP indicated a higher effectiveness than IR for Ar, CO_2, and N_2. Thermal energy was making its way to the surface faster than the O_2 molecules were penetrating to the surface. This was not the case, however, for He. This study was the first to find an exception to the mechanism described by Wiese et al. [3].

Another discussion on the relationship of adiabatic effectiveness magnitudes between thermal measurement techniques and mass transfer techniques can begin with retracing to an assumption that was used to implement the mass transfer analogy. The assumption was that the Lewis number was equal to one to implement the heat-mass transfer analogy to convert adiabatic effectiveness in terms of temperature to that of mass concentrations. This would mean that *LeR* is unity between the coolant and the freestream. However, *LeR* was not unity for any of the four gases. Figure 65 shows centerline η at matched M =0.25 to aid in this discussion. Seen in Figure 65, as Wiese et al. [3] observed, Ar, CO_2, and N_2 indicated a higher η for the mass transfer method compared to the thermal method. This can now be correlated to having a *LeR* less than unity. Then, for He, which indicated a lower η for the mass transfer method compared to the thermal method, *LeR* was greater than unity. Therefore, a coolant with a higher *Le* than the freestream gas will indicate a lower η with a mass transfer method compared to a thermal method and a coolant with a lower *Le* than the freestream gas will indicate a higher η with a mass transfer method compared

to a thermal method. This study was the first to observe the relationship between *LeR* and the difference in η values between mass transfer and thermal methods. There was no exception to this relationship found in this study.

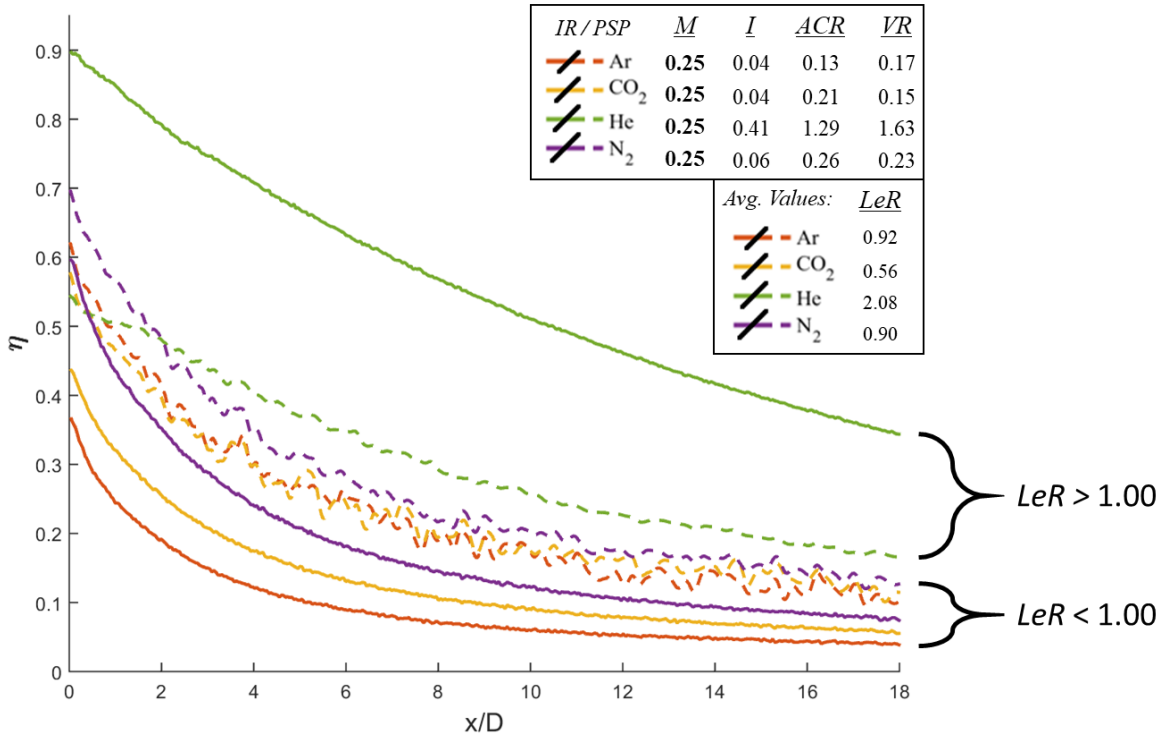

Figure 65: η distributions along *y/D* = 0 at *M* = 0.25 with IR and PSP, *LeR* shown to describe differences in η magnitudes between techniques.

Now, considering only the mass transfer relations, Ar, CO_2, and N_2 have *BDR*s of 0.95, 0.81, and 1.00, respectively. Therefore, the binary diffusion of the coolant gases is either equal to, or less than unity. However, He has a *BDR* of 3.47, so He has a much higher binary diffusion coefficient than unity. A *BDR* less than one would indicate that the coolant is resisting diffusion into the freestream air. Whereas He, with a high *BDR*, readily diffuses into the freestream air and allows the diffusion of air through the coolant plume. Thus, in the order of lowest *BDR* to highest *BDR*, the gases should be ordered as highest effectiveness to lowest effectiveness, in terms of mass

concentrations with the PSP technique. The order of lowest *BDR* to highest *BDR* is CO_2, Ar, N_2, then He. The data shows that as soon as there was jet separation, this was the case, no matter the coolant flow rate parameter, evident in Figure 45, Figure 49, Figure 55, Figure 56, Figure 60, and Figure 63. Figure 56 data is shown here again in Figure 66 but with the IR data removed and the values of *BDR* for each gas labelled. The only discrepancy was in Figure 45 for matched *ACR* = 1.50 where Ar and N_2 are closely grouped together with N_2 having a slightly higher effectiveness than Ar further downstream. However, these values are within the bounds of uncertainty. The observation of the relationship between *BDR* and the magnitude of effectiveness holds for jets that are past the critical flow rate where separation occurs, $I = 1.00$, for the conditions of this study. It does not hold for jets that remain fully attached to the surface, for example: Figure 43, Figure 47, Figure 51, Figure 58, and Figure 62.

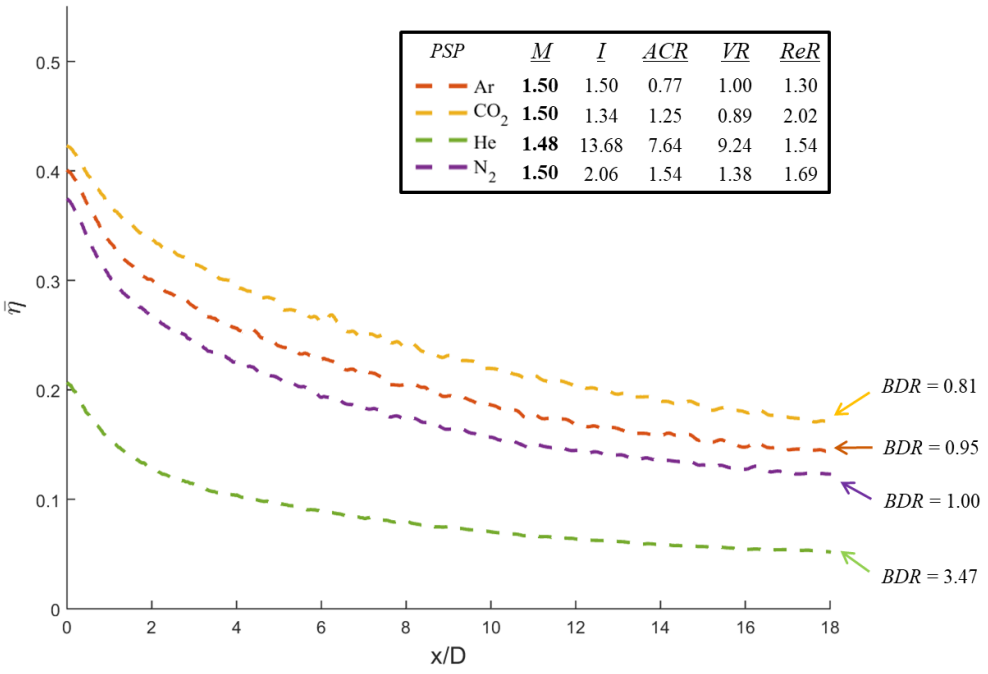

Figure 66: $\bar{\eta}$ distributions averaged over *y/D* = ±2.5 at *M* = 1.50 with PSP and *BDR*s labelled.

The preceding discussion can also help explain another difference seen between IR and PSP measurement techniques. The difference can be visualized in Figure 67 and Figure 68, spanwise adiabatic effectiveness plots at matched *ACR* = 0.25 and *M* = 0.25, respectively at *x/D* = 3.0 over *y/D* ±2.5. These plots are shown as they are the two cases that collapse centerline η most effectively for IR with matched *ACR* and PSP with matched *M*. In both Figure 67 and Figure 68, the IR method shows a greater lateral spreading and a lower $\frac{\partial \eta}{\partial y}$ than the PSP method, an observation that was also seen by Wiese et al. [3]. This can be explained by the IR method's sensitivity to thermal diffusion and conduction in the fluid, and lateral conduction through the test model, where PSP was not sensitive to these thermal effects.

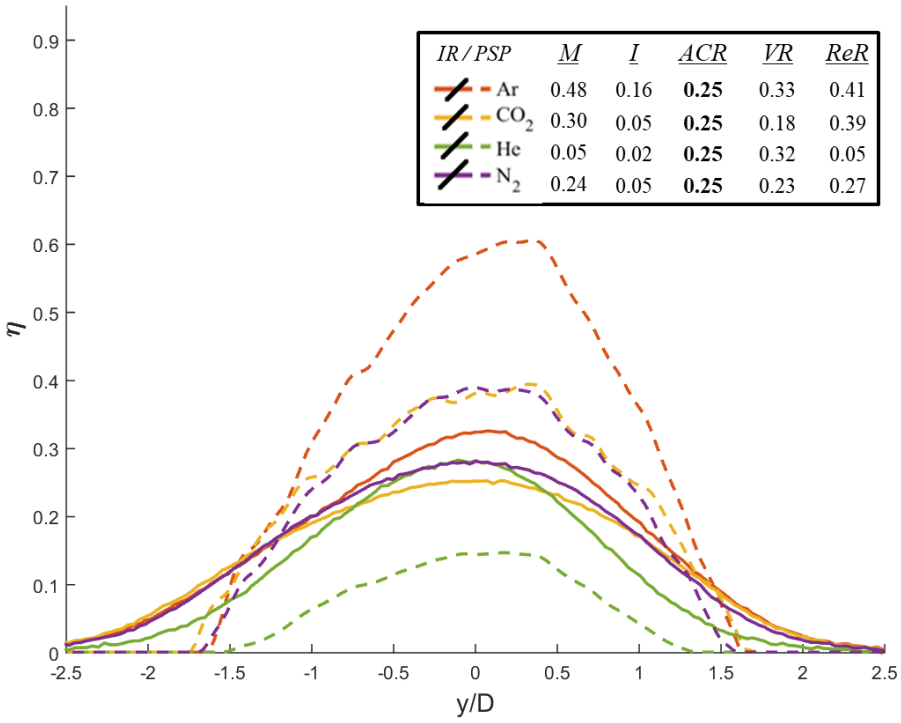

Figure 67: η distributions at *x/D* = 3.0 over *y/D* = ±2.5 at *ACR* = 0.25 with IR and PSP.

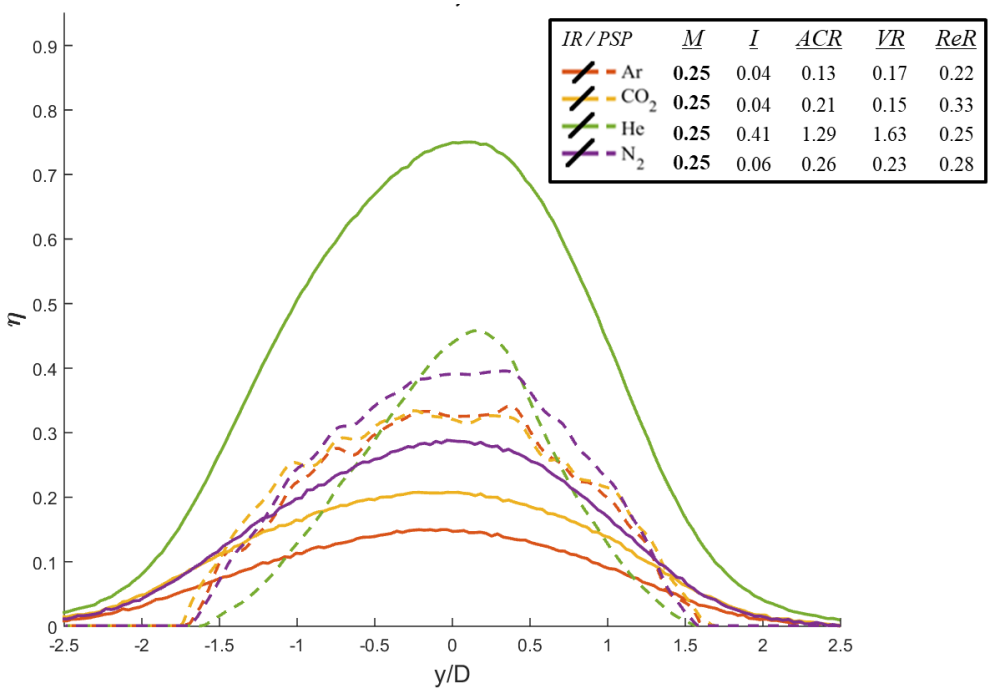

Figure 68: η distributions at x/D = 3.0 over y/D = ±2.5 at M = 0.25 with IR and PSP.

Furthermore, most clearly evident in Figure 42 and Figure 50 for the contour plots of ACR = 0.25 and M = 0.25, respectively, the PSP results exhibited more noise than the IR results. This was also evident in the η and $\bar{\eta}$ plots where the results are shown as smoother curves for the IR data compared to the PSP data. The turbulent mixing from the interaction of the coolant with the freestream can help explain the high level of noise seen in the PSP results. The turbulent fluctuations rapidly affect the concentrations of gas particles on the surface of the plate. As previously stated, the response time of the PSP to pressure change is 300 ms, much slower than the rapid fluctuations of the concentration of O_2 on the surface. The experimental technique using PSP, as described in Section 3.4.3, takes several snapshots, or frames, then averages them to determine the concentration of O_2 on the surface. However, increasing the number of frames averaged past 30 frames did little to reduce the noise shown in the PSP results. On the other hand, with the IR technique, the change in surface temperature is damped with time because the test

model has a nonzero thermal conductivity. Therefore, the temperature remains more constant and thus, the IR results show less noise than the PSP technique.

4.3 Nonzero Adiabatic Effectiveness Upstream of the Cooling Hole

Although not an objective of this study, another phenomenon was observed and is worth noting, nonzero adiabatic effectiveness upstream of the cooling hole. It was seen that there was an observed nonzero adiabatic effectiveness upstream of the hole with the IR measurement technique. This upstream nonzero η with a thermal technique can be attributed to an imperfect conduction correction. There can also be cases where η is perceived as nonzero upstream of the cooling hole due to imperfect conduction corrections. The material of many models is thin immediately upstream of the coolant hole where the coolant hole injection is angled through the model. Conduction occurs from the coolant through the model which can be observed by an IR camera. For this reason, the region immediately upstream of the coolant hole is usually ignored in thermal studies. There is also lateral conduction through the model that could explain the effectiveness seen around the cooling hole. This observed η can be seen in the zoomed in IR contours of Figure 69. However, using the PSP measurement technique, upstream η was also observed. The PSP technique only indicates nonzero η where there is a presence of the coolant on the surface. This implies that there was coolant on the surface upstream of the cooling hole and that there was a nonzero adiabatic effectiveness upstream. This can be attributed to coolant being entrained in a vortical structure as the freestream interacts with the coolant.

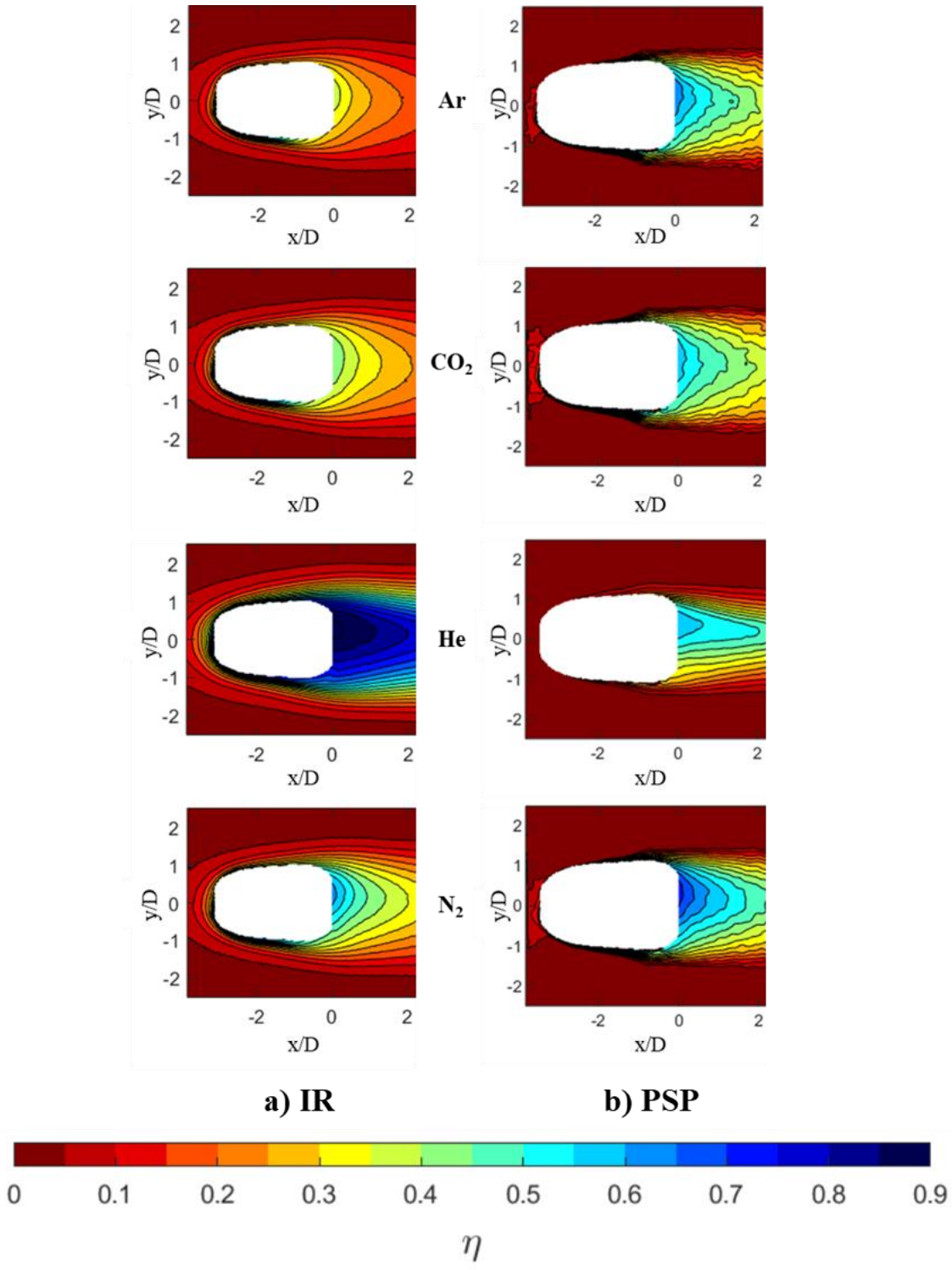

Figure 69: Nonzero upstream η shown at matched M = 0.25. a) IR and b) PSP.

5. Conclusion

The first objective of this research was to determine the best coolant flow rate parameter to use in low temperature PSP experiments to scale adiabatic effectiveness between gases with property variations. To accomplish this objective, five coolant flow rate parameters (*ACR*, *I*, *M*, *ReR*, and *VR*) were used with four different foreign gases (Ar, CO_2, He, and N_2) and the parameters were each matched at five different values (0.25, 0.50, 1.00, 1.50, and 2.00). The dataset offered a wide range of results with large variations in gas properties to determine the efficacy of each coolant flow rate parameters' scaling ability. A previous study was accomplished with the same model geometry in this study using an IR experimental technique. Therefore, the second objective of this study was to repeat the previous IR experiment to match the conditions of the PSP experiment in this study which resulted in a direct comparison between the two techniques.

5.1 New Data Collection Method for Large Datasets with PSP

Although not an objective of this study, a new method to collect large datasets with pressure sensitive paints was developed. The accepted standard method for testing with PSPs required reference images to be taken for each data point collected. If there was a large dataset, this not only increased the time it took to conduct a test, but it also decreased the life of the PSP on the model from prolonged exposure to the excitation light. The new method developed in this study utilizes reference images taken before and after the dataset with an interpolation of the data points between the reference images to account for paint degradation. The method produced repeatable results while decreasing the exposure time of the PSP to the excitation light, increasing the life of the paint.

5.2 Scaling Conclusions

The large dataset in this study offered comprehensive results for determining the best coolant flow rate parameter to use scaling adiabatic effectiveness between various gas properties with a pressure sensitive paint measurement technique. The first parameter studied, *ACR*, was not able to scale adiabatic effectiveness with PSP. This made sense because of the insensitivity of the PSP to thermal effects. Therefore, the consideration of specific heats with *ACR* accounted for the cooling capabilities of the coolant while using the IR thermal experimental method and made for a great scaling parameter. The consideration of *CpR* added a variable that goes undetected with the PSP technique making *ACR* an inappropriate scaling parameter with PSP. Next, it was confirmed that *I* was able to predict jet separation with the PSP technique and values of peak $\bar{\bar{\eta}}$ occurred at about $I = 1.00$ for both techniques. To complete the first objective, this study found that *M* was able to scale adiabatic effectiveness results using the PSP technique for *I* values less than about 0.4 on flat plate geometry, with a 7-7-7 hole at a zero-degree compound angle injection. Laterally averaging the adiabatic effectiveness just outside the coolant plume proved to scale adiabatic effectiveness the best with the PSP technique. Although *M* performed well using the PSP technique, it does fall short of the scaling abilities of *ACR* with the thermal measurement technique as *ACR* offers a larger range of *I* values and thus, a larger range of flow rates.

5.3 IR and PSP Technique Comparison Conclusions

When comparing thermal methods and mass transfer methods directly, the PSP technique indicated a higher adiabatic effectiveness than the IR technique with Ar, CO_2, and N_2, but indicated a lower adiabatic effectiveness with He. One relationship to the magnitude of effectiveness differences between experimental techniques found in this study was the Lewis number ratio. Mass

transfer methods indicate a higher effectiveness than thermal methods for coolants with *LeR*s less than unity and indicate a lower effectiveness than thermal methods for coolants with a *LeR* greater than unity. The PSP technique also indicated a greater $\frac{\partial \eta}{\partial y}$ than the IR method and in turn, resulted in less spanwise spreading of adiabatic effectiveness than the IR technique. As nonzero adiabatic effectiveness around and upstream of the coolant hole with thermal measurement techniques has been attributed to imperfect conduction corrections, the PSP technique indicates that is not entirely true. The PSP measurement technique indicated that there is coolant distributed on the surface upstream of coolant injection.

Possibly the most important aspect of this research was to determine how mass transfer experimental techniques compares to thermal measurement techniques in their ability to scale adiabatic effectiveness results to be able to predict results at engine conditions, specifically at engine temperatures. The PSP measurement technique showed the ability to scale η between different gases with matched *M*. This proves that there is a limitation with mass transfer methods because of their inability to capture thermal relations. This is why thermal measurement techniques have a greater efficacy to predict results at engine temperatures, specifically scaling adiabatic effectiveness to predict an engine's adiabatic wall temperature. This study found no definitive way to use a PSP to predict thermal conditions, like IR does with *ACR*. PSPs do, however, offer a method to compare film cooling schemes by showing the distribution of the coolant on the surface.

5.4 Significance of Research

This researched proved conditions where *M* was able to almost exactly scale adiabatic effectiveness between different gases using the pressure sensitive paint measurement technique. Until the recent findings of *ACR*s scaling abilities, researchers were looking for ways to account for the density ratio using thermal techniques to scale η with *M*, *I*, and *VR*. When the specific heats are accounted for using a thermal measurement technique, there is no need to match the density ratio because *ACR* scales η. When the thermal influences are removed from the results using a mass transfer technique with a PSP, *M* is the appropriate scaling parameter to use with attached coolant flows for collapsing η data. That is not to say that PSP mass transfer methods should be used in lieu of IR thermal techniques since PSP mass transfer methods are not able to account for thermal effects and cannot be used to predict engine temperatures like thermal methods can by matching *ACR*. The PSP measurement technique can be used to determine the location of the coolant on the surface, which can be used to compare different film cooling schemes.

Finally, the significance of these results can give engine designers insight on how mass transfer measurements compare to thermal measurements. Also, with a greater understanding of how matched coolant flow rate parameters scale adiabatic effectiveness, along with the differences between the experimental methods, engine designers can improve their testing techniques. In turn, this can ultimately improve the performance and life of turbine components in gas turbine engines.

References

1. Rezazadeh, R. M., Alizadeh, A. M., Fathi, A., and Khaledi, H., 2013, "Turbine Blade Temperature Calculation and Life Estimation – A Sensitivity Analysis," *Propulsion and Power Research,* **2**(2), pp. 148-161.
2. Fischer, J. P., 2018, "Influence of Coolant Flow Rate Parameters in Scaling Gas Turbine Cooling Effectiveness on a Flat Plate," Master's Thesis, Air Force Institute of Technology.
3. Wiese, C. J., Rutledge, J. L., and Polanka, M. D., 2018, "Experimental Evaluation of Thermal and Mass Transfer Techniques to Measure Adiabatic Effectiveness with Various Coolant to Freestream Property Ratios," *J. Turbomach*., **140**(February) pp. 1-9.
4. Bogard, D. G., and Thole, K. A., 2006, "Gas Turbine Film Cooling," *J. Propulsion and Power,* **22**(2), pp. 249-270.
5. Sinha, A. K., Bogard, D. G., and Crawford, M. E., 1991, "Film-Cooling Effectiveness Downstream of a Single Row of Holes with Variable Density Ratio," *J. Turbomach.,* **113**(July), pp. 442-449.
6. Ekkad, S. V., Han, J.-C., and Du, H., 1998, "Detailed Film Cooling Measurements on a Cylindrical Leading Edge Model: Effect of Free-Stream Turbulence and Coolant Density," *J. Turbomach*., **120**(4), pp. 799-807.
7. Wright, L. M., Gao, Z., Varvel, T. A., and Han, J.-C., 2005, "Assessment of Steady State PSP, TSP, and IR Measurement Techniques for Flat Plate Film Cooling," *Proceedings of ASME summer Heat Transfer Conference*, HT2005-72363.
8. Han, J.-C., and Rallabandi, A. P., 2010, "Turbine Blade Film Cooling Using PSP Technique," *Frontiers in Heat and Mass Transfer,* **1**(1), pp. 1-21.

9. Pederson, D. R., Eckert, E. R. G., and Goldstein, R. J., 1977, "Film Cooling With Large Density Differences Between the Mainstream and the Secondary Fluid Measured by the Heat-Mass Transfer Analogy," *J. Heat Transfer*, **99**(4), pp. 620-627.
10. Goldstein, R. J., and Cho, H. H., 1995, "A Review of Mass Transfer Measurements Using Naphthalene Sublimation," *Exp. Therm. And Fluid Sci.*, **10**(4), pp. 416-434.
11. Williams, R. P., Dyson, T. E., Bogard, D. G., and Bradshaw, S. D., 2013, "Sensitivity of the Overall Effectiveness to Film Cooling and Internal Cooling on a Turbine Vane Suction Side," *J. Turbomach.*, **3**(136), pp. 1-7.
12. Baldauf, S., Schulz, A., and Wittig, 2001, "High-Resolution Measurements of Local Heat Transfer Coefficients from Discrete Hole Film Cooling," *J. Turbomach.*, **123**(4), pp. 758-765.
13. Kays, W., Crawford, M., and Wiegand, B., 2004, *Convective Heat and Mass Transfer*, 4th ed. McGraw-Hill.
14. Eckert, E. R. G., Sakamoto, H., and Simon, T. W., 2001, "The Heat/Mass Transfer Analogy Factor, Nu/Sh, for Boundary Layers on Turbine Blade Profiles," *Int. J. Heat Mass Transf.*, **44**(6), pp. 1223-1233.
15. Innovative Scientific Solutions, Inc., "Pressure-Sensitive Paint," www.psp-tsp.com, March, 2018.
16. Crafton, J. and Fonov, S., 2013, "Development of Pressure-Sensitive Paint Systems for Low Speed Flows and Large Wind Tunnels," *51st AIAA Aerospace Sci. Meeting*, AIAA, Dallas, TX.
17. Wiese, C. J., 2016, "Influence of Coolant Flow Rate Parameters in Scaling Gas Turbine Cooling Effectiveness," Master's Thesis, Air Force Institute of Technology.

18. Innovative Scientific Solutions, Inc., “Binary Pressure-Sensitive Paint,” www.psp-tsp.com, March, 2018.

19. Gritsch, M., Schulz, A., and Wittig, S., 1998, “Adiabatic Wall Effectiveness Measurements of Film-Cooling Holes with Expanded Exits,” *J. Turbomach.*, **120**(July), pp. 549-556.

20. Schroeder, R. P., and Thole, K. A., 2014, “Adiabatic Effectiveness Measurements for a Baseline Shaped Film Cooling Hole,” *ASME Turbo Expo 2014*, GT2014-25992.

21. Kadotani, K., and Goldstein, R. J., 1979, “On the Nature of Jets Entering a Turbulent Flow Part B- Film Cooling Performance,” *J. Engineering for Power*, **101**, pp. 466-470.

22. Rutledge, J. L., and Polanka, M. D., 2014, “CFD Evaluations of Unconventional Film Cooling Scaling Parameters on a Simulated Turbine Blade Leading Edge,” *J. Turbomach.*, **13**(October), pp. 1-9.

23. Rutledge, J. L., Polanka, M. D., and Greiner, N. J., 2017, “Computational Fluid Dynamics Evaluations of Film Cooling Flow Scaling Between Engine and Experimental Conditions,” *J. Turbomach.*, **139**(February), pp. 1-7.

24. Eberly, M. K., and Thole, K. A., 2014, “Time-Resolved Film-Cooling Flows at High and Low Density Ratios,” *J. Turbomach.*, **136**(June), pp. 1-11.

25. Greiner, N. J., Polanka, M. D., and Rutledge, J. L., 2015, “Scaling of Film Cooling Performance from Ambient to Engine Temperatures,” *J. Turbomach.*, **137**(July), pp. 1-11.

26. Incropera, F. P., DeWitt, D. P., Bergman, T. L., and LaVine, A. S., 2007, *Fundamentals of Heat and Mass Transfer*. John Wiley and Sons, Inc..

27. Johnson, B., Tian, W., Zhang, K., and Hu, H., 2014, "An Experimental Study of Density Ratio Effects on the Film Cooling Injection from Discrete Holes by Using PIV and PSP Techniques," *Int. J. Heat Mass Transf.*, vol. 76, pp. 337-349.

28. Baldauf, S., Schulz, A., and Wittig, 2001, "High-Resolution Measurements of Local Effectiveness from Discrete Hole Film Cooling," *J. Turbomach.*, **123**(4), pp. 749-757.

29. Fischer, J. P., Rutledge, J. L., Polanka, M. D., and McNamara, L. J., 2019, "Scaling Flat Plate, Low Temperature Adiabatic Effectiveness Results Using the Advective Capacity Ratio," *ASME Turbo Expo 2019*, Paper No. GT2019-90997.

30. Rutledge, J. L., 2009, "Pulsed Film Cooling on a Turbine Blade Leading Edge," PhD Dissertation, Air Force Institute of Technology.

31. Touloukian, Y. S., Saxena, S. C., and Hestermans, P., 1970, *Thermophysical Properties of Matter*, **11**: *Viscosity. Nonmetallic Gases and Liquids*, IFI/Plenum, New York.

32. Touloukian, Y. S. and Makita, 1970, *Thermophysical Properties of Matter*, **6**: *Specific Heat. Nonmetallic Gases and Liquids*, IFI/Plenum, New York.

33. Touloukian, Y. S., Liley, P. E., and Saxena, S. C., 1970, *Thermophysical Properties of Matter*, **3**: *Thermal Conductivity. Nonmetallic Gases and Liquids*, IFI/Plenum, New York.

34. Innovative Scientific Solutions, Inc., "BinaryFIB Pressure Sensitive Paint," www.psp-tsp.com, March, 2018.

35. Kline, S. J., and McClintock, F. A., 1953, "Describing Uncertainties in Single-Sample Experiments," *Mech. Engineering*, **75**(1), pp. 1-8.

36. Jennings, S. G., 1988, "The Mean Free Path of Air," *J. Aerosol Sci.*, **19**(2), pp. 159-166.

REPORT DOCUMENTATION PAGE

Form Approved
OMB No. 074-0188

1. REPORT DATE *(DD-MM-YYYY)*	2. REPORT TYPE	3. DATES COVERED *(From – To)*
21-03-2019	Master's Thesis	January 2018 – March 2019

TITLE AND SUBTITLE

Scaling Film Cooling Adiabatic Effectiveness with Mass Transfer and Thermal Experimental Techniques

5a. CONTRACT NUMBER

5b. GRANT NUMBER

5c. PROGRAM ELEMENT NUMBER

6. AUTHOR(S)

McNamara, Luke J., Captain, USAF

5d. PROJECT NUMBER

5e. TASK NUMBER

5f. WORK UNIT NUMBER

7. PERFORMING ORGANIZATION NAMES(S) AND ADDRESS(S)
Air Force Institute of Technology
Graduate School of Engineering and Management (AFIT/ENY)
2950 Hobson Way, Building 640
WPAFB OH 45433-8865

8. PERFORMING ORGANIZATION REPORT NUMBER

AFIT-ENY-MS-19-M-233

9. SPONSORING/MONITORING AGENCY NAME(S) AND ADDRESS(ES)
Air Force Research Lab, Turbine Engine Division, Turbomachinery Branch
Dr. Andrew T. Lethander
1950 5th St
Wright Patterson AFB, OH 45433
(937) 255-6779
andrew.lethander@us.af.mil

10. SPONSOR/MONITOR'S ACRONYM(S)
AFRL/RQTT

11. SPONSOR/MONITOR'S REPORT NUMBER(S)

12. DISTRIBUTION/AVAILABILITY STATEMENT
DISTRUBTION STATEMENT A. APPROVED FOR PUBLIC RELEASE; DISTRIBUTION UNLIMITED.

13. SUPPLEMENTARY NOTES
This material is declared a work of the U.S. Government and is not subject to copyright protection in the United States.

14. ABSTRACT
With increasing engine temperatures, it is becoming more important to design effective film cooling schemes. Low temperature, large scale tests are often implemented in the design process to reduce cost and complexity. A nondimensional adiabatic effectiveness can be used as an indication of the performance of a film cooling scheme. However, the coolant flow rate must be properly scaled between the low temperature tests and engine temperatures to accurately predict film cooling effectiveness. This process is complicated by gas property variation with temperature. Tests are commonly conducted using thermal measurement techniques with infrared thermography (IR), but the use of pressure sensitive paints (PSPs) can be used implementing the heat-mass transfer analogy. Thus, the question arises whether mass transfer methods can be used as a surrogate to thermal methods. In this study, a thermal technique with IR was compared to a heat-mass transfer method with PSP. A new method for collecting large datasets with PSP was implementing in this study to account for paint degradation. Results indicate that adiabatic effectiveness is best scaled by accounting for specific heat with the advective capacity ratio (ACR) using thermal techniques. Results also indicated that the mass flux ratio (M) is an appropriate parameter to scale adiabatic effectiveness results between gases using the mass transfer technique. This has significant implication for engine designers that rely on experimental data to predict engine behavior.

15. SUBJECT TERMS
Film Cooling, Scaling, Pressure Sensitive Paint

16. SECURITY CLASSIFICATION OF:			17. LIMITATION OF ABSTRACT	18. NUMBER OF PAGES	19a. NAME OF RESPONSIBLE PERSON
a. REPORT	b. ABSTRACT	c. THIS PAGE			James L. Rutledge, AFIT/ENY
U	U	U	UU	140	19b. TELEPHONE NUMBER *(Include area code)* (937) 255-6565, ext 4734 (james.rutledge@afit.edu)

Standard Form 298 (Rev. 8-98)
Prescribed by ANSI Std. Z39-18